In-beam spectroscopy of high-K states in ^{254}No

Thesis submitted in accordance with the
requirements of the University of Liverpool
for the degree of Doctor in Philosophy
by

Andrew James Ward

Oliver Lodge Laboratory
University of Liverpool

2016

Abstract

The transfermium nucleus ^{254}No ($Z = 102$, $N = 152$) has been studied in a recoil-decay tagging experiment using the SAGE in-beam spectrometer, RITU gas-filled separator and GREAT focal-plane spectrometer at the Accelerator Laboratory of the University of Jyväskylä (JYFL).

Both γ rays and conversion electrons from the ground-state band of ^{254}No have been observed with SAGE. Coincidences between them can be seen and it is possible to measure internal conversion coefficients for some transitions in the band. This shows that they have E2 multipolarity, as expected for a rotational band built on a $K^{\pi} = 0^{+}$ state.

The two previously identified K isomers in ^{254}No have also been seen. In the prompt data tagged on the slow isomer's decay the prominent 605 keV transition from previous decay spectroscopy experiments is not seen with the expected intensity. This allows one of the previously proposed level schemes to be ruled out. It is possible that this transition is not seen in the in-beam data at all and the peak at this energy is entirely from inelastic neutron scattering reactions within the SAGE germanium detectors. If this is the case the 605 keV transition could directly depopulate the fast isomer into a band built on the slow isomer without any intermediate structure.

There is not enough data to measure γ-ray branching ratios in the band built on the slow isomer so a new method has been developed to determine the single-particle structure of the isomer by comparing the in-beam conversion-electron spectrum above it with `Geant4` simulations of the same level scheme with a varying single-particle g factor. This suggests that the structure of the slow isomer is the $\frac{7}{2}^{+}\,[624]_{\nu} \otimes \frac{9}{2}^{-}\,[734]_{\nu}$ two-neutron state.

'Die Deutung dieses Spektrums bot große Schwierigkeiten.'

Lise Meitner
Z. Phys. **9** (1922) 131

Acknowledgements

Without my collaborators at the University of Jyväskylä none of the experimental work here would have been possible. Thank you to all of them, and especially Mikael Sandzelius for the work he did during the 2016 SAGE campaign. I'm also grateful to the technical staff at JYFL and to Marjut Hilska for helping arrange accommodation for my visits to Finland.

I would also like to thank everyone in the physics department in Liverpool, especially the members of the superheavy group (past and present): Philippos, Danny, Andy, Tom and Eddie.

Finally, I would like to thank my supervisor, Rodi Herzberg, for his support, advice and encouragement over the last four years.

Contents

1 Introduction **1**

2 Nuclear models **3**
2.1 Liquid drop model and semi-empirical mass formula . . . 3
2.2 Spherical shell model . . . 5
2.3 Nuclear deformation and the Nilsson model . . . 8
2.4 Nuclear rotation . . . 12
2.5 Magnetic moments and nuclear g factors . . . 14
2.6 Mixing of states . . . 16
2.7 Calculations and theoretical predictions . . . 18

3 Radioactive decay **23**
3.1 α decay . . . 24
3.2 Electromagnetic decay . . . 26
3.3 Isomers . . . 32

4 Previous knowledge and regional systematics **35**
4.1 α decay . . . 36
4.2 Ground-state rotational band . . . 36
4.3 $K^{\pi} = 3^{+}$ band . . . 38
4.4 263 ms isomer . . . 38
4.5 183 µs isomer . . . 39
4.6 Other K isomers around ^{254}No . . . 40

5 Experimental details **42**
5.1 Targets . . . 43
5.2 SAGE – in-beam spectroscopy . . . 44
5.3 RITU – recoil separation . . . 50
5.4 GREAT – decay spectroscopy . . . 52
5.5 Electronics and data acquisition . . . 54
5.6 Calibration . . . 56

6 Data analysis and simulations **61**
6.1 Recoil-decay tagging . . . 61
6.2 SAGE background subtraction . . . 65

6.3 Peak fitting . . . 65
6.4 Geant4 simulations . . . 67

7 Branching ratios and E2/M1 transition intensities **71**
7.1 E2/M1 electron intensity ratios . . . 73
7.2 M1 and E2 electron region limits . . . 76
7.3 Background . . . 80
7.4 Initial population of levels . . . 82
7.5 Simulations . . . 82
7.6 Summary . . . 84

8 Ground-state band **86**
8.1 Conversion coefficients . . . 86
8.2 Coincidences . . . 87
8.3 Discussion . . . 93

9 Level scheme between the isomers **95**
9.1 Intensity of 605 keV transition . . . 97
9.2 ^{74}Ge(n,n'γ) . . . 99
9.3 Conversion electrons from a 605 keV transition . . . 103
9.4 Intensity of a 482 keV transition . . . 104
9.5 Decay of the fast isomer . . . 105
9.6 Discussion . . . 106

10 Structure of the $K^{\pi} = 8^{-}$ isomer **109**
10.1 Finding g_K for the slow isomer . . . 109
10.2 Discussion . . . 110

11 Conclusions **116**
11.1 Structure of K isomers in ^{254}No . . . 116
11.2 Measuring conversion coefficients with SAGE . . . 118

References **119**

Chapter 1

Introduction

A simple model of an atomic nucleus predicts that if it contains more than about 110 protons the repulsive electrostatic force between them makes it impossible for the nucleus to remain bound together. The existence of the heaviest nuclei depends on gaining extra stability from quantum shell effects. Nuclei with certain *magic numbers* of protons and neutrons in closed shells are seen experimentally to be more tightly bound and more stable. The values of these magic numbers are known up to $Z = 82$, $N = 126$. The existence of the superheavy nuclei is due to the next closed shell gap beyond these, but identifying its location is still not possible experimentally.

Most elements lighter than uranium ($Z = 92$) have isotopes which are either stable or have half-lives long enough that they occur naturally on Earth, but the elements beyond this must be produced in nuclear reactions. The first synthetic elements beyond uranium were produced by neutron capture followed by β decay [1], but for $Z > 100$ heavy-ion fusion-evaporation reactions must be used [2]. The heaviest nucleus to be experimentally synthesised so far is $^{294}118$ at the Flerov Laboratory of Nuclear Reactions (FLNR) in Dubna, Russia [3]. The heaviest nuclei are made in reactions with extremely low cross sections and production rates are less than one atom/week. This means detailed spectroscopy of their nuclear properties is not possible, although a small number of α-photon coincidences have been seen on the decay chain from $^{288}115$ in an experiment at the Gesellschaft für Schwerionenforschung (GSI) in Darmstadt, Germany [4].

The available combinations of stable beams and stable or long-lived targets also mean it is not possible to produce the more neutron-rich superheavy isotopes, closer to the predicted closed neutron shell, in fusion-evaporation reactions. High-intensity radioactive ion beams or multi-nucleon transfer in deep inelastic scattering reactions might make the synthesis of these isotopes possible, but the location of the next neutron shell gap is not currently accessible for experimental investigation.

An alternative approach to testing models predicting the location of the island of stability is to study the heavy actinide nuclei around fermium ($Z = 100$) and nobelium ($Z = 102$). These nuclei are not spherical and the variation of the nuclear energy levels with the shape of the nucleus means that some levels predicted to lie either side of the next spherical shell gap bend down towards their Fermi surfaces. Higher production cross sections make it possible to use in-beam spectroscopy to investigate the structure of the nuclei [5].

The ^{208}Pb(^{48}Ca,2n)^{254}No fusion-evaporation reaction has one of the largest cross sections (≈ 2 µb) for producing a transfermium nucleus. Previous experiments have identified two isomeric states in ^{254}No, which are discussed in more detail in chapter 4. This work describes the use of the SAGE combined γ-ray and conversion-electron spectrometer with the RITU gas-filled recoil separator and the GREAT focal-plane spectrometer at the Accelerator Laboratory of the University of Jyväskylä (JYFL) to study the structure of the isomers in ^{254}No.

Chapter 2

Nuclear models

The atomic nucleus is made up of neutrons and protons. The attractive strong nuclear force acts between both protons and neutrons and holds them together, but the repulsive electrostatic force between the positive electric charge of the protons acts to force them apart. The strong force has a short range and acts only between neighbouring nucleons, but the electrostatic force has an infinite range and acts between all the protons in the nucleus. As the number of protons in the nucleus increases the electrostatic force becomes increasingly important and a simple model of the nucleus suggests that when there are more than about 110 protons the repulsion between them is enough for the nucleus to become unbound. The development of the nuclear shell model uses quantum mechanics to explain the existence of heavier nuclei.

Models of the nucleus can also describe its excited states, either excitations of single nucleons in the shell model or collective excitations with all the nucleons vibrating or rotating together, and the transitions between these states.

2.1 Liquid drop model and semi-empirical mass formula

The liquid drop model ignores the protons and neutrons within the nucleus and treats the entire nucleus as a droplet of fluid with a binding energy described by a volume term, a surface tension term and an electrostatic repulsion term. Weizsäcker developed the semi-empirical mass formula [7] by adding corrections to this for

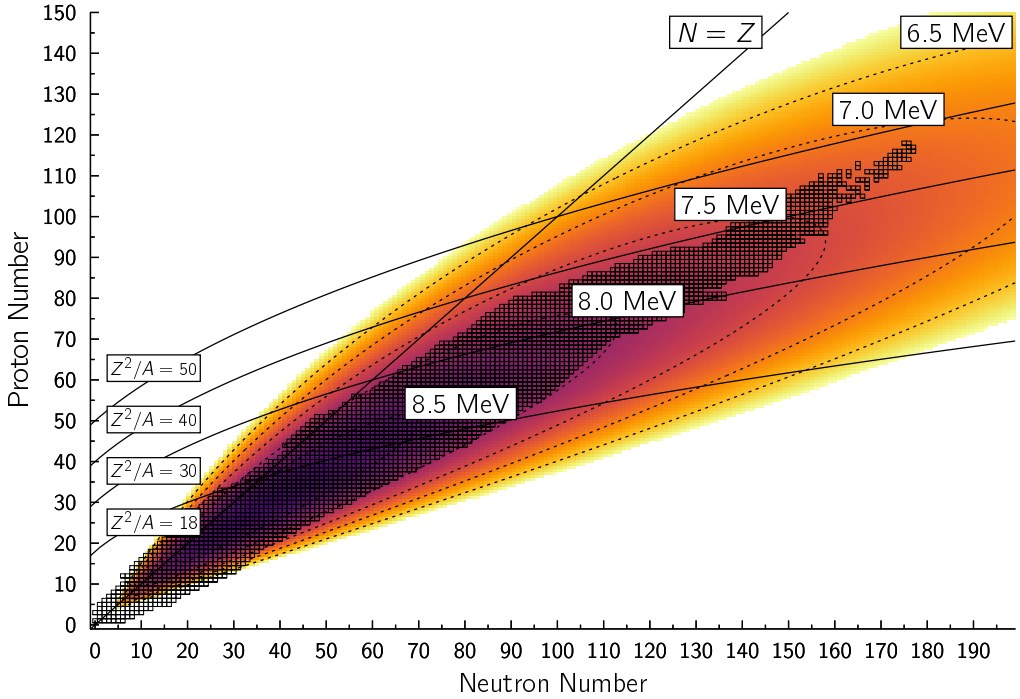

Figure 2.1: Nuclear chart with the predicted binding energy per nucleon from the liquid drop model overlaid. Lines of constant fissility, Z^2/A, are also shown. Based on figure 1 from Herzberg (2013) [6].

symmetry between the numbers of protons and neutrons and for the pairing between nucleons. The mass of a nucleus with Z protons and $A - Z$ neutrons is

$$m(A, Z) = m_\mathrm{p} Z + m_\mathrm{n}(A - Z) - \frac{E_\mathrm{B}}{c^2} \tag{2.1}$$

where m_p is the mass of a proton, m_n is the mass of a neutron and E_B is the nuclear binding energy [8],

$$E_\mathrm{B} = a_\mathrm{v} A - a_\mathrm{s} A^{2/3} - a_\mathrm{c} \frac{Z(Z-1)}{A^{1/3}} - a_\mathrm{sym} \frac{(A-2Z)^2}{A} + \delta \tag{2.2}$$

The first three terms are from the liquid drop model:

- $a_\mathrm{v} A$ is proportional to the nuclear volume and describes the attractive strong

nuclear force between all nucleons, increasing as the number of nucleons increases

- $a_s A^{2/3}$ is proportional to the surface area and describes the effects of surface tension.
- $a_c \frac{Z(Z-1)}{A^{1/3}}$ depends on the number of protons and describes the repulsive electrostatic force between them.

The other two terms are Weizsäcker's semi-empirical corrections:

- $a_{sym} \frac{(A-2Z)^2}{A}$ is the symmetry energy term and is related to the difference between the number of protons and the number of neutrons. Nuclei are more stable with the same number of protons as neutrons, but this is less important in heavier nuclei.
- δ is the pairing term and can be positive, negative or zero depending whether the nucleus has even numbers of protons, neutrons or both. The nucleus is more tightly bound with even numbers of protons and neutrons because they can form pairs with opposite spins.

Figure 2.1 shows the binding energy per nucleon predicted by the liquid drop model plotted over the nuclear chart. The edge of the region of known nuclei is close to the $Z^2/A = 40$ line up to around $Z \approx 90$, $N \approx 140$ but above this the liquid drop model is no longer a good description of the nucleus.

2.2 Spherical shell model

The liquid drop model describes the general trend of nuclear binding energies well, but around certain *magic numbers* of protons or neutrons there are large differences between the liquid drop model's predictions and experimental data [9]. This can be explained by a microscopic approach, in which all nucleons are considered individually and put into discrete energy levels, or *shells*. There are separate sets of shells for

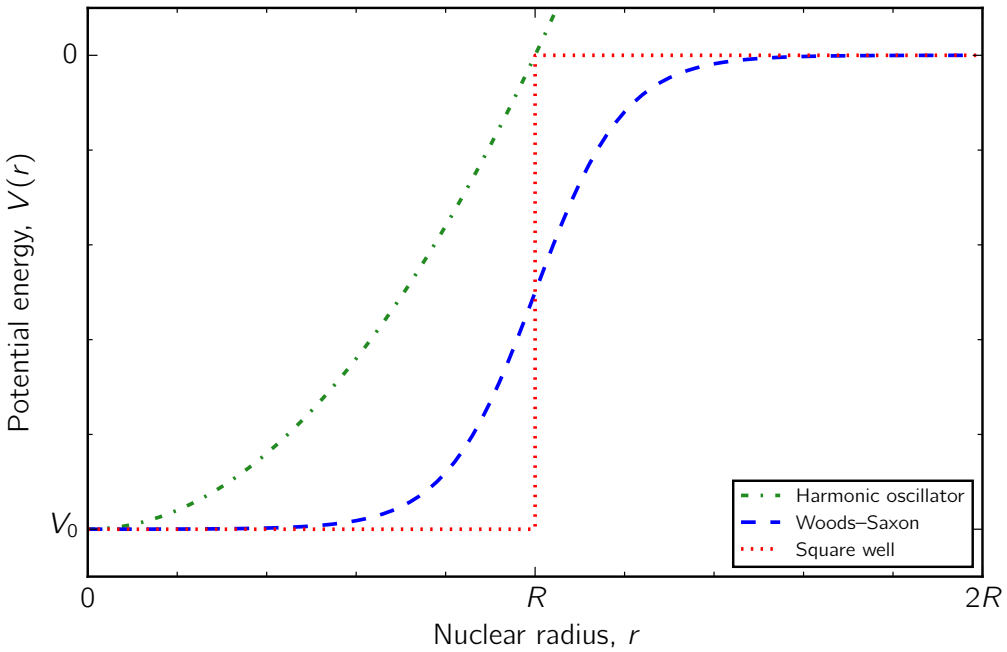

Figure 2.2: Some of the forms of the potential energy used in the spherical shell model.

protons and neutrons and each shell has a fixed maximum number of either protons or neutrons that it can hold. Nucleons start by filling the lowest-energy shell and when this is full they start filling the next higher-energy shell. The magic numbers of protons and neutrons occur at large energy gaps between shells, where nuclei are more tightly bound and stable against decay.

The spacing of the nuclear energy levels is found by solving Schrödinger's equation with a potential of the form

$$V = V(r) + V_{\vec{\ell}\cdot\vec{s}} \tag{2.3}$$

where $V(r)$ is a spherically symmetric term and the $V_{\vec{\ell}\cdot\vec{s}}$ term is from the coupling of the nucleon's intrinsic, $\vec{s}$, and orbital, $\vec{\ell}$, angular momentum [10, 11].

Figure 2.2 shows some of the choices of the spherically symmetric potential, $V(r)$.

One of these is the Woods–Saxon potential [12],

$$V(r) = \frac{-V_0}{1 + e^{(r-R)/a}} \tag{2.4}$$

where r is the radius and V_0, R and a control the depth, width and shape of the potential well. Also plotted is a spherically symmetric harmonic oscillator potential,

$$V(r) = -V_0 \left(1 - \left(\frac{r}{R}\right)^2\right) \tag{2.5}$$

where, again, r is the radius and V_0 and R control the depth and width of the potential well.

The Woods–Saxon potential is a more realistic model of the nucleus but it is easier to solve Schrödinger's equation with the harmonic oscillator potential. The harmonic oscillator can be made more realistic if the bottom of the potential well is flattened by adding an extra term proportional to ℓ^2,

$$V(r) = -V_0 \left(1 - \left(\frac{r}{R}\right)^2\right) + K\ell^2 \tag{2.6}$$

The spin-orbit coupling term depends on the nuclear radius and the magnitude of the orbital angular momentum,

$$V_{\vec{\ell}\cdot\vec{s}} = V_{\ell s}(r)\vec{\ell}\cdot\vec{s} \tag{2.7}$$

The spin-orbit force shifts levels with $j = \ell + \frac{1}{2}$ to lower energies and levels with $j = \ell - \frac{1}{2}$ to higher energies, where $\vec{j} = \vec{\ell} + \vec{s}$ is the total angular momentum of the nucleon. This splits energy levels with the spin and orbital angular momentum coupled parallel or anti-parallel, with the size of the splitting increasing as ℓ increases, and reproduces better the experimental magic numbers. The effect of the spin-orbit splitting can be seen in figure 2.3 where it forces down the $1i_{13/2}$ orbital and splits the $2f_{7/2}$ and $2f_{5/2}$, opening up a spherical shell gap at $Z = 114$. If the strength of

the spin-orbit interaction was less then the these orbitals would stay closer together and this shell gap would be smaller.

For each nuclear shell there are $2j + 1$ possible projections of the total angular momentum, $\vec{j}$, onto the symmetry axis of the nucleus, varying from $+j$ to $-j$ in integer steps. From the Pauli exclusion principle there can only be one nucleon with each angular momentum projection and the total degeneracy of each level in the shell model is $2j + 1$.

Excited states of nuclei can be formed by moving one or more nucleons into higher energy orbitals, leaving holes in the lower orbitals.

2.3 Nuclear deformation and the Nilsson model

Around the magic numbers of protons and neutrons nuclei are generally spherical, but away from these areas the shapes of many nuclei are deformed. The simplest deformation is an axially symmetric quadrupole deformation, in which the nuclear shape can be either prolate (like a rugby ball) or oblate (like a Smartie), but triaxial (like a kiwi fruit) or higher-order deformations are also possible.

The Nilsson model [14] assumes that the potential for the deformed nucleus is an anisotropic harmonic oscillator,

$$V(\vec{r}) = \frac{m}{2}\left(\omega_x^2 x^2 + \omega_y^2 y^2 + \omega_z^2 z^2\right) \tag{2.8}$$

For a deformation which is symmetric about the z-axis, $\omega_x = \omega_y$. The deformation parameter, δ, relates ω_x to ω_z and describes the shape of the nucleus,

$$\omega_x^2 = \omega_y^2 = \omega_0^2\left(1 + \frac{2}{3}\delta\right) \tag{2.9}$$

$$\omega_z^2 = \omega_0^2\left(1 - \frac{4}{3}\delta\right) \tag{2.10}$$

For spherical nuclei $\delta = 0$, for prolate deformations $\delta > 0$ and for oblate deformations

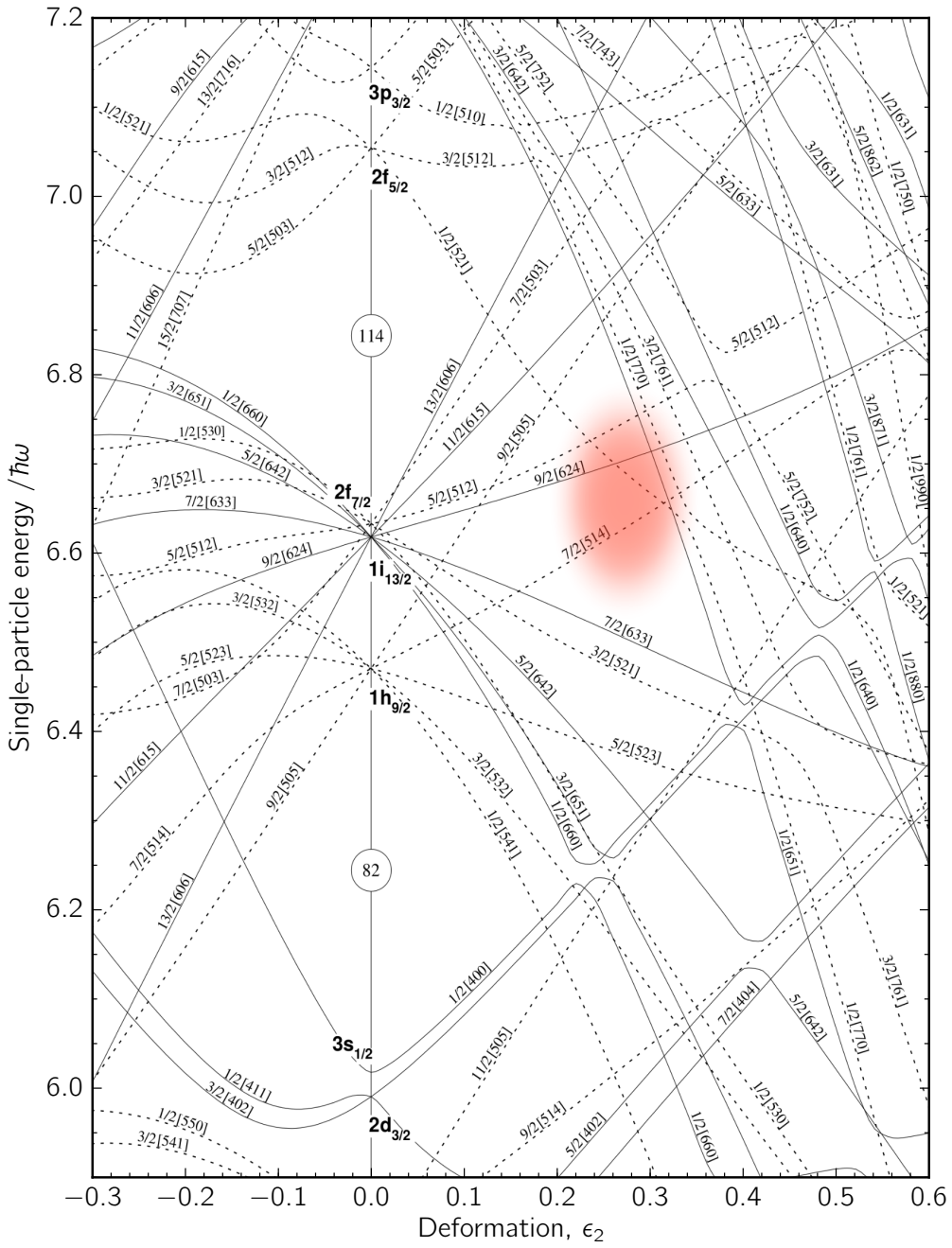

Figure 2.3: Nilsson diagram for protons in nuclei with $Z > 82$, showing the change in energy of different Nilsson levels with the deformation of the nucleus. Solid lines are levels with positive parity and dashed lines are levels with negative parity. The shaded area shows the region around the Fermi surface in ^{254}No. Based on Firestone (1996) [13].

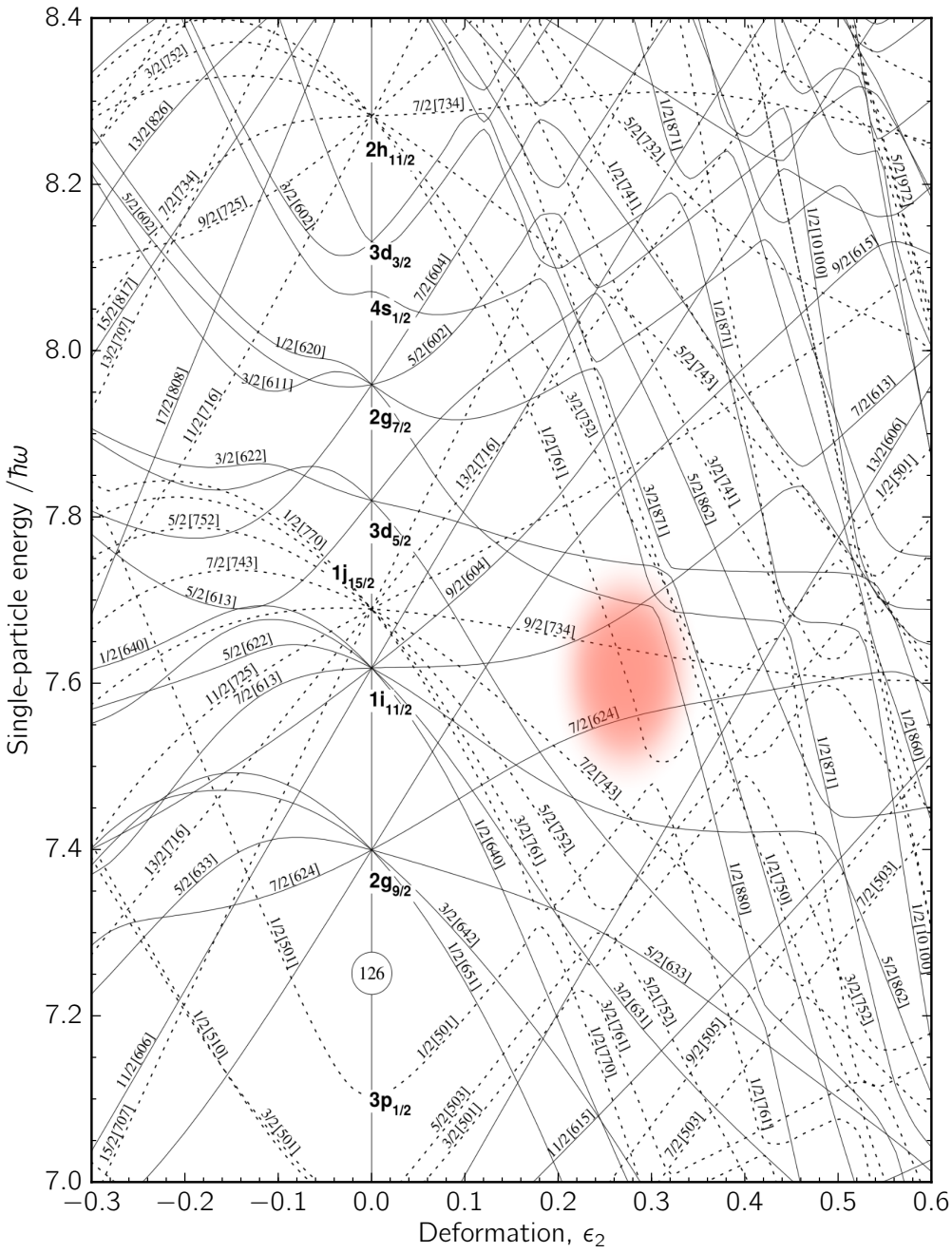

Figure 2.4: Nilsson diagram for neutrons in nuclei with $N > 126$, showing the change in energy of different Nilsson levels with the deformation of the nucleus. Solid lines are levels with positive parity and dashed lines are levels with negative parity. The shaded area shows the region around the Fermi surface in ^{254}No. Based on Firestone (1996) [13].

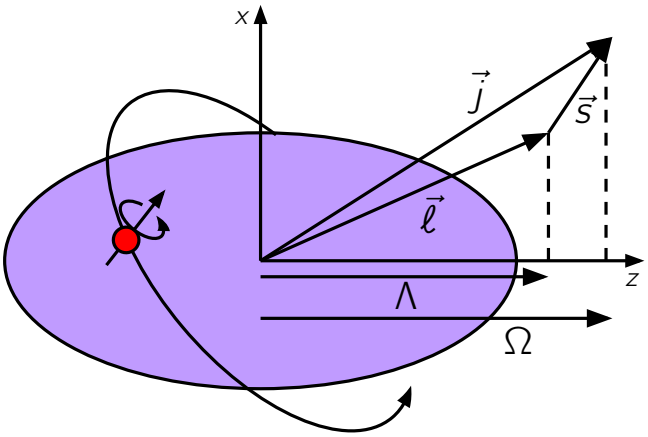

Figure 2.5: Quantum numbers used to label energy levels in the Nilsson model for a nucleon with intrinsic spin $\vec{s}$ and orbital spin $\vec{\ell}$. The z-axis is along the symmetry axis of the nucleus.

$\delta < 0$. The complete Hamiltonian for the Nilsson model is

$$\widehat{H} = -\frac{\hbar^2}{2m}\nabla^2 + \frac{m}{2}\left(\omega_x^2\left(x^2+y^2\right)+\omega_z^2 z^2\right) + C\vec{\ell}\cdot\vec{s} + D\ell^2 \qquad (2.11)$$

with extra terms $C\vec{\ell}\cdot\vec{s}$ to account for spin-orbit coupling and $D\ell^2$ to flatten the bottom of the potential well. Values of C and D are chosen so the model matches experimental results for spherical nuclei.

Solving Schrödinger's equation with this Hamiltonian gives a set of energy levels similar to those for the spherical shell model, but the energies of the different shells vary with the deformation of the nucleus. The Nilsson diagrams in figures 2.3 and 2.4 show the calculated change in energy of different shells as the nuclear deformation changes for protons and neutrons. These show how some levels above the proposed spherical shell gap bend down towards the Fermi surface in the nuclei around ^{254}No.

Energy levels in the Nilsson model are labelled with the asymptotic quantum numbers

$$\Omega^{\pi}\left[Nn_z\Lambda\right]$$

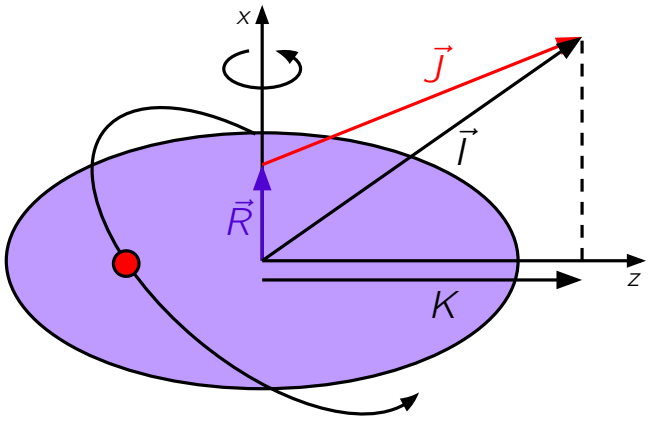

Figure 2.6: Angular momentum in a prolate-deformed nucleus with a single unpaired nucleon orbiting a rotating core. The collective rotation is around the x-axis and the symmetry axis of the nucleus is along the z-axis.

where Ω is the projection of the total angular momentum, π is the parity, N is the principal quantum number (the major oscillator shell from which the orbital originates), n_z is the number of nodes in the wave function in the z-direction and Λ is the projection of the orbital angular momentum. These are shown in figure 2.5. There are only two possible projections of the intrinsic spin ($\pm\frac{1}{2}$) so levels always have $\Omega = \Lambda \pm \frac{1}{2}$. The parity is given by $\pi = (-1)^N$.

The deformed shape of the nucleus means that orientation of a single-particle wave function relative to the nuclear core now affects its energy and states with the same total angular momentum, j, but different projections of this onto the symmetry axis of the nucleus now have different energies. This lifts the $2j + 1$ degeneracy of the shell model and each energy level in the Nilsson model can hold two nucleons in time-reversed orbits with total spin projections $\pm\Omega$.

2.4 Nuclear rotation

Nuclear rotation is a collective excitation involving all the nucleons in the nucleus. Quantum mechanically it is not possible for a sphere to rotate, but for deformed

nuclei rotation is possible. The spin of the nucleus is split into components $\vec{J}$ from the single-particle structure and $\vec{R}$ from the collective rotation, shown in figure 2.6. These couple together to give a total angular momentum

$$\vec{I} = \vec{R} + \vec{J} \tag{2.12}$$

which has a projection K on the symmetry axis of the nucleus.

If there is more than one unpaired nucleon their single-particle angular momenta are summed before adding them to the angular momentum from collective rotation,

$$\vec{J} = \sum_i \vec{j_i} \tag{2.13}$$

The total projection is also the sum of the projections for the individual particles,

$$K = \sum_i \Omega_i \tag{2.14}$$

A set of nuclear states from collective rotation are seen with rotational energies given by

$$E_{\text{rot}} = \frac{\hbar^2}{2\mathcal{I}} \times \left[I(I+1) - K^2 \right] \tag{2.15}$$

where $\mathcal{I}$ is the moment of inertia of the nucleus [15]. The energies of the levels increase as the square of the spin so the energies of transitions between them are equally spaced. The set of equally spaced peaks in a γ-ray spectrum is a characteristic sign of a rotational band.

If the single-particle spin is zero then $K = 0$ and the symmetry of the nucleus means that rotating it by 180° is equivalent to a reflection and only even integer values of $\vec{R}$ are possible. If $K \neq 0$ then this symmetry is broken and any integer value of $\vec{R}$ is allowed.

2.5 Magnetic moments and nuclear g factors

Just like a current flowing round a loop, the rotation of the charged nucleus creates a magnetic dipole moment. Magnetic moments of nuclei are measured in units of nuclear magnetons,

$$\mu_{\mathrm{N}} = \frac{e\hbar}{2m_{\mathrm{p}}} \tag{2.16}$$

where e is the charge of an electron and m_{p} is the mass of a proton. The gyromagnetic ratio or g factor, g, is the ratio of the magnetic moment, $\vec{\mu}$, to the angular momentum, $\vec{\ell}$,

$$\vec{\mu} = g\vec{\ell}\mu_{\mathrm{N}} \tag{2.17}$$

Nuclei can have magnetic moments from the collective rotation of the entire nucleus or from individual nucleons orbiting the core, and there are different g factors associated with each.

Rotational g factors

For a uniformly-rotating nucleus with a uniform charge distribution the collective g factor is expected to be

$$g_R = \frac{Z}{A} \tag{2.18}$$

Figure 2.7 shows experimentally measured g factors in some rare-earth nuclei. These are mostly less than Z/A [15] and a quenching factor, $q = 0.7$, is used to give a better estimate of the g factor,

$$g_R = q \times \frac{Z}{A} \tag{2.19}$$

There are not enough experimentally measured magnetic moments in actinide nuclei to find a quenching factor so $q = 0.7$ is also used.

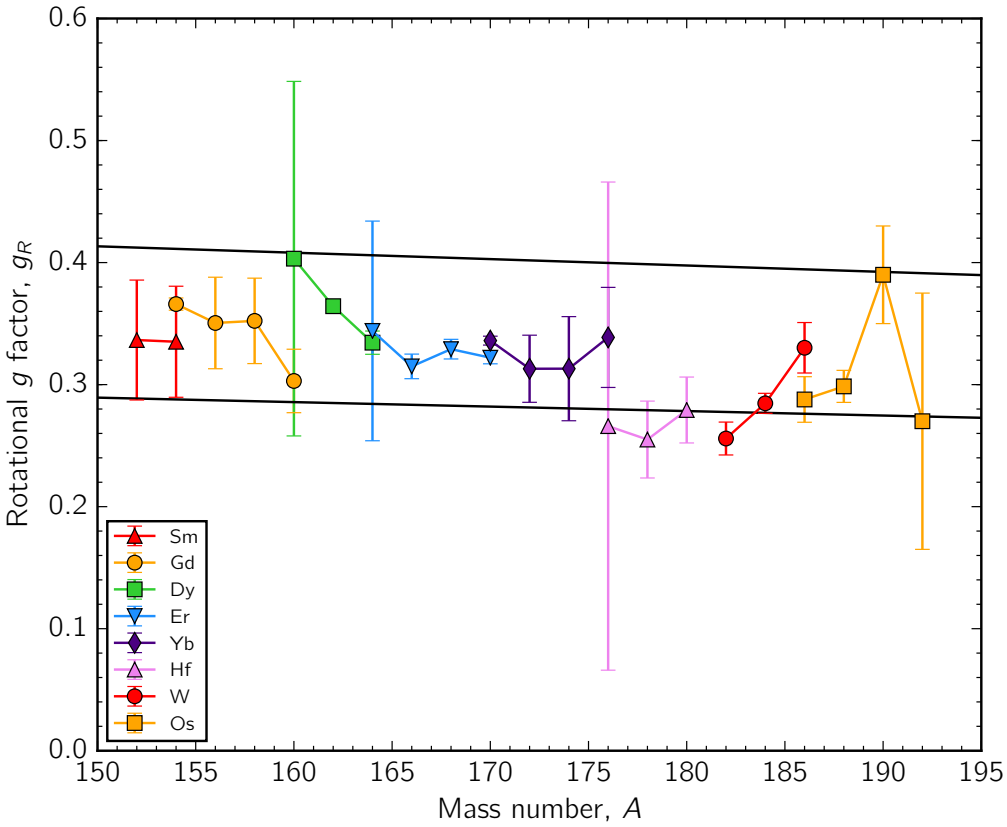

Figure 2.7: Experimentally measured rotational g factors for first excited 2^+ states in even-even rare-earth nuclei. The black lines roughly mark $g_R = Z/A$ and $g_R = 0.7 \times Z/A$. Data is taken from Grodzins (1968) [16]. See also figure 4-6 of Bohr and Mottelson (1975) [15].

Single-particle g factors

Pairs of protons or neutrons in the same Nilsson level occupy time-reversed orbits with no overall magnetic moment, but for any unpaired nucleons there is a magnetic moment from the single particle orbiting the nucleus. The single-particle g factor, g_K, depends on the Nilsson level occupied by the unpaired nucleon,

$$g_K = \frac{1}{\Omega} \langle \Omega \,|\, g_\ell \ell + g_s s \,|\, \Omega \rangle \tag{2.20}$$

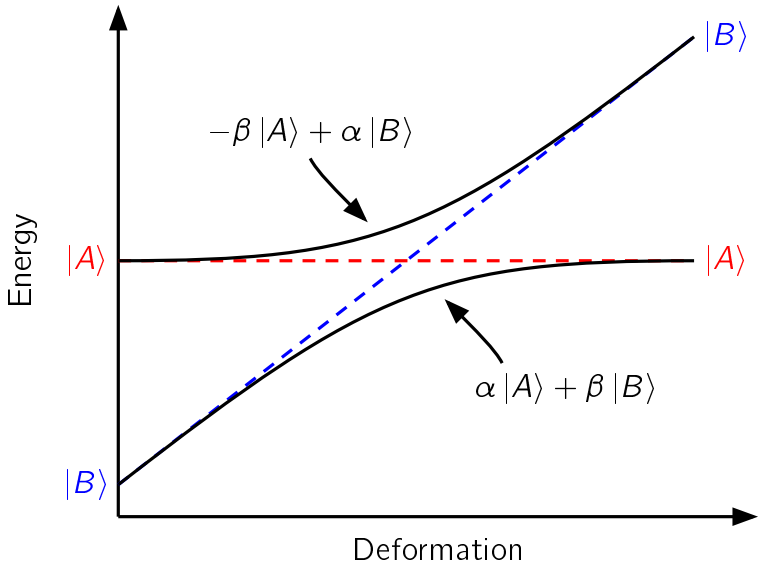

Figure 2.8: Mixing of two states in the Nilsson model.

where ℓ and s are the orbital and spin angular momentum and g_ℓ and g_s the orbital and spin g factors of the nucleon. If there are two unpaired nucleons, with g factors g_1 and g_2 and spins $\vec{j}_1$ and $\vec{j}_2$, the effective g factor can be calculated with the generalised Landé formula [17],

$$\begin{aligned} g_K = g_1 \frac{J(J+1) + j_1(j_1+1) - j_2(j_2+1)}{2J(J+1)} \\ + g_2 \frac{J(J+1) - j_1(j_1+1) + j_2(j_2+1)}{2J(J+1)} \end{aligned} \tag{2.21}$$

where $\vec{J} = \vec{j}_1 + \vec{j}_2$.

2.6 Mixing of states

The models considered so far describe pure nuclear states, either entirely collective nuclear motion or pure single-particle states, but it is possible for quantum mechanical mixing to occur between states with the same quantum numbers.

If there are two nuclear states, $|\psi_A\rangle$ and $|\psi_B\rangle$, with no interactions between them

Schrödinger's equation in matrix form is

$$\begin{pmatrix} \widehat{H}_{\mathrm{A}} & 0 \\ 0 & \widehat{H}_{\mathrm{B}} \end{pmatrix} \begin{pmatrix} \psi_{\mathrm{A}} \\ \psi_{\mathrm{B}} \end{pmatrix} = E_i \begin{pmatrix} \psi_{\mathrm{A}} \\ \psi_{\mathrm{B}} \end{pmatrix} \tag{2.22}$$

which can be split into two separate equations, one for each state, with no coupling between them. If there are interactions between the states the off-diagonal terms of the matrix are no longer zero,

$$\begin{pmatrix} \widehat{H}_{\mathrm{A}} & V \\ V & \widehat{H}_{\mathrm{B}} \end{pmatrix} \begin{pmatrix} \psi_{\mathrm{A}} \\ \psi_{\mathrm{B}} \end{pmatrix} = E'_j \begin{pmatrix} \psi_{\mathrm{A}} \\ \psi_{\mathrm{B}} \end{pmatrix} \tag{2.23}$$

and the equations for the two states can't be separated. The interaction between the states is $V = \langle \psi_{\mathrm{A}} \,|\, V \,|\, \psi_{\mathrm{B}} \rangle$. Newton's third law means that the interaction on ψ_{A} from ψ_{B} must be the same as the interaction on ψ_{B} from ψ_{A} so the matrix is symmetric [8]. As well as mixing the configurations of the states, the interactions between them also shift their energies apart. The new energies and wave functions of the states are the eigenvalues and eigenvectors of this matrix equation.

The energies of the mixed states are given by

$$E'_{1,2} = \frac{E_1 + E_2 \pm \sqrt{(E_1 - E_2)^2 + 4V^2}}{2} \tag{2.24}$$

where $E_{1,2}$ are the energies of the pure states. The energy shift is greater for states with a smaller initial energy spacing and for states which interact more strongly (when the wave functions of the two states are more similar).

The mixed states' wave functions are

$$|\phi_{\mathrm{a}}\rangle = \alpha\,|\psi_{\mathrm{A}}\rangle + \beta\,|\psi_{\mathrm{B}}\rangle \tag{2.25}$$

$$|\phi_{\mathrm{b}}\rangle = -\beta\,|\psi_{\mathrm{A}}\rangle + \alpha\,|\psi_{\mathrm{B}}\rangle \tag{2.26}$$

where

$$\alpha = \frac{1}{\sqrt{1 + \frac{V^2}{(E'_j - E_j)^2}}} \tag{2.27}$$

and

$$\beta = \sqrt{1 - \alpha^2} \tag{2.28}$$

Figure 2.8 shows an example of mixing between two states. As the two energy levels approach each other their wave functions become more mixed, until at the point where they are closest the wave functions are $\phi_a = \frac{1}{\sqrt{2}} |\psi_A\rangle + \frac{1}{\sqrt{2}} |\psi_B\rangle$ and $\phi_b = -\frac{1}{\sqrt{2}} |\psi_A\rangle + \frac{1}{\sqrt{2}} |\psi_B\rangle$. The main component of the wave function of each level then swaps over, but the energy shift means that the levels never cross. This is also seen in figures 2.3 and 2.4, where two levels with the same spin and parity never cross.

2.7 Calculations and theoretical predictions

Nuclear models can be used to calculate theoretical properties of different nuclei, including predictions of the next magic numbers. Except in certain simple cases it is not possible to solve Schrödinger's equation analytically and numerical methods must be used to find approximate solutions. The many-body forces in the nucleus, with every nucleon affecting the potential for every other nucleon, mean that for heavier nuclei a simplified form of the potential is also necessary. Calculations predicting the location of the next magic numbers of the spherical shell model, and of nuclear properties in the deformed transfermium nuclei, use two main approaches: macroscopic-microscopic methods and self-consistent mean-field methods.

Macroscopic-microscopic methods

Strutinsky [18, 19] proposed that the energies of nuclear states could be calculated by taking the macroscopic liquid drop model and adding a correction for the

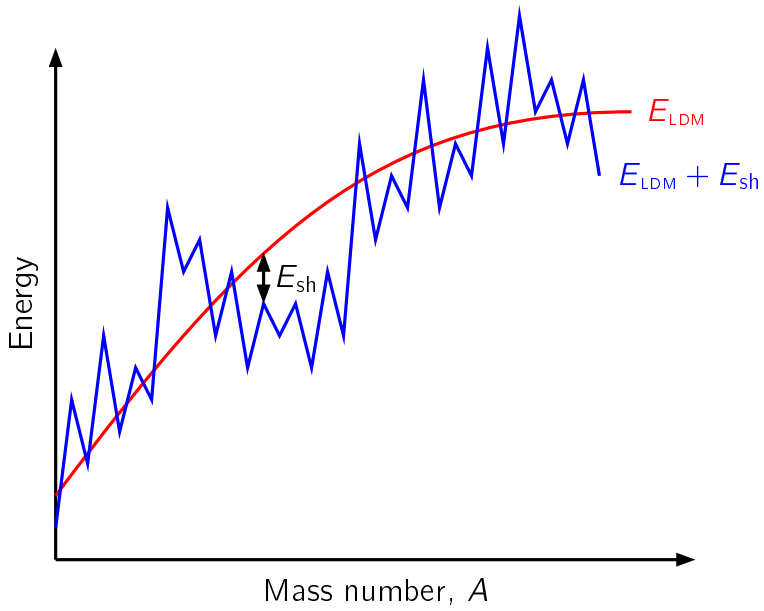

Figure 2.9: Smooth liquid-drop term, E_{LDM}, and Strutinsky shell correction term, E_{sh}, for macroscopic-microscopic calculations.

microscopic shell structure of the nucleus. The energy of a nuclear state is given by

$$E = E_{\mathrm{LDM}} + E_{\mathrm{sh}} \tag{2.29}$$

where E_{LDM} is a macroscopic component based on the liquid drop model, describing the behaviour of all nucleons, and E_{sh} is a microscopic component (the *Strutinsky shell correction*) which corrects for the shell structure of nucleons near the Fermi surface. This is shown in figure 2.9.

The shell correction term depends on the density of single-particle states and is found from the difference between a sum over the discrete energy states and a smeared average of this sum,

$$E_{\mathrm{sh}} = \sum_i \epsilon_i - \tilde{E} \tag{2.30}$$

where ϵ_i are the eigenvalues of the individual Nilsson energy levels and the average

energy term, $\tilde{E}$, is found by blurring the single-particle energies over an energy range of roughly $\hbar\omega_0$. Around shell gaps the level density is low so the discrete sum is less than the average and the shell correction term is negative, but where the level density is high the shell correction term is positive.

Examples of using this method to calculate single-particle excitation energies in transfermium nuclei can be found in the work of Parkhomenko and Sobiczewski [20, 21].

Self-consistent methods

Self-consistent methods use a purely microscopic approach and consider the forces on each individual nucleon. This problem is too complicated to solve so several simplifications are made. Instead of treating every nucleon separately and calculating the force on it from every other nucleon, an estimated average potential on any one nucleon within the nucleus due to all the other nucleons (the mean-field potential) is used. Even with this simplified potential Schrödinger's equation can't be solved analytically so an approximate solution for the nuclear wave function is calculated numerically. Using this wave function a new, more accurate, estimate for the mean-field potential is calculated and the process is repeated iteratively until it finds self-consistent solutions for the mean-field potential and the nuclear wave function [23]. The Hartree-Fock-Bogoliubov (HFB) method extends this to also take into account the pairing forces between nucleons [24]. For low-energy nuclear structure calculations it is possible to use non-relativistic kinematics, but some self-consistent calculations use relativistic models instead [24].

Different choices can be made for the form of the potential used in self-consistent methods. One possible choice is the Skyrme potential [25] which has a two-nucleon term and a three-nucleon term,

$$V = \sum_{i<j} V(i,j) + \sum_{i<j<k} V(i,j,k) \tag{2.31}$$

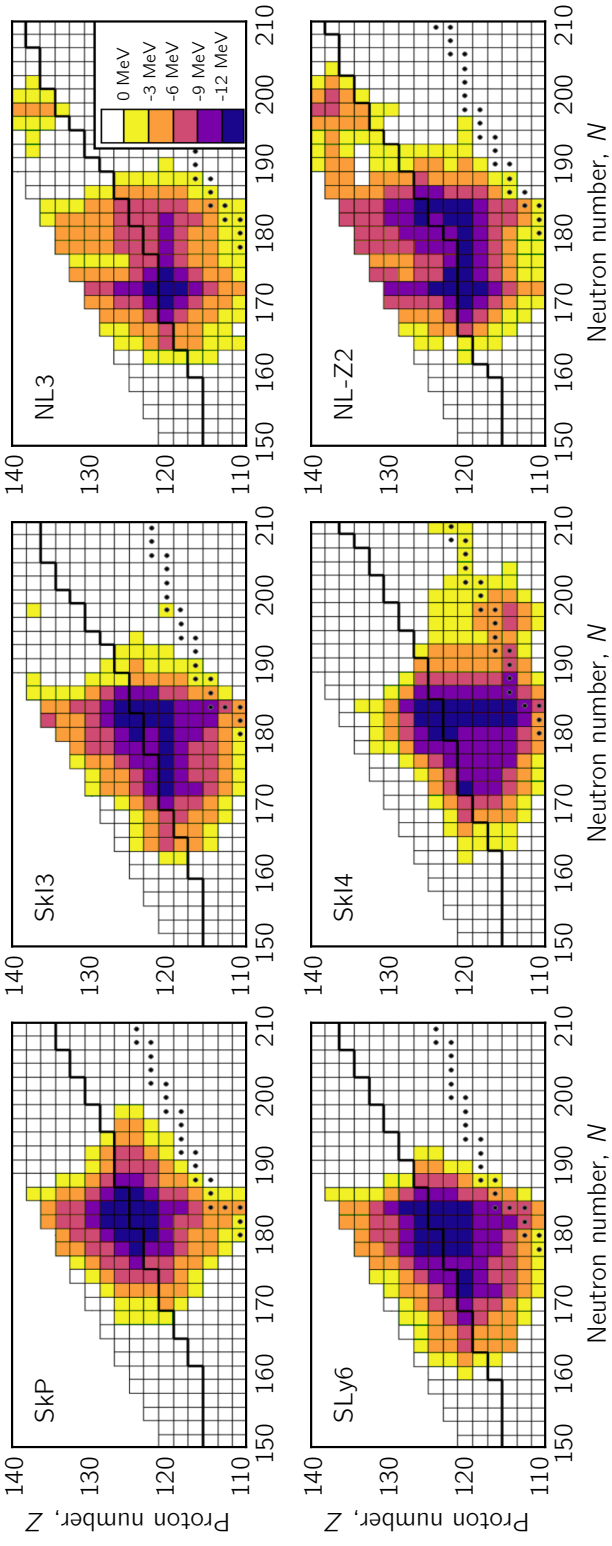

Figure 2.10: Calculated shell correction energies for spherical even-even nuclei using four different Skyrme models (SkP, SkI3, SLy6 and SkI4) and two different relativistic mean-field models (NL3 and NL-Z2). Modified from figure 2 of Bender, Nazarewicz and Reinhard (2001) [22].

To simplify the calculations a short-range force is used for the two-nucleon term and a zero-range force is used for the three-nucleon term. The Gogny force modifies the Skyrme force by using a finite range for the three-body term [26]. For either of these potentials there are parameters which can be adjusted so the results from calculations match better with experimental data for particular areas of the nuclear chart.

For the superheavy nuclei different choices of the form for the potential or its parameters give slightly different locations of the island of stability, as shown in figure 2.10. Predicted locations of the next magic numbers include $Z = 114$, 120 [27, 28], 126 [29] and $N = 172$ [27], 182 [28], 184 [29], or suggest that instead of a single number there is a wider region of more stable nuclei [22]. Without experimental data in this region it is not possible to tell which of these choices is the most accurate model.

Chapter 3

Radioactive decay

Radioactive decay is the process through which an unstable nuclear state changes to a lower energy state [30]. This can either be a lower-energy state in the same nucleus or a state in a different nucleus. A particle is emitted to carry away the energy lost by the nucleus and it is also possible for this particle to carry away some angular momentum. Observing the particles emitted by a nucleus as it decays can give information about the initial and final states of the nucleus and its structure.

Radioactive decay is a random process and the probability of a particular decay occurring in a given time is called the decay probability, λ. If there are initially N_0 nuclei then the number, N, left without decaying after time t decreases exponentially,

$$N(t) = N_0 e^{-\lambda t} \tag{3.1}$$

The time at which on average half of the original nuclei remain is called the half-life and is found from equation 3.1 by letting $N(t) = N_0/2$,

$$t_{\frac{1}{2}} = \frac{\log_e(2)}{\lambda} \tag{3.2}$$

For a nuclear state which can decay in more than one way the half-life for the state is found from the total decay probability which is the sum of the decay probabilities for each decay path.

3.1 α decay

α decay is the process through which an unstable nucleus decays to a lighter nucleus by emitting an α particle, made up of two protons and two neutrons:

$$ {}^{A}_{Z}\mathrm{X} \rightarrow {}^{A-4}_{Z-2}\mathrm{Y} + {}^{4}_{2}\alpha \tag{3.3} $$

For many of the heaviest nuclei ($Z > 82$) this is the most common type of decay from the ground state.

The energy released in an α decay, called its Q value, is equal to the change in the binding energy between the mother and the daughter and α particle. It can be calculated from their masses,

$$ Q = (m_{\mathrm{X}} - m_{\mathrm{Y}} - m_{\alpha})\, c^2 \tag{3.4} $$

This energy is shared between the kinetic energies of the daughter nucleus and the α particle, but the α particle is much lighter so conservation of momentum means that its kinetic energy, T_α, is much greater than that of the daughter nucleus,

$$ T_\alpha = \frac{Q}{1 + m_\alpha / m_{\mathrm{Y}}} \tag{3.5} $$

With only two particles after the decay conservation of energy and momentum means the total kinetic energy can only can only be split between them in one way and α particles from the same decay always have the same energy. This characteristic energy (for transfermium nuclei typically in the range 7–9 MeV) and the decay's half-life can be used to identify the decaying nucleus.

The decay probability of an α decay (and therefore also its half-life) depends strongly on the Q value. Geiger and Nuttall [31] noticed that there was a rough logarithmic relationship between them, called the Geiger–Nuttall rule,

$$ \log(\lambda) = C_1 \log(Q) + C_2 \tag{3.6} $$

where C_1 and C_2 are constants. Higher-energy α particles tend to have bigger decay probabilities and shorter half-lives.

The process of α decay can be modelled as an α particle forming inside the nucleus and then tunnelling out of the nucleus through a potential barrier. The probability for α particle emission, P_α, depends on the probability for each of these steps,

$$P_\alpha = P_{\text{Preformation}} \times P_{\text{Tunnel}} \tag{3.7}$$

The probability of the α particle preforming inside the nucleus depends on the nuclear structure. The probability of tunnelling depends on the α particle Q value, the barrier height, B, and width. The potential barrier can have two components, the Coulomb barrier and the centrifugal barrier,

$$B = B_{\text{Coul}} + B_{\text{Cent}} \tag{3.8}$$

There is always a Coulomb barrier from the electrostatic force between protons,

$$B_{\text{Coul}} = \frac{Z_Y Z_\alpha e^2}{4\pi\epsilon_0 r} \tag{3.9}$$

and for α decay between states with different spins there is also a centrifugal barrier,

$$B_{\text{Cent}} = \frac{\ell_\alpha \left(\ell_\alpha + 1\right) \hbar^2}{2mr^2} \tag{3.10}$$

where ℓ_α is the angular momentum carried away by the α particle. For α decay of the ground states of even-even nuclei ($J^\pi = 0^+$) it is possible to populate higher-spin members of the ground-state rotational band in the daughter nucleus, but the probability is less than for the ground-state to ground state decay because the centrifugal term increases the barrier height and the Q value for the decay decreases. This means even-even nuclei have a single characteristic α decay.

In odd-mass or odd-odd nuclei the ground states of the mother and daughter do

not always have the same spin and α decay to excited states in the daughter nucleus with the same spin as the mother is more likely. Several different α decays are seen between different pairs of states with the same spin. The energy of each different α decay depends on the excitation energies of the states it links in the mother and daughter.

The α particle has no intrinsic angular momentum because the two protons and two neutrons in it form two spin-zero pairs. All the angular momentum it carries away from the nucleus is in the form of its orbital angular momentum, ℓ_α, which depends on the spin of the mother and daughter nuclei,

$$|J_X - J_Y| \leq \ell_\alpha \leq J_X + J_Y \tag{3.11}$$

The parity of the α particle is related to the mother and daughter nuclei by

$$\pi_\alpha = \pi_X \pi_Y \tag{3.12}$$

but the decay is only allowed if the selection rule

$$\pi_\alpha = (-1)^{\ell_\alpha} \tag{3.13}$$

is followed.

3.2 Electromagnetic decay

Electromagnetic decay does not involve a change in either N or Z for a nucleus. Instead, an excited state in a nucleus decays to a lower-energy state in the same nucleus. The energy is carried away by an emitted particle which is most commonly a photon (γ decay), but can also be an atomic electron (internal conversion).

γ decay

The energy, E_γ, of the photon emitted in γ decay is equal to the difference between the energies of the initial and final nuclear states, E_i and E_f,

$$E_\gamma = E_\mathrm{i} - E_\mathrm{f} \tag{3.14}$$

The angular momentum, L, carried by the emitted photon and its parity, π, depend on the spins and parities of the initial and final nuclear states,

$$|J_\mathrm{i} - J_\mathrm{f}| \leq L \leq J_\mathrm{i} + J_\mathrm{f} \tag{3.15}$$

$$\pi_\gamma = \pi_\mathrm{i}\pi_\mathrm{f} \tag{3.16}$$

Transitions can be either electric or magnetic and selection rules for spin and parity mean only certain transitions are allowed:

$$\begin{aligned} \pi_\gamma &= +1 : \mathrm{M1}, \mathrm{E2}, \mathrm{M3}, \mathrm{E4}, \ldots \\ \pi_\gamma &= -1 : \mathrm{E1}, \mathrm{M2}, \mathrm{E3}, \mathrm{M4}, \ldots \end{aligned} \tag{3.17}$$

Transitions between two states will occur with all allowed multipolarities, but the intensity is usually dominated by the lowest multipolarity transition, with $L = |J_\mathrm{i} - J_\mathrm{f}|$.

Internal conversion

Internal conversion competes with γ decay but results in the emission of an atomic electron instead of a photon [32]. The energy of the emitted electron, E_e, depends on the energy of the initial and final nuclear states, E_i and E_f, and the binding energy, E_B, of the atomic shell from which the electron is emitted,

$$\begin{aligned} E_\mathrm{e} &= (E_\mathrm{i} - E_\mathrm{f}) - E_\mathrm{B} \\ &= E_\gamma - E_\mathrm{B} \end{aligned} \tag{3.18}$$

Table 3.1: Atomic electron binding energies for the inner electron sub-shells in nobelium [13].

Electron shell	Binding energy /keV
K	149.2
L_I	29.2
L_{II}	28.3
L_{III}	21.9
M_I	7.7
M_{II}	7.2
M_{III}	5.7
M_{IV}	5.0
M_V	4.8

For an electron to be emitted from a particular shell the transition energy must be greater than that shell's binding energy. Table 3.1 lists the binding energies for the inner electron shells in nobelium. After internal conversion the remaining electrons move to fill the vacancy and X-rays or Auger electrons are emitted in coincidence with the conversion electron.

The ratio of the decay probabilities for γ decay and internal conversion is called the internal conversion coefficient,

$$\alpha = \frac{\lambda_e}{\lambda_\gamma} \tag{3.19}$$

Conversion coefficients can also be defined separately for each atomic electron shell using the decay probability of electrons from that shell only,

$$\begin{aligned} \alpha &= \alpha_K + \alpha_L + \alpha_M + \dots \\ &= \frac{\lambda_K}{\lambda_\gamma} + \frac{\lambda_L}{\lambda_\gamma} + \frac{\lambda_M}{\lambda_\gamma} + \dots \end{aligned} \tag{3.20}$$

Conversion coefficients can be calculated approximately, assuming a point-like

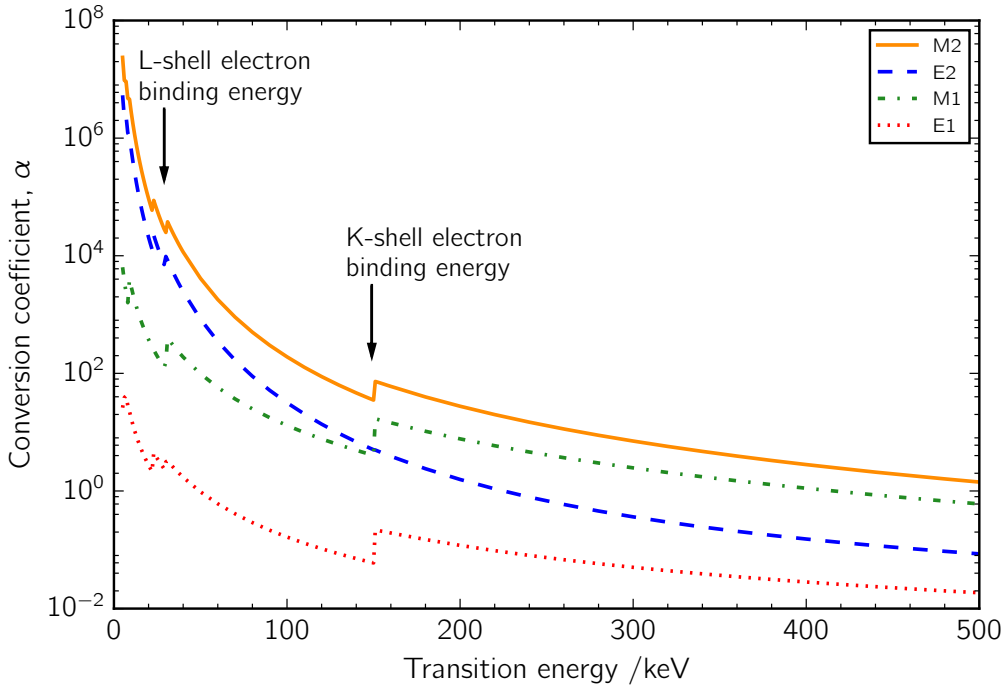

Figure 3.1: Internal conversion coefficients for different multipolarity transitions in nobelium. Arrows mark the binding energies for K- and L-shell electrons.

nucleus and ignoring relativistic effects [17],

$$\alpha(\mathrm{E}L) \approx \frac{Z^3}{n^3}\left(\frac{L}{L+1}\right)\left(\frac{e^2}{4\pi\epsilon_0\hbar c}\right)^4\left(\frac{2m_\mathrm{e}c^2}{E}\right)^{L+\frac{5}{2}} \tag{3.21}$$

$$\alpha(\mathrm{M}L) \approx \frac{Z^3}{n^3}\left(\frac{e^2}{4\pi\epsilon_0\hbar c}\right)^4\left(\frac{2m_\mathrm{e}c^2}{E}\right)^{L+\frac{3}{2}} \tag{3.22}$$

for electric or magnetic transitions respectively with multipolarity L. From these equations it can be seen that:

- The conversion coefficient is bigger for nuclei with higher Z, because of the greater spatial overlap between the wave functions of the nucleus and the atomic electrons.
- The conversion coefficient decreases for electrons from atomic shells which are further from the nucleus, because the overlap of their wave functions with

the nucleus is less.

- The conversion coefficient increases as the transition energy decreases.

- The conversion coefficient varies with the transition multipolarity, and measuring it can allow the multipolarity of a transition to be determined.

More accurate calculations include relativistic effects and take into account the finite size of the nucleus. This work uses the `BrIcc` software [33] to calculate all theoretical conversion coefficients.

Conversion coefficients from `BrIcc` are plotted in figure 3.1 for E1, M1, E2 and M2 multipolarity transitions in nobelium. This shows the increase in α as the transition energy decreases or the multipolarity increases. When the transition energy reaches the binding energy of an atomic electron shell there is a jump in the conversion coefficient as it becomes possible for the nucleus to emit conversion electrons from this shell. In most cases electrons from the inner-most electron shell dominate the conversion coefficient as soon as the transition energy is greater than their binding energy, but for E2 transitions there is no jump in α at the K-shell binding energy and most conversion electrons are still emitted from the L-shell even for transitions above 149 keV.

Weisskopf estimates

Weisskopf estimates are a method to roughly calculate the transition probability for a particular γ decay [34]. The transition probability for a transition of multipolarity L and energy E_γ is given by

$$\lambda(\sigma L) = \frac{2(L+1)}{\hbar\epsilon_0 L[(2L+1)!!]^2}\left(\frac{E_\gamma}{\hbar c}\right)^{2L+1} B(\sigma L) \tag{3.23}$$

The quantity $B(\sigma L)$ is the reduced transition probability and is defined for electric and magnetic transitions respectively as

$$B(\mathrm{E}L) = \frac{1}{2J_\mathrm{i}+1}\left|\left\langle \mathrm{f}\right\| \widehat{Q}_L \left\|\mathrm{i}\right\rangle\right|^2 \tag{3.24}$$

$$B(\mathrm{M}L) = \frac{1}{2J_\mathrm{i}+1}\left|\left\langle \mathrm{f}\right\| \widehat{M}_L \left\|\mathrm{i}\right\rangle\right|^2 \tag{3.25}$$

where $\widehat{Q}_L$ and $\widehat{M}_L$ are the electric and magnetic multipole operators and $|\mathrm{i}\rangle$ and $|\mathrm{f}\rangle$ are the wave functions of the initial and final nuclear states. The Weisskopf estimate calculates $B(\sigma L)$ by making some simplifying assumptions about the decay:

- the transition involves only a single particle, which is assumed to be a proton.
- the wave functions of the initial and final states are those of independent particles in a spherically symmetric square well.
- the final state has no orbital angular momentum ($\vec{\ell} = \vec{0}$).

In cases where the assumptions involved in calculating the Weisskopf transition probability are not valid it will not provide a good estimate. For example, in a rotational band the collective nuclear motion means the assumption that only a single particle is involved in the transition is not correct and the estimate is a factor of ~ 100 less than the experimental E2 transition probability.

Transition probabilities in collective motion

Electromagnetic decay occurs between levels in a rotational band with $\Delta I = 1$ or $\Delta I = 2$. The decay between levels with $\Delta I = 2$ occurs only via stretched E2 transitions, but decay between levels with $\Delta I = 1$ can occur via either stretched M1 transitions or folded E2 transitions. The transition probabilities, $B(\mathrm{M1})$ and $B(\mathrm{E2})$,

for each of these can be calculated in the rotational model [15],

$$B(\mathrm{M1}; I \to I-1) = \frac{3}{4\pi}\left(\frac{e\hbar}{2mc}\right)^2 (g_K - g_R)^2 K^2 |\langle IK10 | (I-1)K\rangle|^2 \quad (3.26)$$

$$B(\mathrm{E2}; I \to I-1) = \frac{5}{16\pi} e^2 {Q_0}^2 |\langle IK10 | (I-1)K\rangle|^2 \quad (3.27)$$

$$B(\mathrm{E2}; I \to I-2) = \frac{5}{16\pi} e^2 {Q_0}^2 |\langle IK20 | (I-2)K\rangle|^2 \quad (3.28)$$

where g_K is the single-particle g factor, g_R is the collective rotational g factor and Q_0 is the electric quadrupole moment of the nucleus.

For the $\Delta I = 1$ decays the relative intensities of the M1 and E2 transitions is described by the mixing ratio,

$$\delta = \frac{0.93 E Q_0}{|g_K - g_R|\sqrt{I^2 - 1}} \quad (3.29)$$

where the transition, E, is in MeV and the intrinsic quadrupole moment of the nucleus, Q_0, is in eb. Through the rest of this work the $\Delta I = 1$ transitions within a rotational band are referred to as M1 transitions (and the $\Delta I = 2$ transitions as E2 transitions), but in all calculations the mixed M1/E2 nature is taken into account.

The M1 transition probability depends on $(g_K - g_R)^2$ so if the ratio of E2 and M1 transition intensities in a band can be measured it can be combined with the known g_R value to find two possible values of g_K. This helps to deduce the underlying single-particle structure of the band.

3.3 Isomers

Some excited states in nuclei are unusually stable against decay [36] and when their half-life is greater than about one nanosecond they are known as nuclear isomers. These excited states have longer half-lives because their decay is hindered by a significant change in the nuclear wave function. Isomers can be split into three types, each shown in figure 3.2, depending on what this change is [35, 37]:

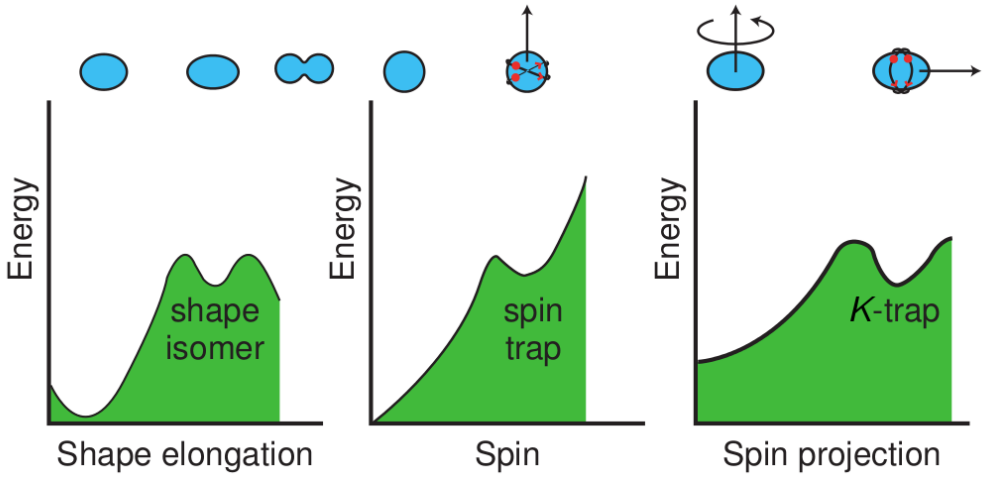

Figure 3.2: Nuclear excitation energy plotted against different nuclear properties to illustrate the three types of isomers: shape isomers, spin traps and K-traps. The shape of the nucleus and the angular momentum vectors are also shown. Taken from Walker and Dracoulis (1999) [35]

- Shape isomers, in which the change in shape between initial and final states hinders the decay.

- Spin-trap isomers, in which the change in spin between the initial and final states hinders the decay.

- K isomers, in which the change in direction of the nuclear spin (and therefore also its projection, K, onto the symmetry axis) between initial and final states hinders the decay.

K isomers are the most important of these three for the deformed nuclei around ^{254}No. Along with the area around hafnium this is one of the most important regions of the nuclear chart for the study of K isomers [38, 39].

K hindrance

For a transition of multipolarity L between two states with different K values a degree of K-forbiddenness is defined as

$$\nu = |\Delta K| - L \tag{3.30}$$

If K was a good quantum number and the projection of the angular momentum was always a conserved quantity then any transition with $\nu > 0$ would be forbidden. Mixing of states with different K values means transitions between them can happen, but they are hindered [40, 41]. For these transitions the ratio of the experimentally measured partial half-life, $t_{\frac{1}{2}}^{\mathrm{exp}}$ for the transition, and the half-life found from the Weisskopf estimate for the transition probability, $t_{\frac{1}{2}}^{\mathrm{W}}$, is called the hindrance factor,

$$F_{\mathrm{W}} = \frac{t_{\frac{1}{2}}^{\mathrm{exp}}}{t_{\frac{1}{2}}^{\mathrm{W}}} \tag{3.31}$$

There is a trend of $\log(F_{\mathrm{W}})$ increasing roughly linearly with ΔK for each different transition multipolarity [40, 42]. The reduced hindrance factor,

$$f_\nu = {F_{\mathrm{W}}}^{\frac{1}{\nu}} = \left(\frac{t_{\frac{1}{2}}^{\mathrm{exp}}}{t_{\frac{1}{2}}^{\mathrm{W}}} \right)^{\frac{1}{\nu}} \tag{3.32}$$

is roughly constant and values of f_ν in the range between 30 and 300 are typical for K-hindered decays [35].

Chapter 4

Previous knowledge and regional systematics

The synthesis of an element with atomic number $Z = 102$ was first reported in 1957 by a group of scientists bombarding ^{244}Cm with ^{13}C at the Nobel Institute in Stockholm [43]. The new element was named nobelium, in recognition of Alfred Nobel and the institute where the experimental work was carried out. Later experiments at Lawrence Berkeley National Laboratory (LBNL) and the FLNR in Dubna failed to replicate the original results, but ^{254}102 was identified by its α decay to ^{250}Fm at LBNL in 1958 [44]. With no further evidence to support the Nobel Institute results this is now recognised as the first synthesis of an isotope of element 102.

Early experiments to synthesise nobelium used fusion reactions of carbon beams on actinide targets, but production of transfermium nuclei now usually uses cold-fusion reactions of ^{48}Ca on lighter targets [45]. The cross section, σ_{xn}, for a fusion-evaporation reaction depends on the cross section, σ_{CN}, for fusion between the beam and target nuclei to produce the compound nucleus and also the probability, P_{xn}, of the compound nucleus surviving against fission and instead de-exciting by evaporation of light particles [46],

$$\sigma_{xn} = \sigma_{CN} \times P_{xn} \tag{4.1}$$

The cross-section for fusion decreases as the Coulomb barrier between the beam and target nuclei increases, giving very small cross sections to produce the heaviest nuclei.

In the reaction ^{208}Pb(^{48}Ca,2n)^{254}No both the target and beam are doubly magic, with closed shells of protons and neutrons and high binding energies. The compound nucleus is less tightly bound and much of the excitation energy from the fusion reaction goes into this change in binding energy. This leaves a colder compound nucleus than many other fusion-evaporation reactions with similar mass beams and targets and increases the probability of the compound nucleus decaying by particle evaporation not fission. This means the production of ^{254}No has a relatively high cross section (≈ 2 µb [47, 48]) compared to the production of other transfermium nuclei.

Figure 4.1 shows two proposed level schemes for ^{254}No. This chapter discusses previous work on different parts of the level scheme and the difference between the two proposals.

4.1 α decay

The ground state of ^{254}No has a 90(1) % branching ratio for α decay. The accepted values for the α decay energy and the half-life are $E_\alpha = 8.10(1)$ MeV and $t_{\frac{1}{2}} = 51.2(4)$ s [51, 52].

4.2 Ground-state rotational band

The ground-state band of ^{254}No was the first rotational band to be identified in a transfermium nucleus, using in-beam γ-ray spectroscopy at both Argonne National Laboratory [53] and JYFL [54]. Later experiments have observed levels in the band up to a spin of $24\hbar$ [55, 56]. Below the 4^+ state the transitions are too highly converted for any γ rays to be seen, but the transition energies can be extrapolated from a Harris fit [57] to the rest of the band.

Conversion electrons from the ground-state band transitions have also been seen at JYFL using the SACRED conversion electron spectrometer [58, 59]. L- and M-shell electron peaks were identified for the lower-energy transitions in the ground-state

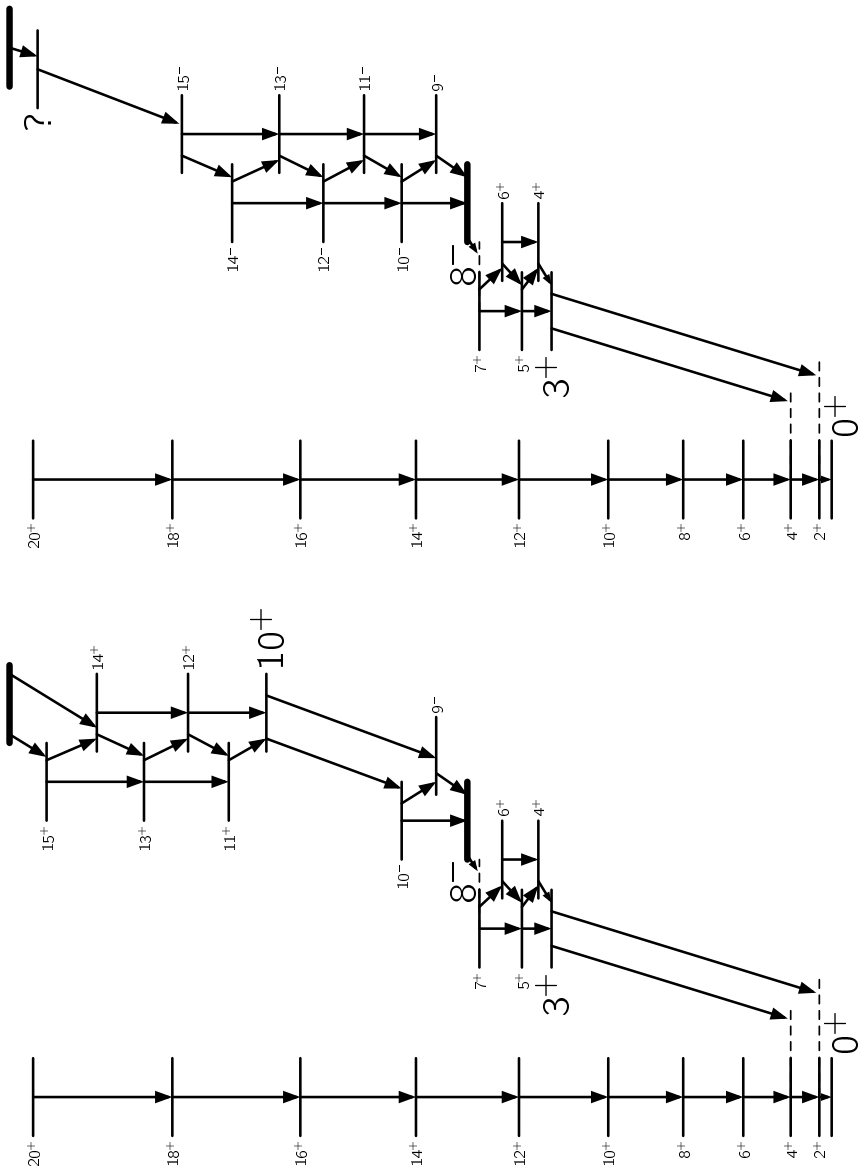

(a) Proposal from Clark et al. (2010) [49]. **(b)** Proposal from Heßberger et al. (2010) [50].

Figure 4.1: Proposed level schemes of ^{254}No from previous work. Labels show the spin and parity of each level and thicker lines mark the isomeric states.

band, including those from the $4^+ \rightarrow 2^+$ transition. There was also a large conversion electron background, which was suggested to be due to the existence of a high-K band with a cascade of highly converted M1 transitions which could not be individually resolved.

4.3 $K^\pi = 3^+$ band

The first non-yrast structure observed in ^{254}No was the 3^+ band [55, 60]. The prominent γ rays from the state's decay to the 2^+ and 4^+ levels in the ground-state band indicate that it has $K = 3$. The only possible two-quasiparticle structure giving the correct spin is the two-proton state,

$$\left\{ \tfrac{1}{2}^- [521]_\pi \otimes \tfrac{7}{2}^- [514]_\pi \right\}^{3^+}$$

The 3^+ state is not isomeric so recoil-decay tagging can't be used to identify prompt radiation above it, but it is populated by the decay of the slow isomer. γ rays in coincidence with the isomeric decay can be seen and placed in a rotational band built on the 3^+ state.

4.4 263 ms isomer

Ghiorso et al. [61] first suggested the presence of an isomeric state, with a half-life of 0.28(4) s, in ^{254}No in the 1970s, but it was not until about 30 years later that decay spectroscopy experiments [62, 63] confirmed its existence and determined its decay path.

The 53 keV decay to the 7^+ level in the 3^+ band is assumed from its intensity to have E1 multipolarity, meaning that the isomer has spin and parity $K^\pi = 8^-$. The three most likely possible structures are the two-proton state,

$$\left\{ \tfrac{7}{2}^- [514]_\pi \otimes \tfrac{9}{2}^+ [624]_\pi \right\}^{8^-}$$

or one of the two-neutron states,

$$\left\{\tfrac{7}{2}^{+}\,[624]_{\nu} \otimes \tfrac{9}{2}^{-}\,[734]_{\nu}\right\}^{8^{-}}$$
$$\left\{\tfrac{7}{2}^{+}\,[613]_{\nu} \otimes \tfrac{9}{2}^{-}\,[734]_{\nu}\right\}^{8^{-}}$$

In the rest of this work this isomer is referred to as the slow isomer.

4.5 183 μs isomer

^{254}No also has a second isomeric state with a shorter half-life of 183 μs [62, 63], referred to from now on as the fast isomer. The decay of this isomer feeds the levels built on the slow isomer. The excitation energy can be estimated from the total energy measured when the isomer decays and is higher than expected for any two-quasiparticle state. This suggests a four-quasiparticle structure, which could be formed by coupling together two of the 8^{-} two-quasiparticle excitations to give an isomer with $K^{\pi} = 16^{+}$ [62], or a spin/parity assignment of $K^{\pi} = 14^{+}$ has been proposed [63].

Decay spectroscopy experiments at LBNL [49] and GSI [50] have both observed γ rays of the same energies in coincidence with the decay of the fast isomer. Many of these have also been seen in recoil-isomer tagged spectroscopy of the slow isomer at JYFL. The 605 keV transition in the decay path of the fast isomer has also been seen in the in-beam spectra from JYFL [56]. If the transition is seen in the prompt spectra it can't directly depopulate the fast isomer and there must be some intermediate structure. Figure 4.1 shows the proposed level schemes from LBNL and GSI. The proposed level scheme from LBNL (figure 4.1a) has an extra 10^{+} state below the fast isomer which then decays by a 605 keV transition into a band built on the slow isomer [49]. The level scheme proposed from GSI (figure 4.1b) places all the observed γ rays into a single rotational band fed by the 605 keV transition from an unknown structure below the fast isomer [50].

Table 4.1: Two-quasiparticle isomers in even-even nuclei around $Z = 102$, $N = 152$.

	Nucleus	K^π	Energy /keV	Half-life	Configuration	
$N = 148$	^{244}Cm	6^+	1040	34 ms	$\frac{5}{2}^+[622]_\nu \otimes \frac{7}{2}^+[624]_\nu$	[64, 65]
	^{248}Fm			10.1 ms		[66]
	^{250}No	(6^+)		43 µs	$\frac{5}{2}^+[622]_\nu \otimes \frac{7}{2}^+[624]_\nu$	[67]
$N = 150$	^{246}Cm	8^-	1180	1.1 s	$\frac{7}{2}^+[624]_\nu \otimes \frac{9}{2}^-[734]_\nu$	[68]
	^{248}Cf	8^-	1261		$\frac{7}{2}^+[624]_\nu \otimes \frac{9}{2}^-[734]_\nu$	[69]
	^{250}Fm	8^-	1200	1.8 s	$\frac{7}{2}^+[624]_\nu \otimes \frac{9}{2}^-[734]_\nu$	[70]
	^{252}No	8^-	1250	110 ms	$\frac{7}{2}^+[624]_\nu \otimes \frac{9}{2}^-[734]_\nu$	[71]
	^{254}Rf	8^-	$\geq$ 1350	4.7 µs	$\frac{7}{2}^+[624]_\nu \otimes \frac{9}{2}^-[734]_\nu$	[72]
$N = 152$	^{248}Cm	8^-	1460	146 µs		[73]
	^{254}No	8^-	1300	263 ms		
	^{256}Rf		1120	25(2) µs		[74]
	^{256}Rf		1400	17(2) µs		[74]

4.6 Other K isomers around ^{254}No

K isomers are common in the region around ^{254}No, and table 4.1 lists details of some other known two-quasiparticle isomers in nearby even-even nuclei.

For the $N = 152$ isotones none of the isomers have had single-particle structures firmly assigned. For the 8^- isomer in ^{248}Cm the $B(\mathrm{M1})/B(\mathrm{E2})$ ratios from the data are not enough to give a structural assignment, but do not rule out the $\frac{7}{2}^+[624]_\nu \otimes \frac{9}{2}^-[734]_\nu$ two-neutron state [73]. In ^{256}Rf one experiment has identified three isomeric states [74] but these have not been confirmed in a later experiment [75] and none of the isomers have spin/parity assignments. ^{252}Fm is difficult to produce experimentally and no isomeric states are known.

The data for the $N = 150$ isotones is more complete and 8^- states with a two-neutron $\frac{7}{2}^+[613]_\nu \otimes \frac{9}{2}^-[734]_\nu$ structure have been assigned in ^{246}Cm, ^{250}Fm, ^{252}No and (more tentatively) in ^{254}Rf. In ^{248}Cf a state has been assigned the same configuration from single-nucleon transfer reaction data, but the half-life has not been measured. The reason for the much shorter half-life of the isomer in ^{254}Rf is not known.

Apart from ^{254}No the only known four-quasiparticle isomer in a transfermium

nucleus is in ^{254}Rf. It has a 16^+ spin/parity assignment and the structure is thought to be made from coupling an 8^- two quasi-proton state with an 8^- two quasi-neutron state [72], like the fast isomer in ^{254}No. The half-life of this isomer in ^{254}Rf is 247(73) µs, which is similar to the 183 µs half-life of the fast isomer in ^{254}No. An isomeric state in ^{256}Rf has been suggested to have a four-quasiparticle structure [75], but this is only based on its lower population ratio compared to that expected for a two-quasiparticle state.

K isomers are also common in the deformed nuclei around hafnium ($Z = 72$). The neutron numbers of these nuclei ($N \approx 104$) are similar to the proton numbers of the heavy actinides so some of the proton Nilsson levels are near the Fermi surface in nobelium are the same as the neutron Nilsson levels that are near the Fermi surface in the hafnium isotopes. There are 8^- isomers in ^{176}Hf [76] and ^{178}Hf [77]. In both these isotopes there are two possible 8^- configurations which are both seen experimentally, but only one is isomeric. In ^{178}Hf the two 8^- configurations couple together to form a 16^+ isomeric state and both ^{176}Hf and ^{178}Hf have 14^- four-quasiparticle isomers. Both the higher-lying isomers feed the 8^- levels and the situation for ^{254}No could be analogous to either.

Chapter 5

Experimental details

The experiment took place at the University of Jyväskylä Accelerator Laboratory (JYFL), using the SAGE/RITU/GREAT setup for recoil-tagged in-beam spectroscopy and decay spectroscopy. There were two separate beam times, the first in September 2013 and the second in January 2016, and table 5.1 gives some details for them both.

Production of ^{254}No used the fusion-evaporation reaction

$$^{208}\mathrm{Pb}(^{48}\mathrm{Ca}, 2\mathrm{n})^{254}\mathrm{No}$$

with a beam of $^{48}Ca^{10+}$ ions produced in the ECR ion source and accelerated by the K130 cyclotron [78] to a nominal energy of $E_{\mathrm{lab}} = 220$ MeV. The maximum cross section for the two-neutron evaporation channel in this reaction is at a beam energy of $E_{\mathrm{lab}} = 219$ MeV [47, 48], but the energy loss of the beam as it passes through

Table 5.1: Details of experimental conditions for the two beam times. The total numbers of recoil-tagged and recoil-isomer tagged events are also shown.

Run	HV barrier voltage /kV	Run time /hours	Average beam current /pnA	Recoil-tagged events	Recoil-isomer tagged events
2013	38	200	8	71000	5600
2016	Not working	31	10	7800	830
2016	28	7	5	1900	200
2016	32	66	10	18000	1900
Total		304		98700	8530

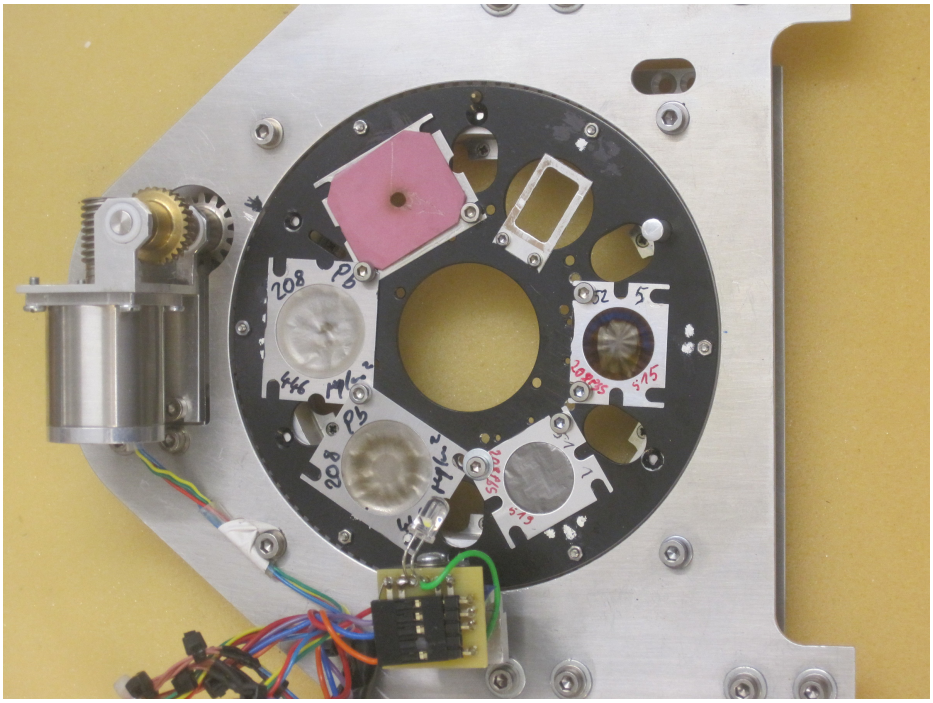

Figure 5.1: Target wheel for the second beam time. The target positions are numbered from zero to five moving clockwise from the top left position.

the target is roughly 2 MeV. With an initial energy of 220 MeV the beam energy at the centre of the target should be 219 MeV.

5.1 Targets

The SAGE target chamber contains a wheel which can hold up to six targets, shown in figure 5.1. The wheel rotates to move different targets into the beam line. The cyclotron operators use a viewer (position zero in figure 5.1) when they tune the beam and the empty frame (position one) can be used to check that the beam will not hit the frame of any of the other targets. The targets shown in figure 5.1 are two 520 µg/cm^2 ^{208}PbS foils (at positions two and three) and two 446 µg/cm^2 ^{208}Pb foils (at positions four and five). All four of these have a 50 µg/cm^2 carbon backing.

The target used for the second beam time was one of the 446 µg/cm^2 ^{208}Pb foils

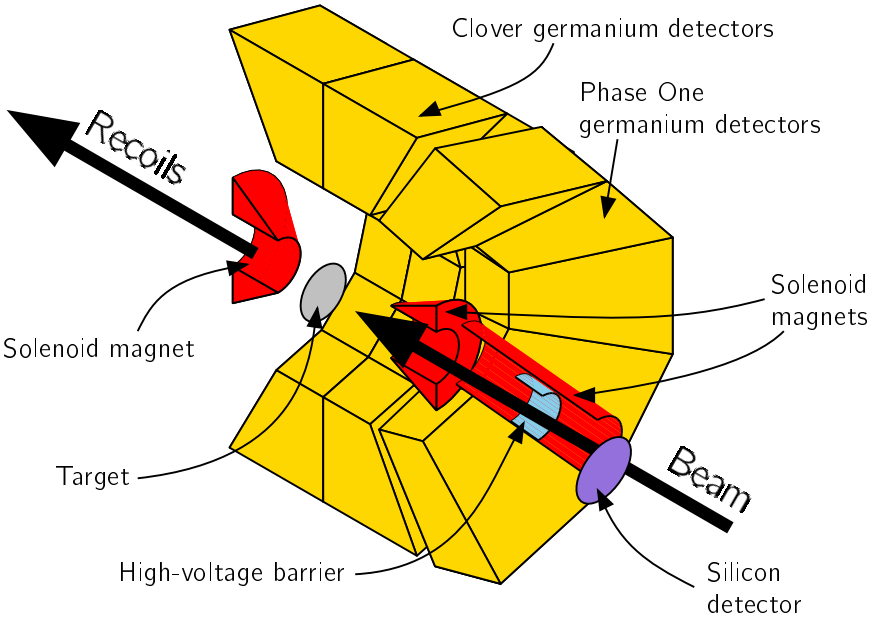

Figure 5.2: Cut-through diagram of half the SAGE spectrometer, showing the relative positions of the target, the silicon detector, the three rings of germanium detectors and the solenoids for electron transport.

(in position five). For the first beam time a 445 µg/cm^2 ^{208}Pb foil, without any carbon backing, was used.

5.2 SAGE – in-beam spectroscopy

The SAGE (Silicon And GErmanium) spectrometer [79, 80] measures prompt radiation emitted at the target position. It consists of both germanium detectors for measuring γ rays and a silicon detector to measure conversion electrons. A diagram of the parts of SAGE is shown in figure 5.2. Figure 5.3 shows photos of the spectrometer with the frame holding the germanium detectors in open and closed positions.

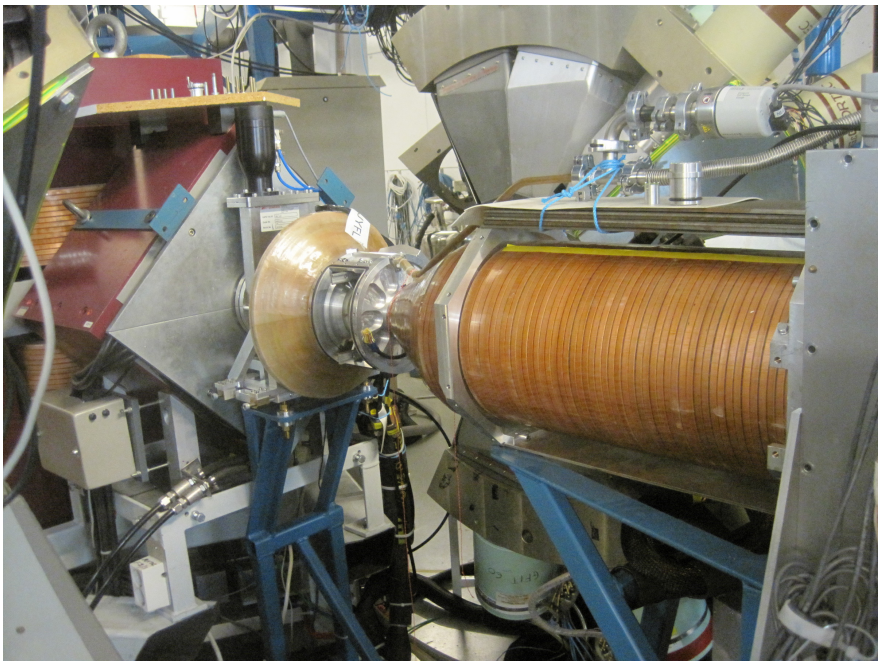

(a) With the germanium array open the SAGE target chamber and solenoid coils can be seen.

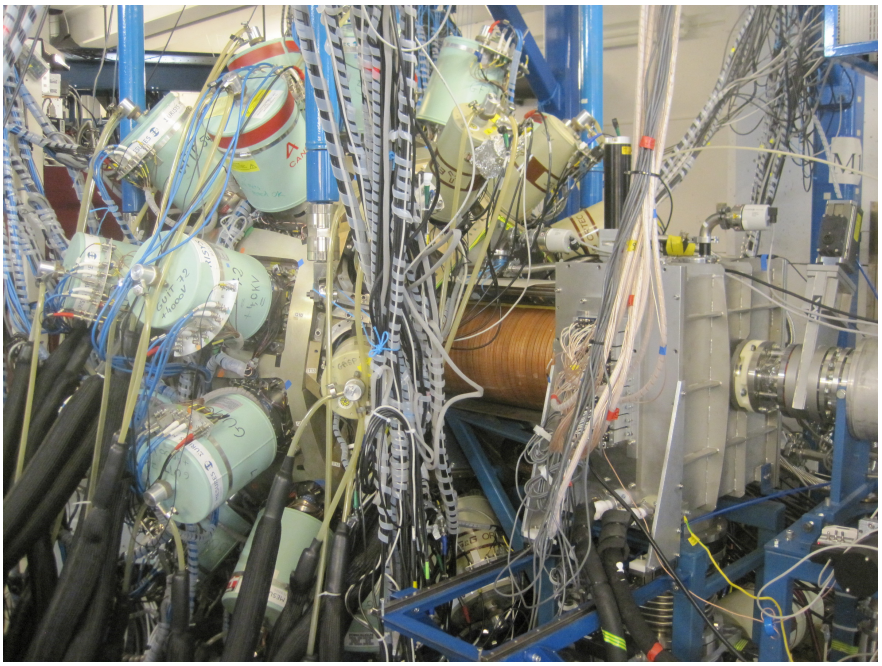

(b) With the germanium array frame closed the detectors are packed tightly around the target chamber and the solenoid coils.

Figure 5.3: Photos of the SAGE spectrometer with the frame holding the germanium detector array in open and closed positions.

Germanium detectors

For detection of γ rays SAGE uses high-purity germanium detectors from the Jurogam II array. There are two rings of clover detectors [81] at angles of 104.5° and 75.5° to the beam direction, with twelve detectors in each ring. Upstream of these, at 133.57° to the beam direction, is a ring of ten detectors of either GASP or Eurogam Phase One type [82]. Jurogam II normally has another ring of five Phase One detectors at the upstream end, but these must be taken out to make space for the SAGE solenoid coils. All the germanium detectors are cooled with liquid nitrogen to a temperature of around 80 K to reduce thermal noise.

The Phase One detectors contain a single germanium crystal, with a tapered shape so they can be packed together more closely. The clover detectors each contain four germanium crystals in the same cryostat. These can be used either as four individual detectors or in add-back mode where energy signals in adjacent crystals within a short time of each other are summed. If a γ ray scatters in one crystal and is then absorbed in a neighbouring crystal the add-back will reconstruct its full energy. This improves the efficiency of the detector for high-energy photons. All clover detectors at the target position used add-back for this experiment.

Each germanium detector is fitted with a bismuth germanate (BGO) escape suppression shield [83, 84]. This surrounds the sides and back end of the germanium crystal. Photons which scatter out of the germanium will also be detected in the BGO. The signal from the BGO vetoes hits from photons which do not deposit all their energy in the germanium detector and improves the peak-to-total ratio for the detector.

Silicon detector

For electron detection SAGE has a circular silicon detector with a diameter of 48 mm and a thickness of 0.3 mm. This is divided into 90 pixels in the arrangement shown in figure 5.4. The inner rings are 1 mm wide and the outer rings are 2 mm wide. The flux of incident electrons is higher closer to the centre of the detector so

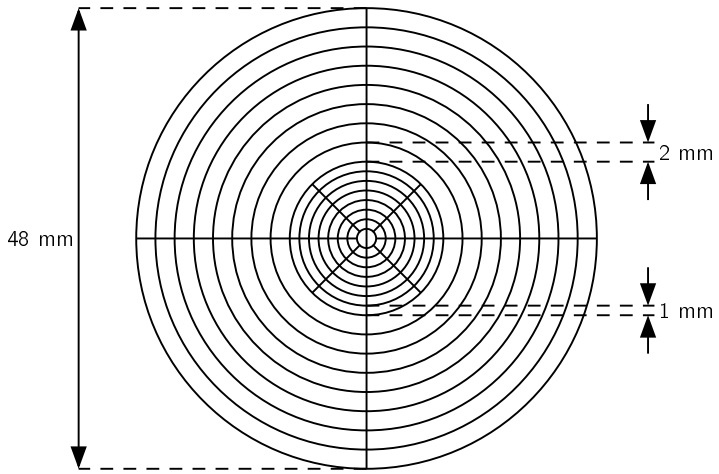

Figure 5.4: Arrangement of pixels on the SAGE silicon detector.

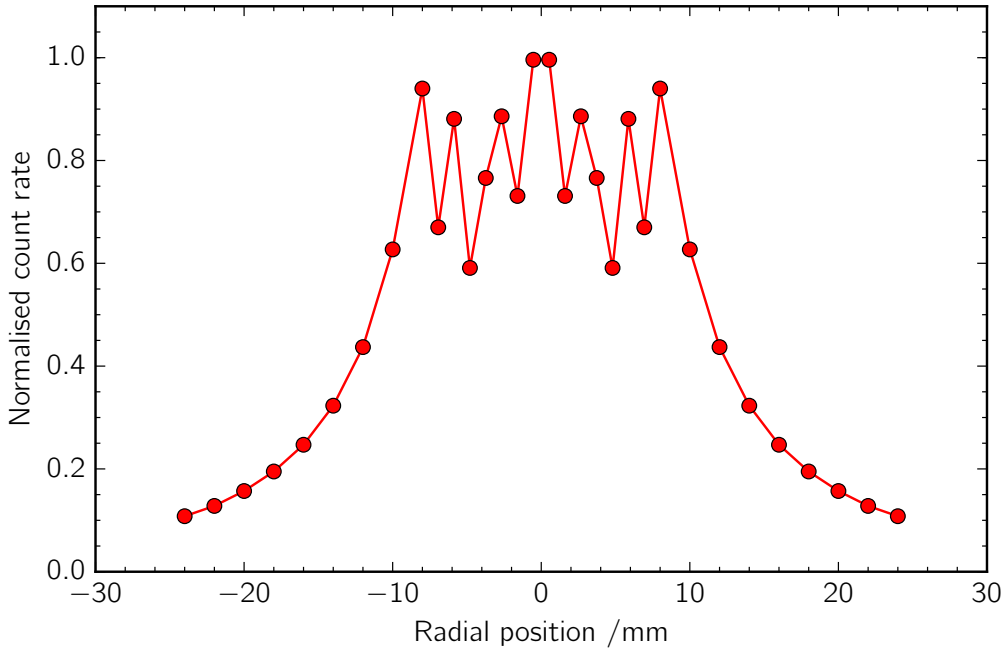

Figure 5.5: Calculated count rate distribution for the SAGE silicon detector. Count rates are normalised to the central pixels. Based on figure 3.32 of Papadakis (2010) [79].

the pixels here are smaller to try to even out the count rates between all pixels and maximise the total count rate. The count rate distribution in figure 5.5 shows how the rate is fairly even across the middle part of the detector.

The detector is mounted directly on a PCB which the pre-amplifiers are also attached to. The detector PCB is cooled to around −20°C with an ethanol-filled cooling circuit. This reduces thermal noise and reduces the detector leakage current [85].

Atomic interactions between the beam and the target produce a lot of low energy δ electrons. These are emitted mainly in the forward direction so the silicon detector is behind the target, at an angle of 177° to the beam direction, to reduce the number of δ electrons reaching it.

Magnetic field

Three solenoid coils create a magnetic field inside SAGE to transport electrons from the target position to the silicon detector. One of the coils is downstream of the target and acts like a mirror to reflect electrons back towards the silicon detector. The other two coils are upstream of the target and create the magnetic field to transport electrons from the target position to the detector [79].

High-voltage barrier

The δ-electron background in SAGE is mainly at low energies so to reduce the amount of it reaching the silicon detector there is a high-voltage barrier (shown in figure 5.6) inside the solenoid coil between the target and the detector chamber [80]. The potential difference between the barrier electrode and the grounded outer sleeve creates an electric field which prevents low-energy electrons reaching the silicon detector. For the first beam time the barrier voltage was −38 kV. During the second beam time there were problems with the barrier discharging and for the first part of the experiment it was not used and the silicon detector also had to be turned off. The barrier was then replaced with a new one and operated at −28 kV or −32 kV for different parts of the remaining beam time.

Figure 5.6: High-voltage barrier from SAGE. The stainless steel electrode is the central cylinder. It is surrounded by a Noryl resin insulator and an aluminium grounding sleeve. This is the barrier that had to be replaced in the second beam time and the black mark on the insulator (circled at top of picture) is probably from the barrier discharging by sparking. The outer diameter of the barrier is 146 mm.

Carbon foils

The high-voltage barrier and the silicon detector are in the same high-vacuum volume ($\approx 10^{-6}$ mbar) as the accelerator beam line, but the target position is connected to RITU (section 5.3) which is filled with helium gas at a pressure of 0.5 mbar. To separate these volumes there are two 50 µg/cm^2 carbon foils upstream of the target chamber with the volume between the foils pumped to an intermediate pressure. A single foil of this thickness is not enough to maintain the pressure difference and thicker foils reduce the transmission efficiency for electrons from the target to the detector. If the carbon foils were downstream of the target they would reduce the transmission efficiency for recoiling ions entering RITU. The location of the foils also means that the targets are in the helium gas which fills RITU which helps to cool them so they can withstand higher-intensity beams.

5.3 RITU – recoil separation

The small cross sections for production of superheavy nuclei mean it is necessary to separate recoiling ^{254}No nuclei from unreacted beam particles and nucleon-transfer reaction products. At JYFL this is done using the RITU (Recoil Ion Transfer Unit) gas-filled recoil separator [86, 87].

Recoil separators use different combinations of electric and magnetic fields to separate charged particles based on their mass, velocity or momentum. Gas-filled separators use a dipole magnet to separate particles with different momentum. Charged particles passing through the magnetic field of the dipole are deflected with a bending radius

$$r = \frac{mv}{qB} \tag{5.1}$$

where m is the particle's mass, v is its velocity, q is its charge and B is the magnetic field strength. conservation of momentum in the fusion-evaporation reaction means beam particles and ^{254}No recoils have similar momenta, but the beam particles are lighter and have a higher velocity. The separator is filled with low-pressure (0.5 mbar)

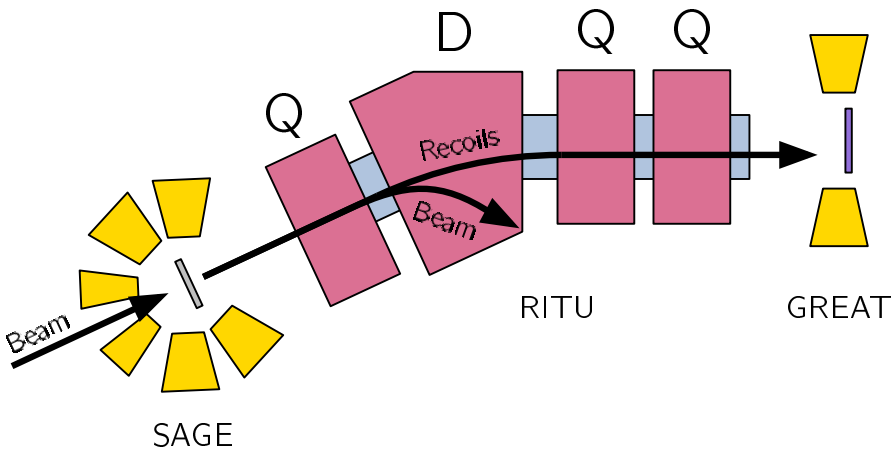

Figure 5.7: Diagram of the RITU gas-filled recoil separator, seen from above. The magnets in RITU are labelled (with D for the dipole magnet and Q for the quadrupole magnets) and the positions of SAGE and GREAT are shown.

helium gas and when recoiling ions and helium atoms collide electrons are exchanged between. Over time the average charge state of ions travelling through the gas is [88]

$$q_{\text{ave}} = \frac{v}{v_{\text{B}}} eZ^{1/3} \tag{5.2}$$

where v is the ion's velocity and $v_{\text{B}} = c/137$ is the Bohr velocity. The faster-moving beam particles have a higher average charge state than the ^{254}No recoils and, from equation 5.1, their paths are bent more in the separator. Instead of passing through to the focal plane they hit a beam dump in the dipole magnet chamber.

Collisions with the gas in the separator also mean all recoiling ^{254}No ions have the same time-averaged charge and the bending radius of their paths does not depend on their charge state when they enter the separator. This increases the transmission efficiency of the separator compared to vacuum-mode separators, which only focus a single charge state to the focal plane. For transfermium nuclei RITU has an estimated transmission efficiency to the GREAT MWPC of 47(4) % [89].

The most common arrangement of magnetic fields in a gas-filled separator is DQQ,

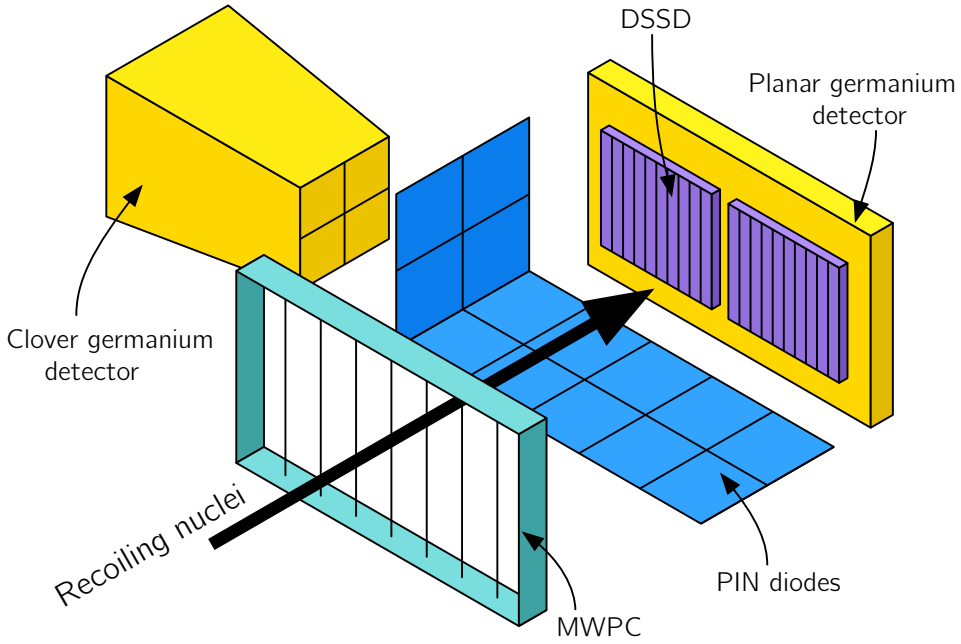

Figure 5.8: Arrangement of the main parts of GREAT. For clarity two of the clover detectors and half the PIN diodes are not shown.

with the main bending dipole magnet, D, followed by two quadrupole magnets, Q, for focusing the recoils horizontally and vertically onto the focal plane of the separator. RITU uses a QDQQ arrangement (shown in figure 5.7) with an extra quadrupole magnet at the upstream end to improve the angular acceptance of the separator when it is used with an array of detectors around the target position.

5.4 GREAT – decay spectroscopy

After travelling through RITU the recoiling nuclei enter the GREAT (Gamma Recoil Electron Alpha Tagging) spectrometer [90]. They pass through a multi-wire proportional counter and are implanted into a double-sided silicon strip detector. When the nuclei decay the energy of any emitted α particles, γ rays or conversion electrons can be measured in the silicon detector or the PIN diodes and germanium detectors positioned around it. Figure 5.8 shows the main parts of GREAT.

Double-sided silicon strip detector

The double-sided silicon strip detector (DSSD) records the energy of implanting recoils and their subsequent decays. It consists of two 60 mm × 40 mm, 300 μm thick silicon detectors with a 4 mm gap between them. The front of each detector (the side facing into RITU) is divided into 1 mm wide vertical strips and the back is divided into 1 mm horizontal strips. The x and y co-ordinates from these strips gives the location of any implantation or decay in one of a total of 4800 pixels. The high granularity of the detectors reduces the probability of random correlations between implantations and decays of different nuclei in the same pixel when recoil-decay tagging (section 6.1) is used. The amplifier gains for the DSSD are set for observation of isomeric electron decays ($E < 1$ MeV) on the front side (DSSD-X) and α decays and recoils ($E \approx 5$–20 MeV) on the back (DSSD-Y).

The shape and size of the DSSD mean it only covers 85 % of the distribution of recoils reaching the focal plane [90]. Combining this with the transmission efficiency of RITU the total efficiency for detection of recoiling ions is about 40 %. When a nucleus in the DSSD decays particles can be emitted in any direction. In α decay the half of the α particles are emitted back towards RITU and escape from the DSSD without giving any signal in it so the detection efficiency is only around 50 %. For detection of a conversion electron cascade from an isomeric decay (for recoil-isomer tagging, section 6.1) the detection efficiency is higher because not all electrons are emitted in the same direction and even if some escape others will be detected. Simulations give a detection efficiency of 85 % for the decay of the 8^- isomer in ^{254}No with the DSSD-X energy thresholds set at 50 keV [91].

Multi-wire proportional counter

To discriminate between recoil implantation events and their subsequent decays there is a 131 mm × 50 mm multi-wire proportional counter (MWPC) which recoils pass through before implanting in the DSSD. For recoil events there are coincident signals in the DSSD and MWPC, but for a decay there is a signal in the DSSD only.

The detection efficiency of the MWPC for particles which pass through it is almost 100 % and it is bigger than the DSSD so all recoil implantation signals in the DSSD will also have a signal from the MWPC [87].

PIN diodes

Upstream of the DSSD is a box of 28 silicon PIN diodes. Some of the α particles or conversion electrons emitted by implanted recoils which escape from the DSSD will be detected by the PIN diodes. This improves the total efficiency for detecting these decays in GREAT.

Planar germanium detector

The planar germanium detector measures X-rays and low-energy γ rays. It has a thickness of 15 mm and an area of 120 mm $\times$ 60 mm, divided into 5 mm $\times$ 5 mm pixels. To reduce any attenuation of γ rays emitted from particles implanted in the DSSD the planar detector is only about 10 mm behind it and has a thin beryllium entrance window.

Clover germanium detectors

Three clover germanium detectors are positioned around GREAT to measure higher-energy γ rays. One of these is above the DSSD and the other two are either side of it. The clovers are similar to those at the target position (described in section 5.2) but the crystals in each are used as four individual detectors without add-back.

5.5 Electronics and data acquisition

Figure 5.9 shows a diagram of the data acquisition system at JYFL. The DSSD uses analogue electronics with signals sent to shaping amplifiers and constant fraction discriminators to determine their energies and times and then to VXI time-stamping analogue-to-digital converters (ADCs). All other detector channels use fully digital electronics. Signals from the detector pre-amplifiers are sent through gain and offset

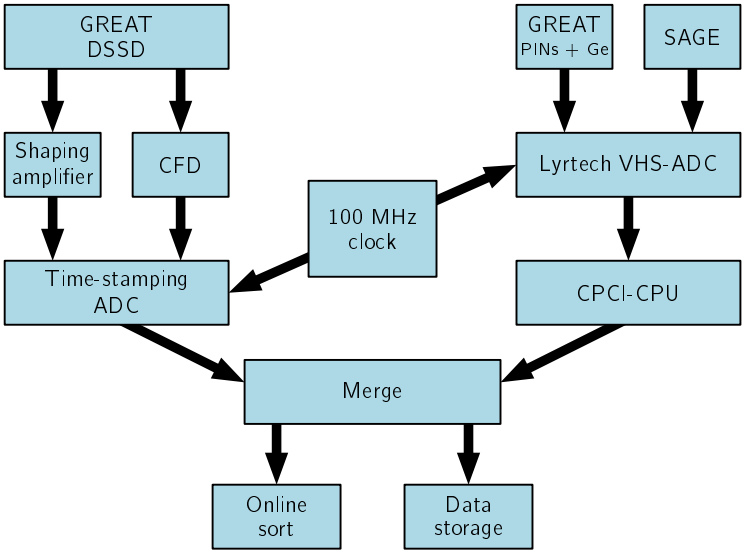

Figure 5.9: Signal processing for TDR data acquisition at JYFL.

(GO) boxes to Lyrtech ADCs with 14-bit resolution and a 100 MHz sampling rate. The ADCs use a moving-window deconvolution algorithm [92] to find the signal energies and times.

Using digital electronics each channel in SAGE can count at rates up to around 30 kHz. Count rates at the focal plane are much lower (because there is much less background) and faster signal processing is not as important but digital electronics give better resolution and a more linear energy response at low energies.

In a traditional recoil-decay tagging experiment (section 6.1) a common trigger is used for all channels. This leads to high dead times, particularly when tagging on longer-lived states. To overcome this problem JYFL uses the total data readout (TDR) system [93]. Each channel triggers individually and the data is stamped with a time signal (with a 10 ns resolution) and its channel number before being sent to a common data stream and written to disk. The dead time for each channel depends only on the intrinsic dead time of each individual detector. For data analysis the `Grain` data-sorting software [94] reconstructs events from the data stream, with the

triggering channel and the event time delay and width defined in software. In the analysis from this experiment the trigger was any DSSD strip, with 4 μs long events starting 2 μs before the DSSD signal.

5.6 Calibration

Energy calibration

All germanium detectors were calibrated using sealed ^{152}Eu and ^{133}Ba sources. For the SAGE silicon detector open ^{133}Ba and ^{207}Bi sources were used. An open ^{133}Ba source was also used for DSSD-X and the PIN diodes. A mixed α source containing ^{239}Pu, ^{241}Am and ^{244}Cm was used to calibrate DSSD-Y. The source was outside the DSSD so α particles from it lost around 60 keV of energy passing through the detector dead layer. For α decay of nuclei implanted into the DSSD this did not occur and all the α particle energy was absorbed by the detector. This shifts the energies of observed α-decay peaks to around 60 keV higher than expected. The energy loss of electrons in the detector dead layer is negligible [95] so no adjustments are needed for the DSSD-X calibration. Calibration coefficients were calculated for each detector channel from a quadratic fit to raw peak centroids and known peak energies [96], except for DSSD-Y where there were only three degrees of freedom in the fit (from only three data points) and a linear fit was used.

Efficiency calibration

The efficiency of the detectors in SAGE was measured using the same radioactive sources as the energy calibration. For the sealed sources absolute efficiencies were found using measured activities of the sources corrected for the decay since the time of measurement. For the open electron sources the activity was not known so the germanium detectors were used to measure the activity of the sources to calibrate the silicon detector efficiency.

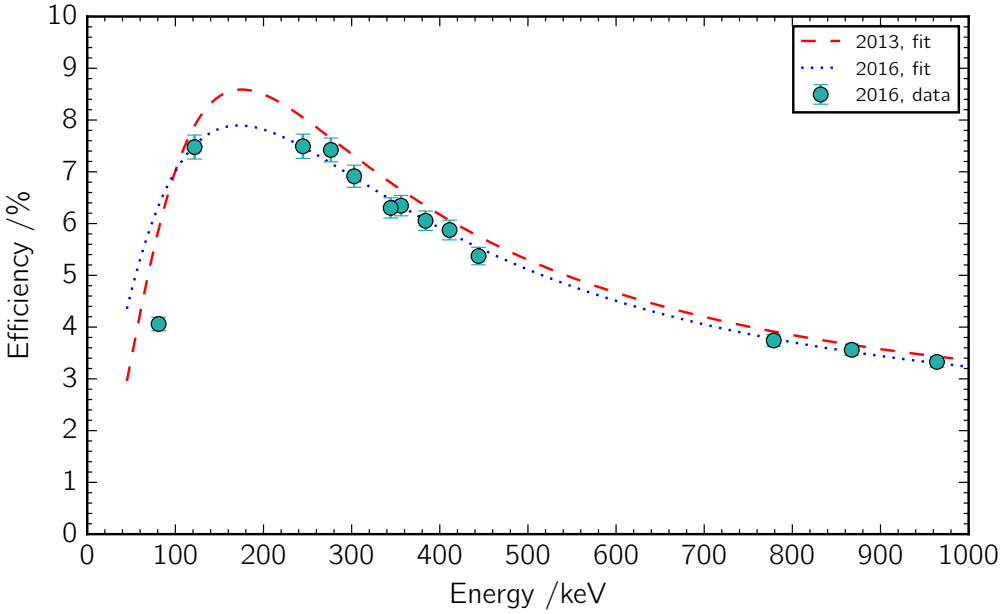

(a) Fitted efficiency curves for the germanium detectors in the two beam times.

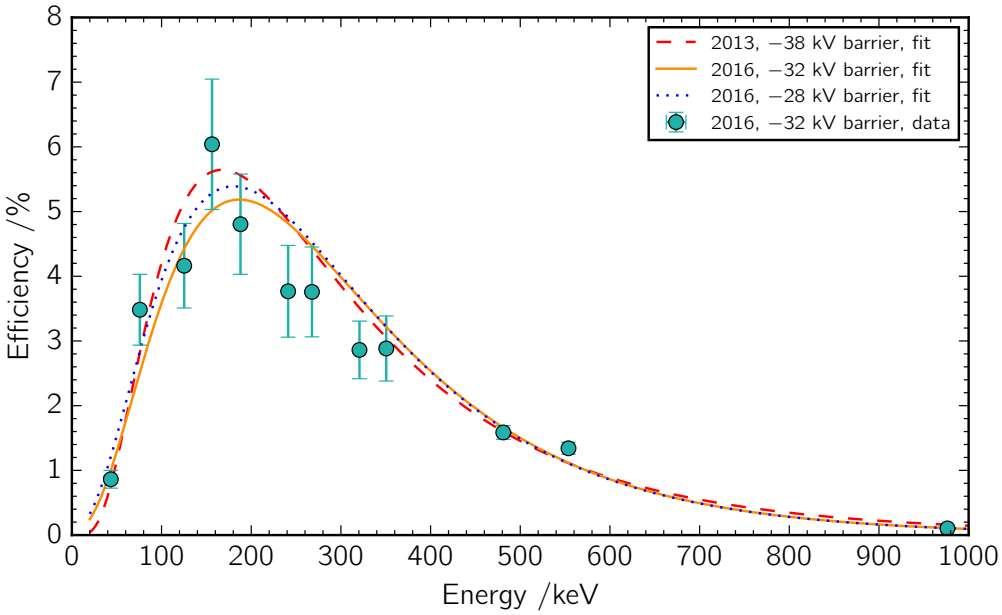

(b) Fitted efficiency curves for the silicon detector in the two beam times with the different voltages on the HV barrier. Increasing the barrier voltage reduces the efficiency at low energies but the data for −38 kV was taken in a different beam time when the overall detector efficiency was higher. The different size error bars on the experimental data points are because the ^{133}Ba and ^{207}Bi data were not measured for the same length of time.

Figure 5.10: Fitted efficiency curves for SAGE silicon and germanium detectors. Experimental data points are also shown for one set of data in each case.

Table 5.2: Values of the parameters for the curves fitted to the SAGE detector efficiency data.

(a) For the germanium detectors, using equation 5.3.

Run	A	B	D	E	F
2013	4.75	3.1	3.54	-0.63	0.16
2016	4.54	2.37	3.53	-0.64	0.15

(b) For the silicon detector, using equation 5.4.

Run	HV barrier /kV	a	b	c	d	e
2013	38	-25.5	10.3	-0.94	-0.0038	-0.0007
2016	28	2.53	-5.85	2.16	-0.21	-0.0002
2016	32	1.89	-5.76	2.18	-0.21	-0.0004

The curve fitted to the efficiency data for the germanium detectors has the form

$$\log(\epsilon) = \left[(A + Bx)^{-3} + (D + Ey + Fy^2)^{-3}\right]^{-1/3} \tag{5.3}$$

where ϵ is the efficiency, $x = \log(E_\gamma/100)$, $y = \log(E_\gamma/1000)$ and E_γ is in units of keV [97].

The curve fitted to the efficiency data for the silicon detector has the form

$$\log(\epsilon) = a + bx + cx^2 + dx^3 + ex^4 \tag{5.4}$$

where $x = \log(E_\gamma)$ [98].

Figure 5.10 shows the fitted efficiency curves and table 5.2 lists their parameters. The efficiency of the germanium array changes when individual detectors within it are swapped so efficiency curves were found separately for each beam time. For the silicon detector the efficiency at low energies depends on the operating voltage of the high-voltage barrier so separate efficiency measurements were made for each barrier voltage. When they were used in the data analysis the efficiency curves for each part of the experiment were scaled by the number of recoils in that part and added together.

Efficiency curves from `GEANT` simulations by Andreyev et al. [91] were used for the

detectors in GREAT.

Time resolution

Although the data acquisition electronics have a time resolution of 10 ns the intrinsic time resolutions of the detectors is not this good. The measured time resolutions are around 65 ns for the SAGE germanium detectors and 50 ns for the silicon detector pixels. Using `Grain` the timing of each detector channel can be shifted backwards or forwards by multiples of 10 ns. This can be used to correct for any difference in timing (for example from differences in cabling) between different elements within SAGE or GREAT.

Doppler correction

SAGE is calibrated with a source fixed at the target position, but ^{254}No recoils move through the spectrometer as they leave the target. The energies of γ rays are Doppler shifted by different amounts depending on their emission angle relative to the recoil's direction. The shifted energy, E', is related to the energy in the frame of the recoiling nucleus, E, by the equation,

$$E' = E\,(1 + \beta \cos\theta) \tag{5.5}$$

where θ is the angle between the emitted γ ray and the beam direction and $\beta = \frac{v}{c}$ with v = recoil velocity and c = the speed of light. The value of β is found by looking at the energy shift of γ rays observed in the three rings of germanium detectors, which are at different angles to the beam direction.

For the silicon detector the Doppler shifted energy must also take into account the rest mass of the electron, m_e,

$$E' = \frac{E + m_e + \beta \cos\theta \sqrt{E^2 + 2m_e E}}{\sqrt{1 - \beta^2}} - m_e \tag{5.6}$$

The emission angle of electrons is not known, because of the magnetic fields

used to transport them to the SAGE silicon detector. Simulations of the SACRED spectrometer [99] showed that 150°–160° was the most common emission angle for electrons reaching the detector, so a value of $\theta_{\text{ave}} = 150°$ is used for the Doppler correction of all SAGE pixels.

Chapter 6

Data analysis and simulations

6.1 Recoil-decay tagging

Most of the radiation at the target position is background and it is necessary to identify any γ rays or conversion electrons from ^{254}No within this. Recoil-decay tagging (RDT) [100–102] identifies prompt radiation from ^{254}No recoils which reach the focal plane. When recoiling ^{254}No nuclei from the target position reach GREAT they pass through the MWPC and are then implanted into the DSSD. Gating on the particle's time of flight (ToF) from the MWPC to the DSSD and its energy loss (dE) as it passes though the MWPC discriminates between fusion-evaporation recoils and any contamination from unreacted beam which is not removed by RITU. The α decay of ^{254}No is then identified by its energy,

$$7.8 \text{ MeV} < E_\alpha < 8.2 \text{ MeV}$$

and correlated with a recoil implantation event in the same DSSD pixel within around five half-lives earlier,

$$\Delta t < 275 \text{ s}$$

Data is only taken from the detectors at the target position in coincidence with a correlated recoil (taking into account flight time through RITU). Figure 6.1a shows this schematically and figure 6.2 shows the effect on the SAGE germanium detector spectrum.

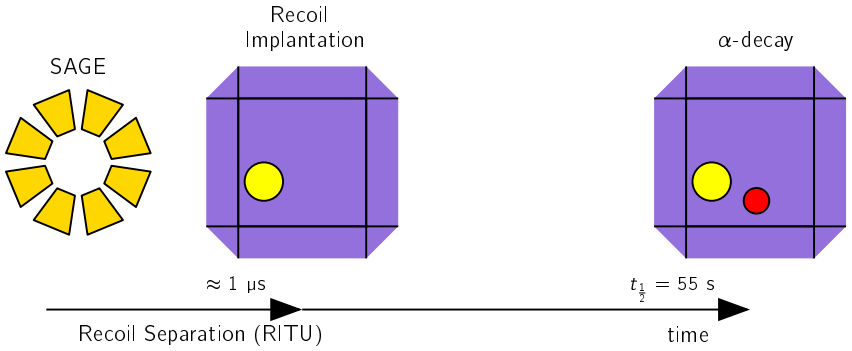

(a) Recoil-decay tagging on ^{254}No α decay

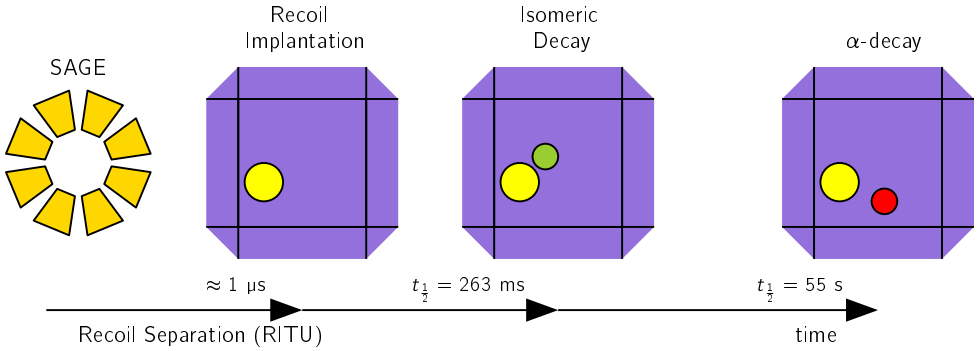

(b) Recoil-isomer tagging on conversion electrons from decay of the slow isomer

Figure 6.1: Schematic diagrams of recoil-decay tagging using correlations between recoil implantations and decays in a single DSSD pixel.

For the ^{208}Pb + ^{48}Ca reaction the cross section for 2n evaporation is so much bigger than for any other channel that taking prompt data for any recoil which passes the ToF-dE gate, without requiring a correlated α-decay, gives a recoil-tagged spectrum (figure 6.2) with no contamination from other reaction channels. Comparing this with the recoil-decay tagged spectrum confirms that it has no extra peaks from contaminant channels, but the recoil-tagged spectrum has more counts making it easier to identify and fit peaks in it.

Recoil-isomer tagging

Figure 6.1b shows a variation of the RDT technique which tags on the decay of an isomeric state, identified by the emitted cascade of conversion electrons in

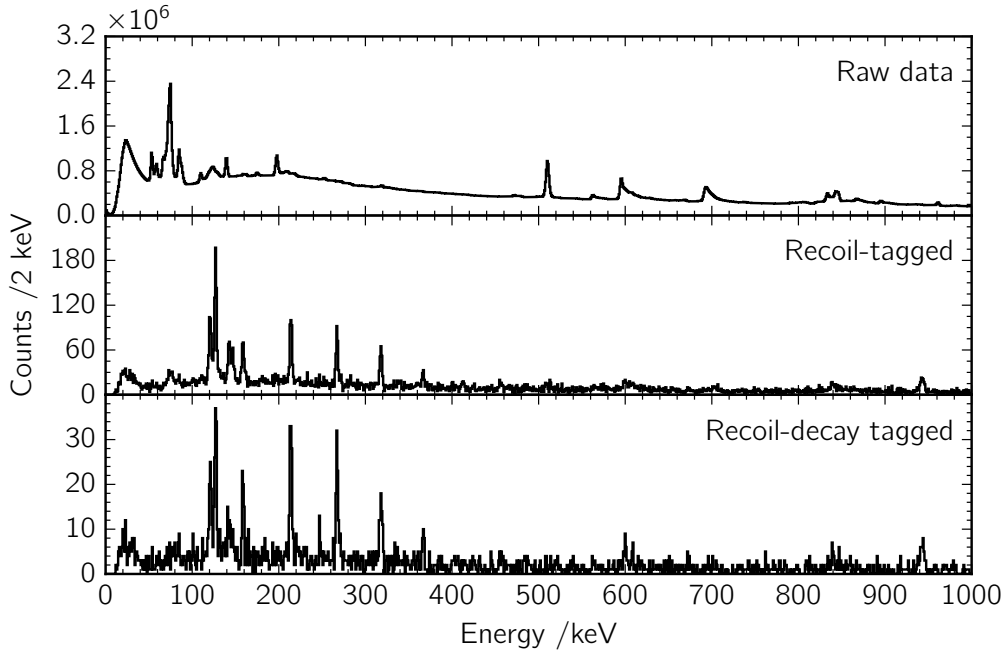

Figure 6.2: Effect of applying recoil tagging and recoil-decay tagging to data from the SAGE germanium detectors.

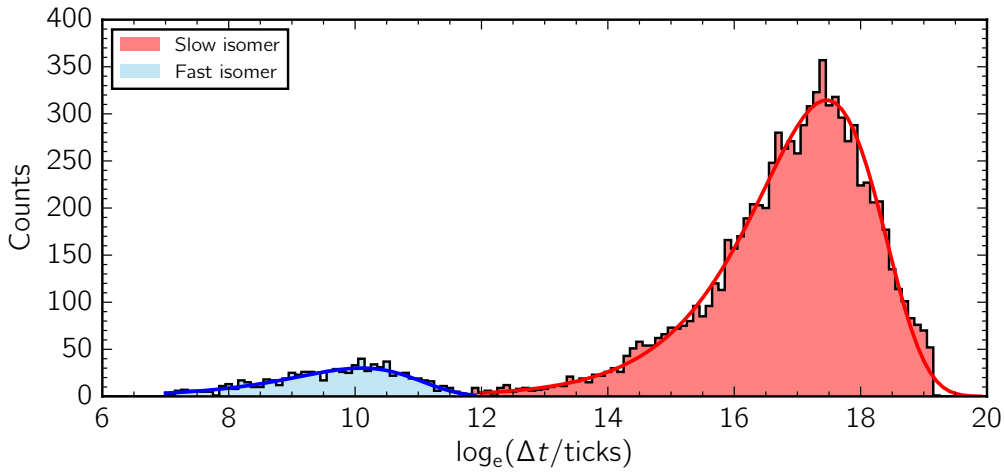

Figure 6.3: Log of the time difference between recoil implantations and isomeric decays, showing peaks from the two isomers in ^{254}No separated by their different half-lives. Fits to the two peaks are also shown and the time gates used to identify each of the isomers are shaded.

the DSSD, instead of an α decay [103]. Tagging on correlated chains of recoil $\rightarrow$ isomer $\rightarrow \alpha$ decay can be used to confirm that the recoil-isomer tagged spectrum is free of contamination in the same ways as recoil-decay tagging is used to check recoil-tagged data.

The two isomeric states in ^{254}No can be separated by tagging on chains of recoil $\rightarrow$ isomer $\rightarrow$ isomer and by their different half-lives. The time distribution of any radioactive decay follows an exponential decrease,

$$\frac{\mathrm{d}N}{\mathrm{d}t} = N\lambda \mathrm{e}^{-\lambda t} \tag{6.1}$$

and making the substitution $\theta = \log_{\mathrm{e}}(t)$ transforms this into

$$\frac{\mathrm{d}N}{\mathrm{d}\theta} = N\lambda \mathrm{e}^{-\lambda \mathrm{e}^{\theta}} \mathrm{e}^{\theta} \tag{6.2}$$

which is a peak with a shape independent of the decay half-life [104]. The height of the peak depends on the number of decays, N, and its position depends on the half-life, with the centroid at $\log_{\mathrm{e}}(1/\lambda)$. Using logarithms means that a single time distribution can show peaks from decays with half-lives which vary by several orders of magnitude. Figure 6.3 shows the time distribution for isomeric decays in ^{254}No, with two separate peaks from the two isomers. The fitted curves give a half-life for the slow isomer of

$$t_{\frac{1}{2}} = 266 \text{ ms}$$

and for the fast isomer

$$t_{\frac{1}{2}} = 170 \text{ µs}$$

The time gate for recoil-decay correlations for the slow isomer is

$$1.5 \text{ ms} < \Delta t < 2200 \text{ ms}$$

and for the fast isomer

$$\Delta t < 1.5 \text{ ms}$$

The slow isomer is identified from recoil → slow isomer chains but the identification of the fast-isomer uses recoil → fast isomer → slow isomer chains. The energy gate for isomeric decays is set separately for each DSSD-X channel to be the total useful range above electronic noise and below overflow.

6.2 SAGE background subtraction

Even after using RDT to identify prompt radiation in SAGE the silicon detector spectrum still contains a lot of background. The background is also seen outside the recoil-SAGE time gate (figure 6.4a) so extra time gates before and after the prompt radiation are used to fill background spectra. After normalising the background spectra to the prompt radiation spectrum using the relative widths of the time gates they are subtracted from the prompt SAGE electron spectrum. This leaves a spectrum containing only electrons associated with ^{254}No. Figure 6.4b shows spectra before and after this background subtraction. Some background is still left but this is from unresolved transitions in ^{254}No feeding into the ground-state band [58].

The spectra from the SAGE germanium detectors have much less background and more significant peaks so the prompt spectra in coincidence with ^{254}No recoils are used without any background subtraction.

6.3 Peak fitting

Peaks in the spectra are fitted using the `tv` software package [105]. A polynomial background can be fitted either side of the peak. The fit is weighted using the uncertainties on the numbers of counts in each bin of the spectrum and `tv` can calculate the uncertainties using either a Gaussian or a Poisson distribution [106]. The Poisson distribution is better for peaks with small numbers of counts. The fitted peak areas are corrected for detector efficiency using the efficiency curves from

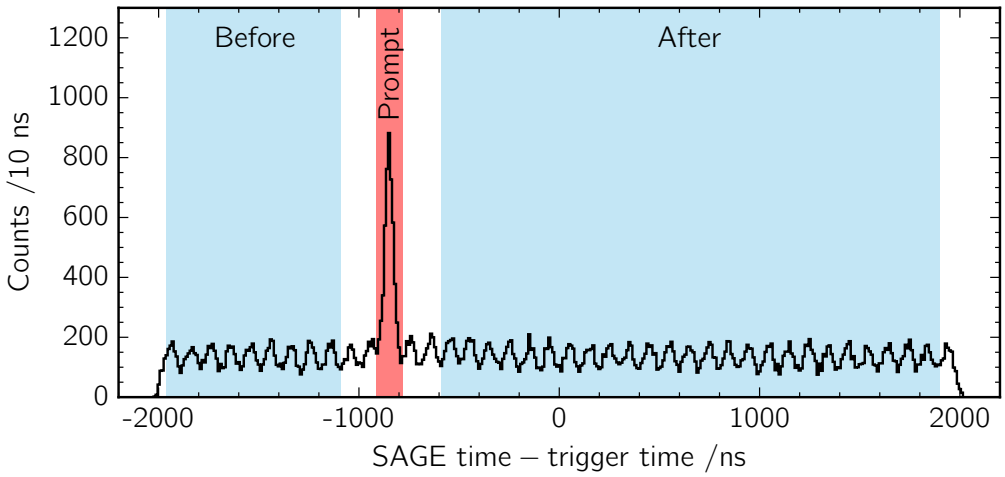

(a) SAGE silicon detector hit times within recoil-tagged events. The shaded areas show the gates for prompt hits and background before and after this.

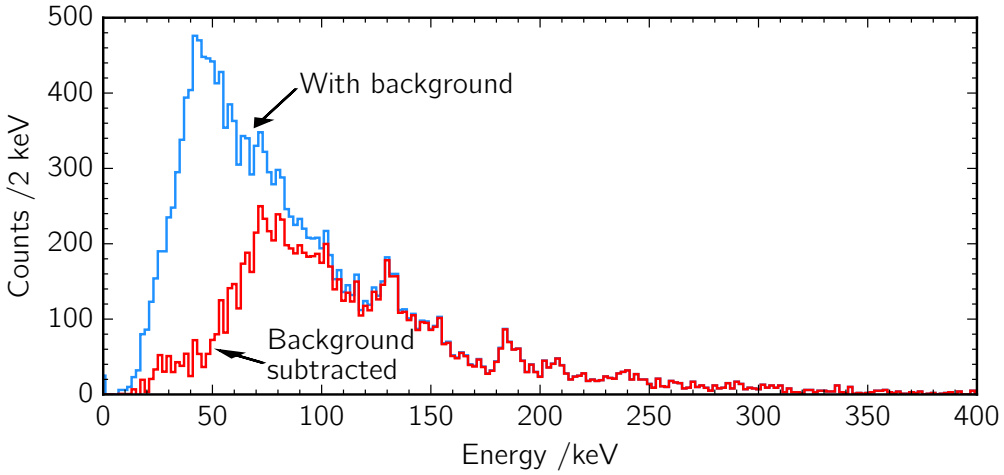

(b) Energy spectrum from the SAGE silicon detector with and without background subtraction.

Figure 6.4: Time gating and background subtraction for SAGE silicon detector spectrum.

section 5.6 to find the intensities.

6.4 Geant4 simulations

To help with interpretation of experimental results a Geant4 simulation package for the SAGE spectrometer is available [107, 108]. Geant4 is a software toolkit which uses Monte Carlo methods to simulate the transport of particles and their interactions with matter [109]. The simulation package for SAGE uses Geant4 to reconstruct the geometry of the spectrometer and the electromagnetic fields inside it. It takes input data files describing possible level schemes, generates γ rays and conversion electrons with the correct energies. These are then tracked through the spectrometer and simulated energy spectra from the silicon and germanium detectors are produced. Simulations used in this work have been run with Geant4 version 10.0.4 with the emstandard_opt4 physics list.

Simulations can be run for many more events than it is possible to collect experimental data for so the differences between the spectra for different possible level schemes can be seen more easily. It is also possible to use the simulation to investigate the performance of the spectrometer. The energy deposited in non-sensitive parts of the spectrometer (for example the target wheel) can be found and different parts of the geometry (for example silicon detector dead layers or the carbon foil unit) can be turned on or off to see their effect on the observed spectra.

Detector resolution and efficiency

Geant4 can simulate the energy loss of particles before they reach the detector volume and scattering into or between detector volumes but it does not reproduce the intrinsic energy resolution of the detector. The energy recorded is always exactly the same as the energy deposited by the interacting particle. To give more realistic spectra the resolution for the detectors was measured experimentally at different energies and a linear fit of peak full-width half-maximum (FWHM) against energy performed. Figure 6.6 shows this.

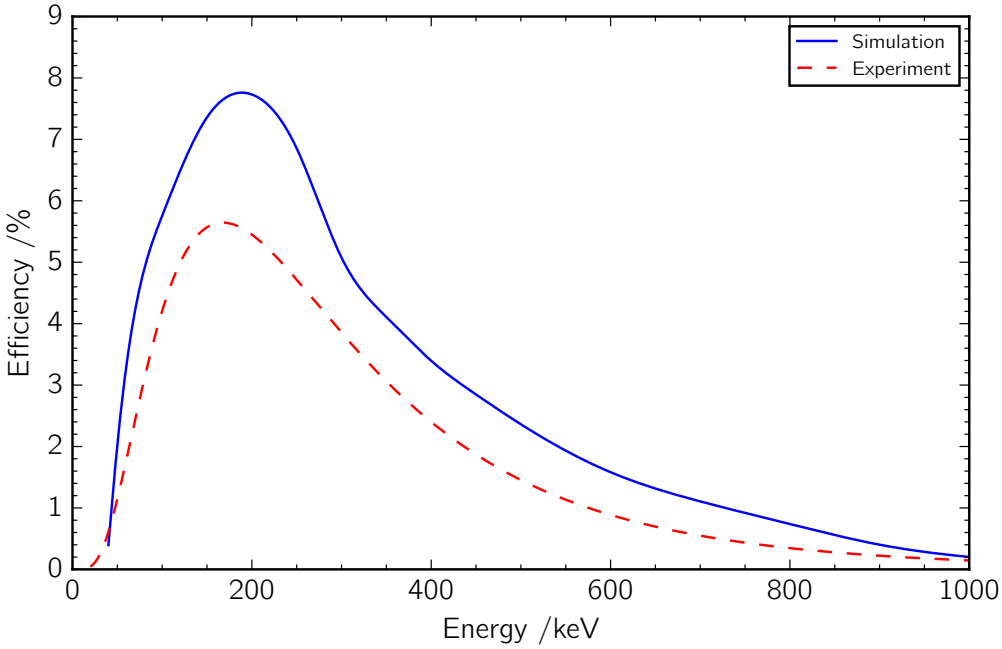

Figure 6.5: Experimental and simulated efficiency curves for the SAGE silicon detector, both with the HV barrier at −38 kV. The experimental data is fitted as described in section 5.6 and the simulated data is fitted with a cubic spline.

The efficiency of the simulated detectors is slightly higher than the measured experimental efficiency, as shown in figure 6.5. This is corrected for by simulating a series of mono-energetic γ-ray and electron sources at the target position and producing efficiency curves from this data for both the germanium and silicon detectors.

Figure 6.7 shows the steps in the processing of raw output from `Geant4`. A Gaussian spread is applied to the energies, with the FWHM increasing with energy, and the simulated spectra are then scaled by the ratio of the experimental efficiency curve to the simulated curve. The simulated efficiency can only be measured above the HV barrier voltage so the spectrum is cut off below this. Add-back in the clover germanium detectors and escape suppression for γ rays scattered into the BGO shields are also performed for the simulated data in the same way as for the experimental data.

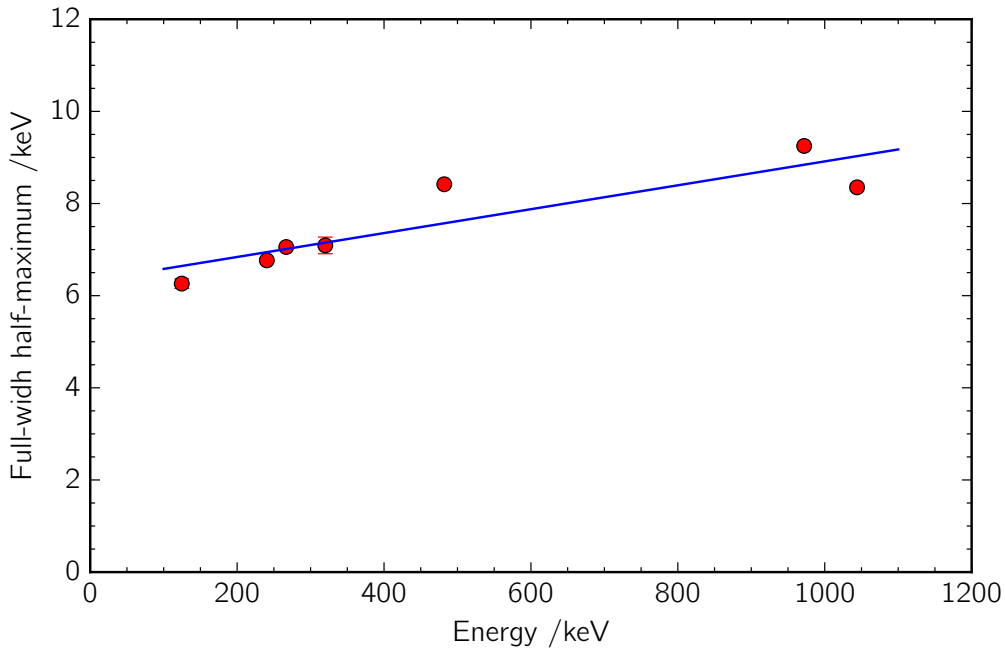

Figure 6.6: Measured full-width half-maximum for the SAGE silicon detector, with a linear fit to the data points. The measured points are from ^{133}Ba and ^{207}Bi sources.

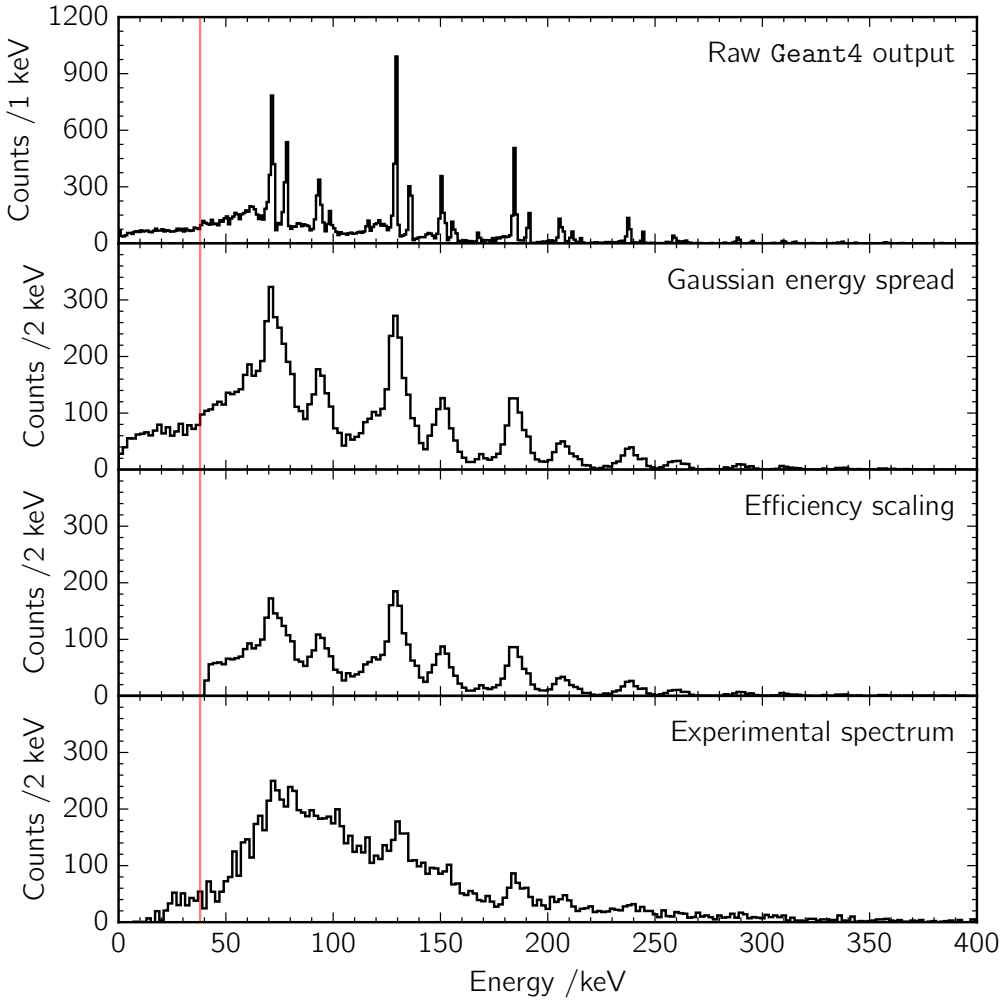

Figure 6.7: Processing of output from `Geant4` simulations to match experimentally measured resolution and efficiency. This example shows spectra from the silicon detector for a simulation of the ^{254}No ground-state band with 98700 simulated events, to match the number of experimental recoil-tagged events. The red vertical line in all the spectra marks the energy cut-off with the maximum HV barrier voltage used in the experiment (-38 kV). A similar process is also used for the germanium detectors.

Chapter 7

Branching ratios and E2/M1 transition intensities

In a rotational band the branching ratios for $\Delta I = 1$ inter-band transitions and $\Delta I = 2$ intra-band transitions depend on the reduced transition probabilities, B(M1) and B(E2) (equations 3.26 and 3.28). The reduced transition probability B(M1) is proportional to the square of the difference between the single-particle g factor, g_K, and the rotational g factor, g_R (both discussed in section 2.5),

$$B(\mathrm{M1}) \propto (g_K - g_R)^2 \tag{7.1}$$

This means that the branching ratios are affected by the single-particle structure of the band. Figure 7.1 shows the transition intensities for the same rotational band with some different values of g_K. This shows how the relative intensities of E2 and M1 transitions varies with $g_K - g_R$, but depends only on its magnitude and not its sign. The E2 transition intensity is higher if $|g_K - g_R|$ is closer to zero and the M1 transitions dominate if $|g_K - g_R|$ is bigger.

The rotational g factor, g_R, can be calculated (equation 2.19) so if the relative intensities of M1 and E2 transitions can be measured the single-particle g factor, g_K, can be determined. The value of g_K depends on the orbitals occupied by the unpaired protons and neutrons making up a state so the ratio of intensities for M1 and E2 transitions in a rotational band gives information about the band's underlying

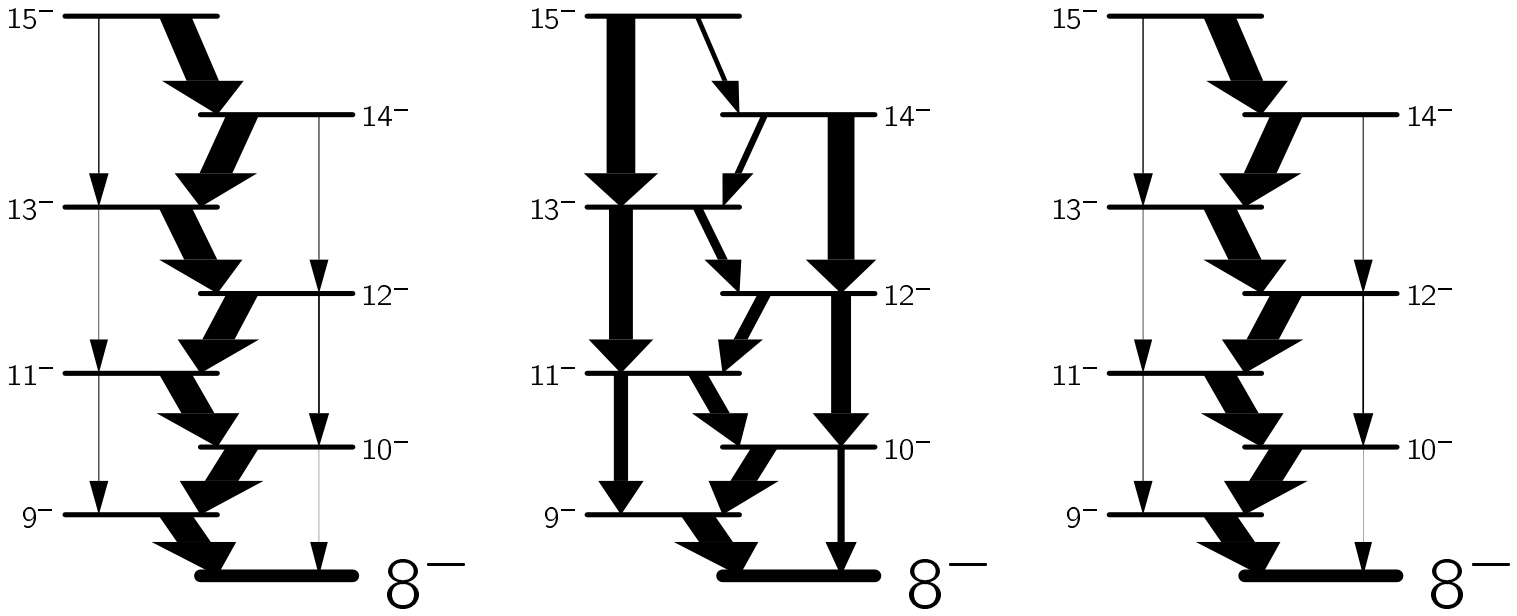

(a) $g_K - g_R = -0.9$ **(b)** $g_K - g_R = 0$ **(c)** $g_K - g_R = +0.9$

Figure 7.1: Identical level schemes with different values of g_K giving different E2/M1 branching ratios. The thickness of the transitions represents their total intensity (γ rays and conversion electrons). Note that the branching ratio depends only on the magnitude of the difference between g_K and g_R, not its sign, so the intensities in (a) and (c) are the same.

single-particle structure.

With enough data the intensities (I) of all transitions can be found by fitting their peaks in a γ-ray spectrum, such as the simulated examples in figure 7.2a, and the branching ratio I_{E2}/I_{M1} found for the transitions depopulating each level in the band. These branching ratios can then be compared to theoretical values calculated with the g_K values of different possible single-particle structures for the band.

7.1 E2/M1 electron intensity ratios

When only a more limited amount of data is available, for example the simulated spectra in figure 7.2b, it is not possible to measure individual M1 and E2 transition intensities. An alternative approach based on the summed intensity of all γ rays from the band has been developed [110], but the dominance of internal conversion over γ decay in the heaviest nuclei means that adapting this method to use electron intensity ratios from SAGE is more useful.

The silicon detector spectrum can be split into two regions, one containing electrons from M1 inter-band transitions and the other containing electrons from E2 intra-band transitions. For M1 transitions the largest component of the conversion coefficient is for the K shell so conversion electrons are mostly in the lower-energy part of the spectrum. For E2 transitions the L-shell component of the conversion coefficient is larger and the electrons have higher energies. Splitting the spectrum into these two areas depends only on the general shape of the electron distribution and not on being able to identify discrete peaks. The numbers of electrons in each of these regions, I_{M1} and I_{E2}, are measured and the ratio between them is calculated,

$$R = \frac{I_{E2}}{I_{M1}} \tag{7.2}$$

As well as calculating R from the experimental spectrum it is also found from `Geant4` simulations for the same level scheme with different g_K values (which give different branching ratios) and the experimental value can then be compared to the simulated

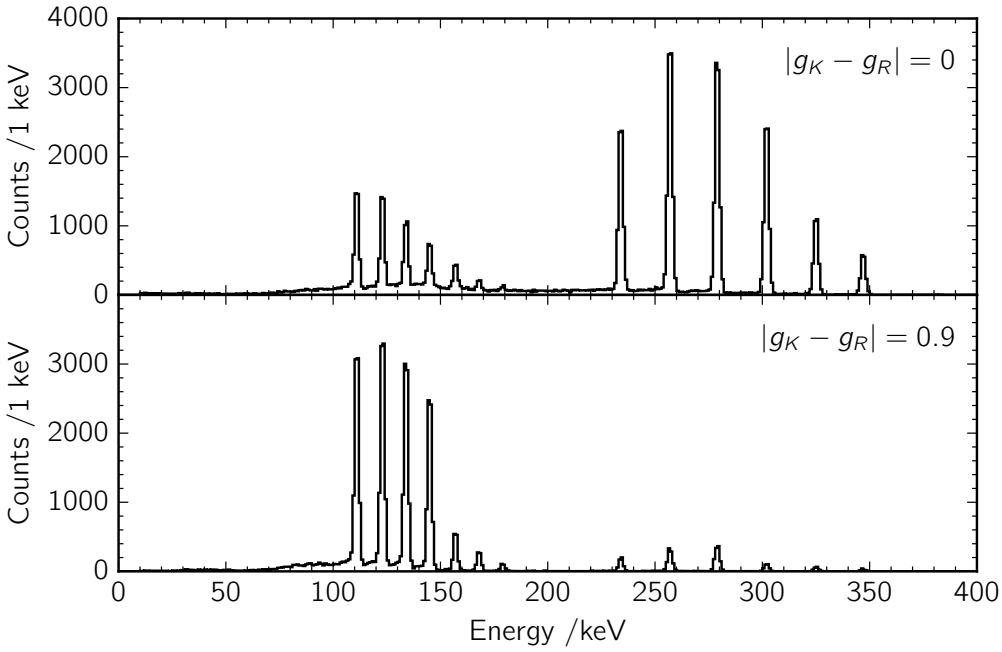

(a) With 10^6 simulated events the γ-ray clear peaks can be seen from all inter-band and intra-band transitions and could be fitted to find the transition intensities.

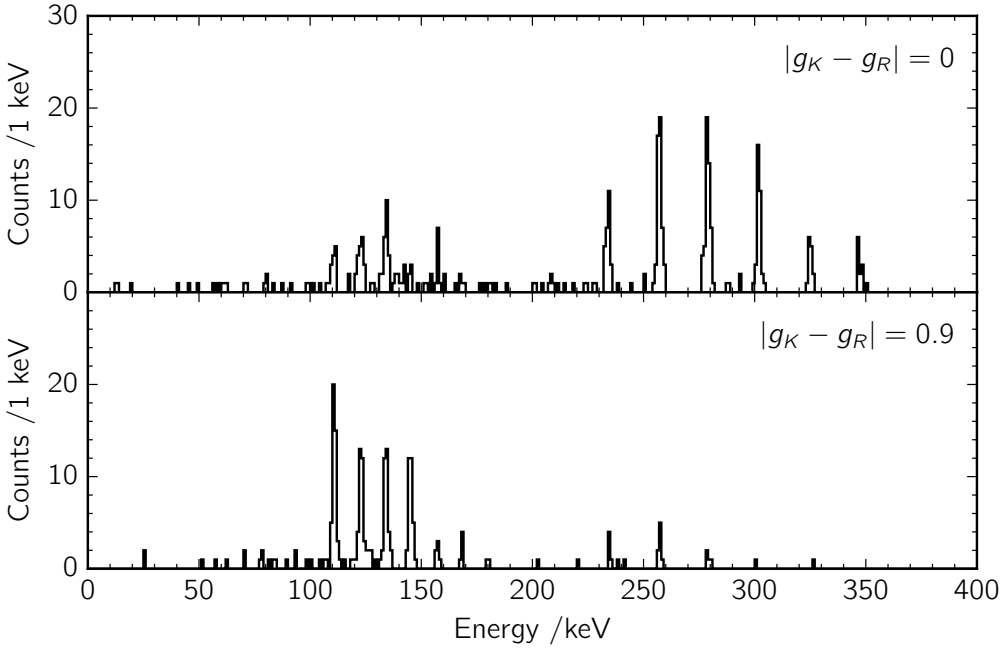

(b) With only 5000 simulated events the γ-ray peaks from either the M1 or E2 transitions become less distinct and it is no longer possible to fit the areas of all of them.

Figure 7.2: Simulated spectra from the SAGE germanium detectors for two extreme values of $|g_K - g_R|$ with different numbers of events.

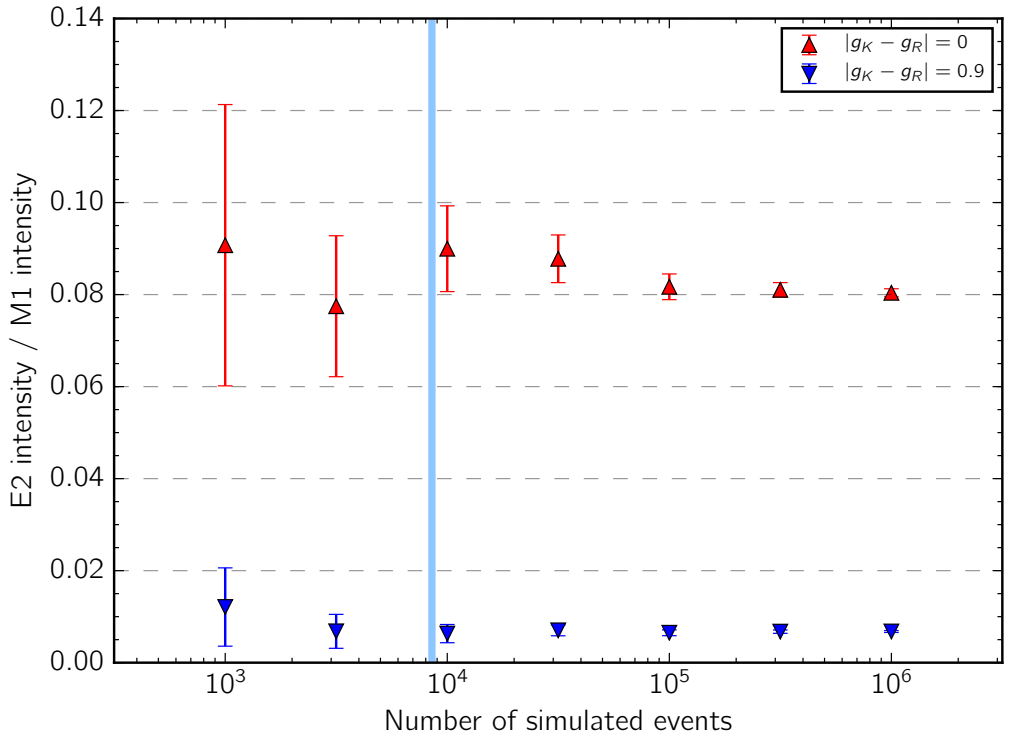

Figure 7.3: Ratio of E2 and M1 electron intensities from simulated SAGE silicon detector spectra with different numbers of events, for two extreme values of $|g_K - g_R|$. The vertical blue line shows the number of recoil-isomer tagged events in the experimental data.

values to find g_K for the band.

Figure 7.3 shows the value of the ratio R from simulations with different values of $|g_K - g_R|$ for different numbers of events. As the number of events decreases the uncertainty on the ratio increases but the ratio itself does not change significantly. This makes it possible to investigate g_K for a band with a much smaller amount of data than would be needed to use γ-ray intensities from fitting individual peaks.

In order for the method to work it must be possible to separate the electron spectrum into regions of M1 and E2 electrons, the limits for each of these regions must be chosen and a background contribution to the experimental spectrum in each region must be estimated. Each of these points is discussed in more detail in the following sections.

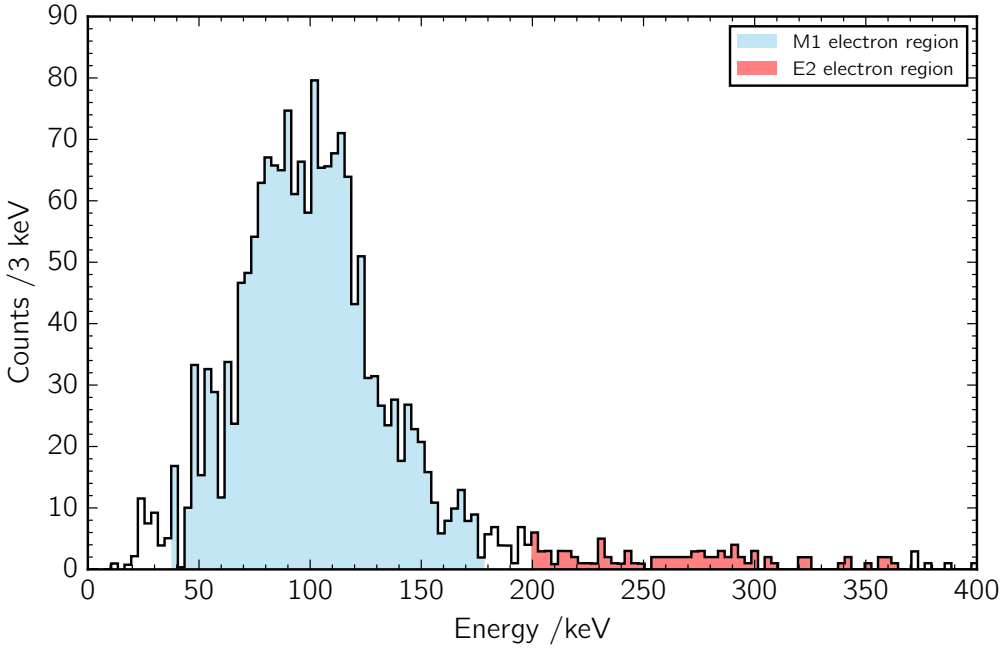

Figure 7.4: Regions of conversion electrons from M1 and E2 transitions shown on the experimental recoil slow-isomer tagged SAGE spectrum.

7.2 M1 and E2 electron region limits

The division of the SAGE silicon detector spectrum into two separate regions, one of electrons from M1 transitions and the other of electrons from E2 transitions, is shown on a recoil-isomer tagged electron spectrum in figure 7.4 and this section explains how the edges of each region have been chosen.

For the ratio of the M1 and E2 electron region areas to give useful information it is also important that it is not strongly sensitive to the exact choice of the edges of each region. This has been investigated with the recoil-isomer tagged SAGE data by varying each of the edges while holding the other three constant. Figures 7.5–7.8 show the effect of this on the intensity ratio.

The lower limit of the M1 electron region is at 40 keV, just above the SAGE barrier voltage. Electrons from the target position with energies less than this shouldn't reach the silicon detector so they are excluded from the M1 electron region. The efficiency correction between the simulated and experimental spectra (section 6.4) is

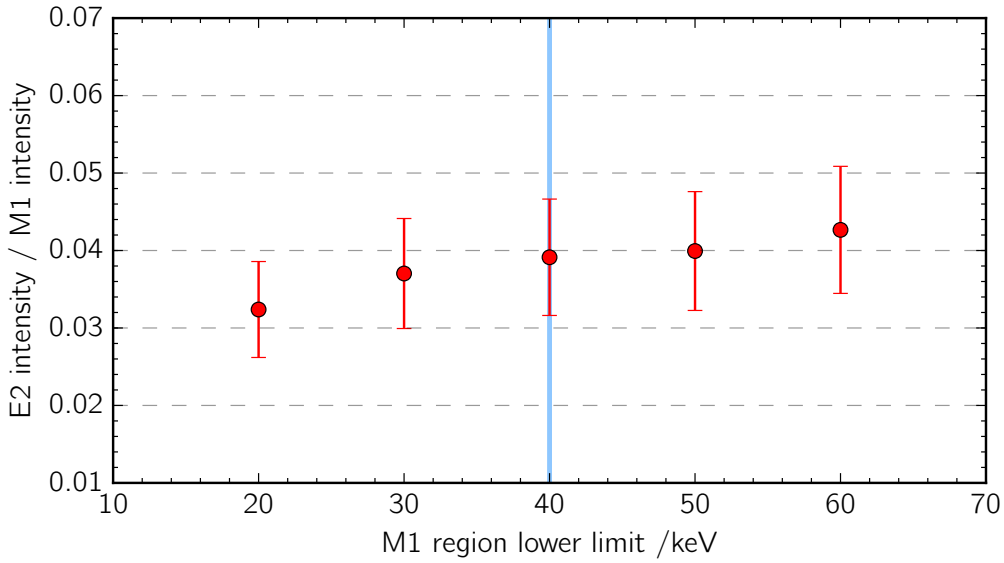

Figure 7.5: Change in E2/M1 electron intensity ratio as lower limit of M1 electron region is varied for the experimental spectrum. The vertical line marks the chosen limit of 40 keV.

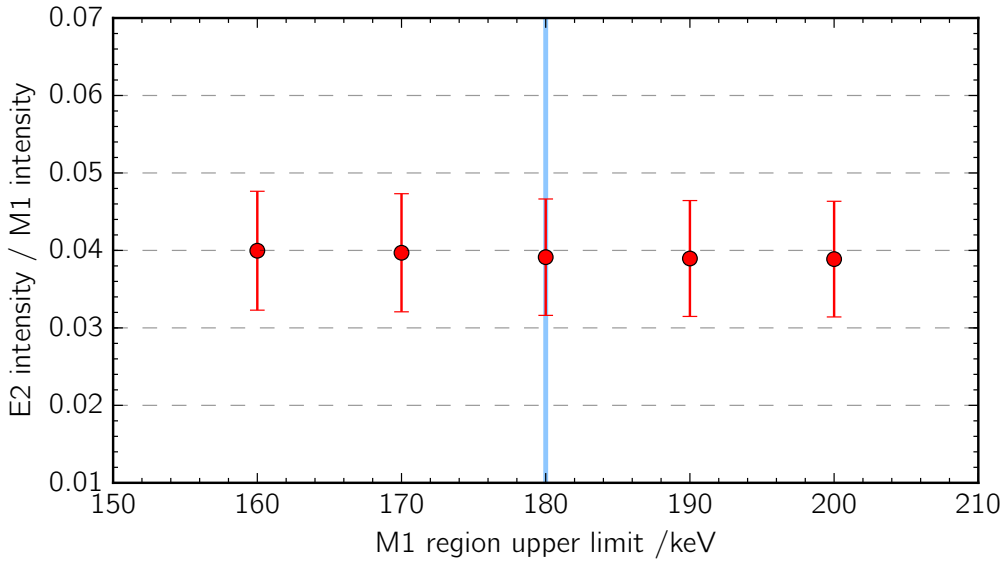

Figure 7.6: Change in E2/M1 electron intensity ratio as upper limit of M1 electron region is varied for the experimental spectrum. The vertical line marks the chosen limit of 180 keV.

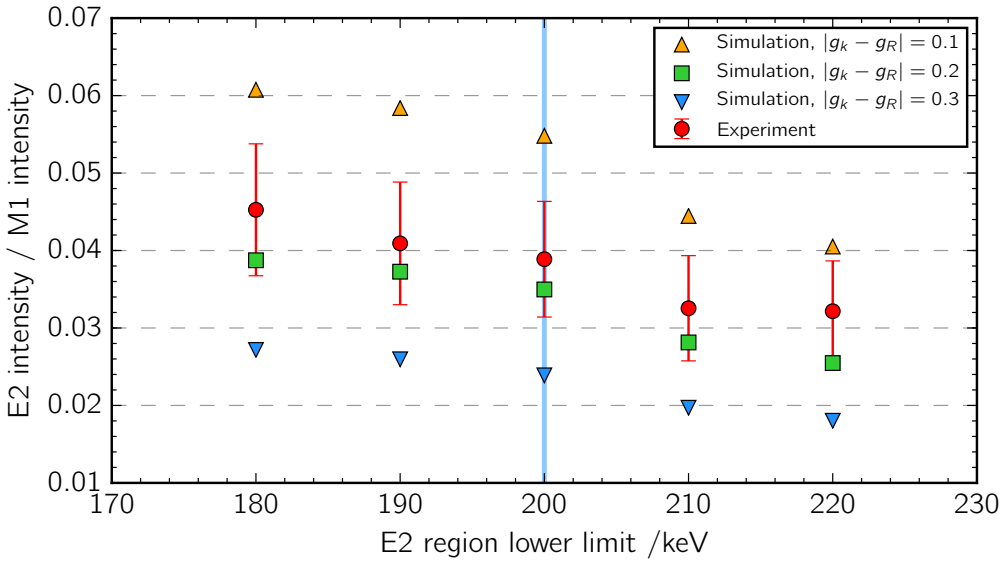

Figure 7.7: Change in E2/M1 electron intensity ratio as lower limit of E2 electron region is varied for the experimental spectrum and `Geant4` simulations with three different values of $|g_K - g_R|$. The vertical line marks the chosen limit of 200 keV.

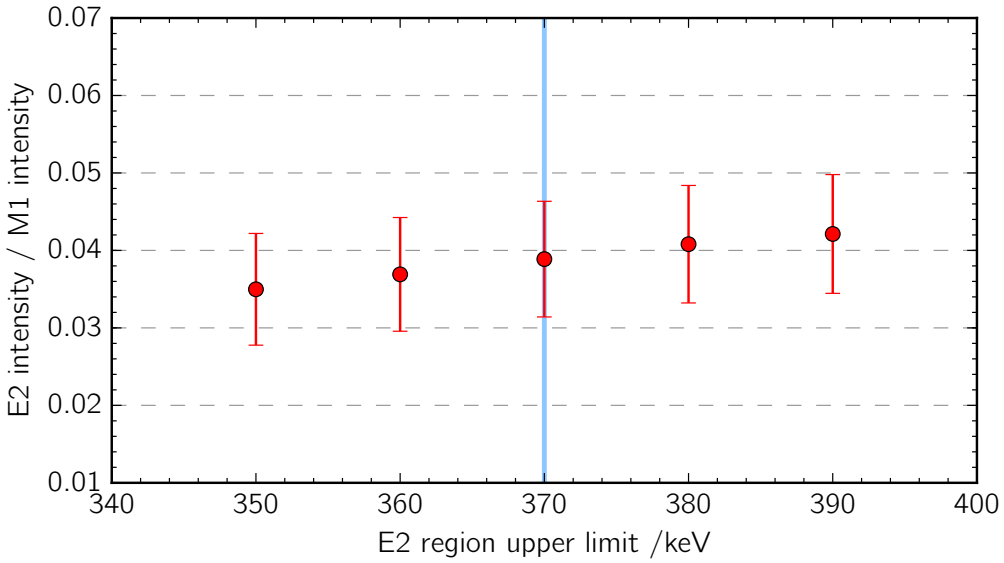

Figure 7.8: Change in E2/M1 electron intensity ratio as lower limit of E2 electron region is varied for the experimental spectrum. The vertical line marks the chosen limit of 370 keV.

also not possible below the barrier voltage.

The upper limit for of the M1 electron region is 180 keV. This is determined from the K-shell electron binding energy of the atom (149 keV for nobelium). For M1 transitions with energy lower than the K-shell binding energy it is not possible to emit K-shell conversion electrons so the L-shell component of the conversion coefficient is largest and the most energy electrons are at around $E_\gamma - E_L$. For M1 transitions with energy greater than the K-shell binding energy the K-shell component of the conversion coefficient dominates and most electrons have an energy $E_\gamma - E_K$, with only a much smaller number at $E_\gamma - E_L$. This means most electrons from M1 transitions will have energies less than the K-shell binding energy. The limit is set slightly above this to take into account the resolution of the silicon detector. Figure 7.6 shows that the ratio, R, does not vary much even when the upper edge of this region is moved by $\pm$20 keV.

The E2 transitions have higher energies than the M1 transitions and are all above the K-shell binding energy, but the L-shell component of the conversion coefficient is bigger than the K-shell component so most of the emitted conversion electrons are from the L shell, with energy $E_\gamma - E_L$ ($E_\gamma - 29$ keV in nobelium). The lower limit of the E2 electron region is set from the lowest energy E2 transition in the band minus the L-shell binding energy. The lowest energy E2 transition in the band above the isomer in ^{254}No is 234 keV so the lower limit of the E2 electron region is at 200 keV to include all E2 L-shell electrons. There is a gap left between the upper edge of the M1 electron region and the lower edge of the E2 region so that moving the edge of one does not affect the other. In figure 7.7 the value of R is affected more strongly by moving this edge of this region. The ratio has also been plotted from simulated spectra with a range of g_K values with the lower edge of the E2 region varied in the same way as for the experimental data. The values of R from simulations with any value of g_K vary with the E2 region lower limit in the same way as the experimental R so the value of g_K found by comparing experiment and simulation will be the same even if the edge of the region is moved.

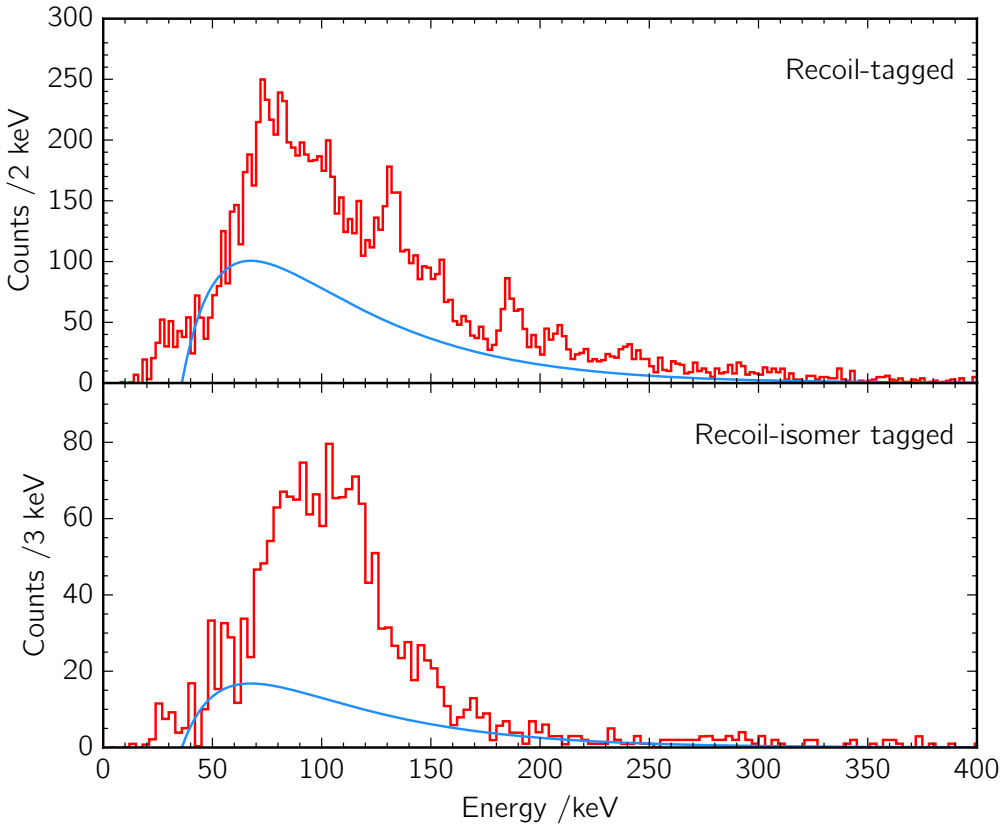

Figure 7.9: Recoil-tagged and recoil-isomer tagged SAGE silicon detector spectra with modelled background curves.

The upper limit of the E2 region is at 370 keV, just above the highest E2 transition, but its exact position makes only a small difference to the E2/M1 intensity ratio because the conversion coefficient and detector efficiency both decrease with energy and the number of observed electrons around this energy is very small.

7.3 Background

The difference between the background in the simulated and experimental SAGE spectra must also be considered when the E2/M1 intensity ratios are compared. The simulated level scheme includes only the rotational band being investigated, but even after subtraction of time-random background (section 6.2) there will still be

background in the experimental spectrum from any other bands in ^{254}No feeding into the simulated band.

The background intensity, I_{bgr}, in the electron spectrum is modelled with the same function of energy as was used for the SACRED spectrometer [59],

$$I_{\text{bgr}}(E) = a\left(1 - \sqrt{\frac{b}{E}}\right)\mathrm{e}^{cE} \tag{7.3}$$

The parameter b is the HV barrier voltage [111], and is set at $b = 36$ from the average of the three different barrier voltages used, weighted by the number of events at each voltage. The parameters $a = 1440$ and $c = -0.02$ are set so the shape of the background distribution matches the recoil-tagged spectrum in the upper panel of figure 7.9. This is then scaled to give an estimated maximum background for the recoil-isomer tagged spectrum by setting $a = 240$ without changing b or c, as shown in the lower panel of figure 7.9. Integrating the function numerically gives the total background contribution to each of the M1 and E2 electron regions,

$$B_{\text{M1}} = \int_{\text{M1}} I_{\text{bgr}}(E)\,\mathrm{d}E \tag{7.4}$$

$$B_{\text{E2}} = \int_{\text{E2}} I_{\text{bgr}}(E)\,\mathrm{d}E \tag{7.5}$$

To take into account any uncertainty in estimating the background the ratio R is found with a maximum and minimum (zero) background. With no background the value is just

$$R = \frac{I_{\text{E2}}}{I_{\text{M1}}} \tag{7.6}$$

To find the value with an estimated background the background in each region is subtracted from that region's area before the ratio is calculated

$$R_{\text{bgr}} = \frac{I_{\text{E2}} - B_{\text{E2}}}{I_{\text{M1}} - B_{\text{M1}}} \tag{7.7}$$

The experimental value of R is found from the average of these two values (which would match an average estimated background) but the uncertainty on the value includes the values within the uncertainties on each individual value (which is bigger than if an average estimated background was used).

The much smaller total number of electrons in the E2 region means the contribution of the background in it has a much greater effect on the ratio than the background in the M1 region, but from equation 7.7 it can be seen that if the background in both regions is increased each will have an opposite effect on the E2/M1 ratio. The shape of the background distribution means that increasing the background in the E2 region also increases the background in the M1 region and the effect on the intensity ratio is smaller than it would be if the background in each region was varied independently.

7.4 Initial population of levels

In prompt spectroscopy the intensity of transitions depends on the initial population of the levels above them from the fusion-evaporation reaction, as well as the intensities of the transitions feeding those levels. Entry distributions have been measured for the ^{208}Pb(^{48}Ca,2n)^{254}No reaction at beam energies of 215 MeV and 219 MeV [112] and at 219 MeV and 223 MeV [113, 114].

Simulations using level populations based on any of these entry distributions show no significant difference so the 219 MeV measurement by Henning et al. [114], shown in figure 7.10, is used and assumed to be valid for the 220 MeV beam energy in this work.

7.5 Simulations

Simulations are run for the same level scheme with a range of $g_K - g_R$ values from -0.9 to $+0.9$ in steps of 0.05. For each step events are simulated with the SAGE high-voltage barrier at 28 kV, 32 kV and 38 kV for a total of 100000 events, split

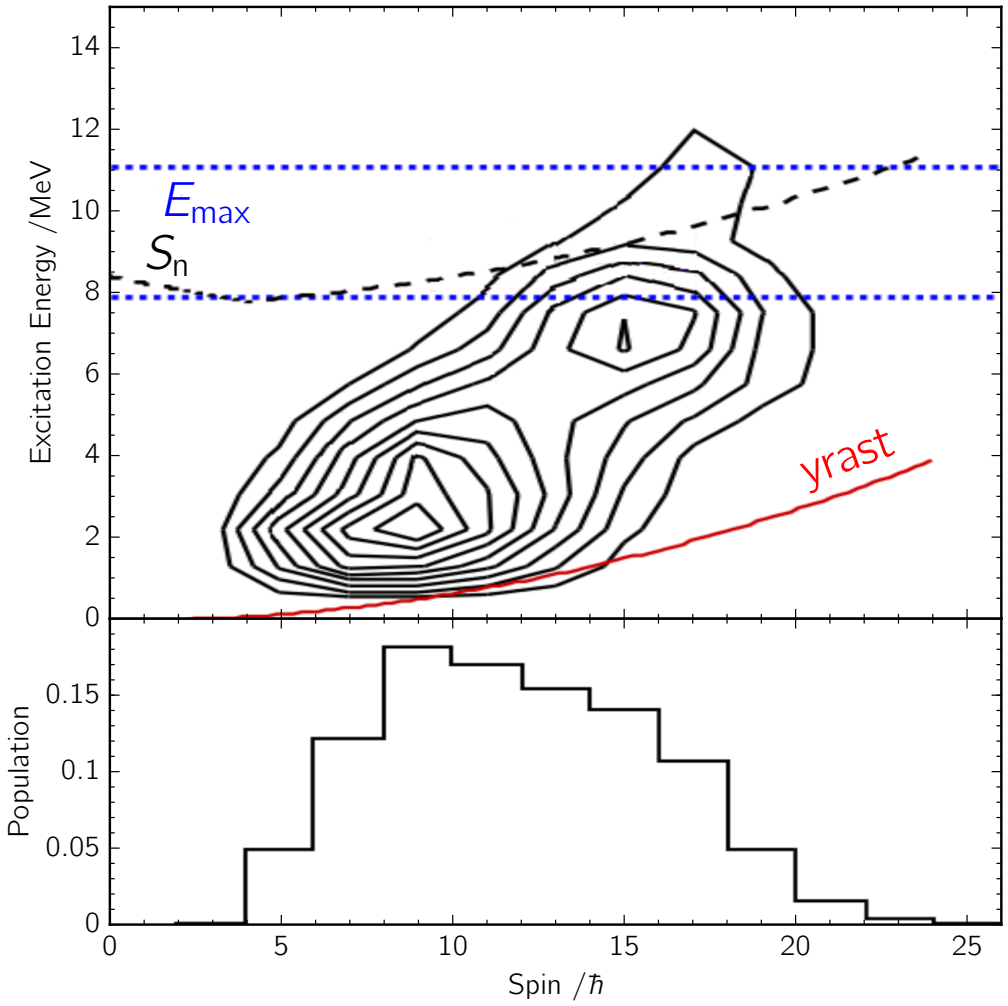

Figure 7.10: Entry distribution and its spin projection for the ^{208}Pb(^{48}Ca,2n)^{254}No reaction with a 219 MeV beam energy. In the upper panel the solid red line shows the ^{254}No yrast line, the dashed black line shows the neutron separation energy, S_n, and the dotted blue lines are the maximum excitation energy at the front and back of the target, E_{max}. Modified from figure 1 of Henning et al. (2014) [114].

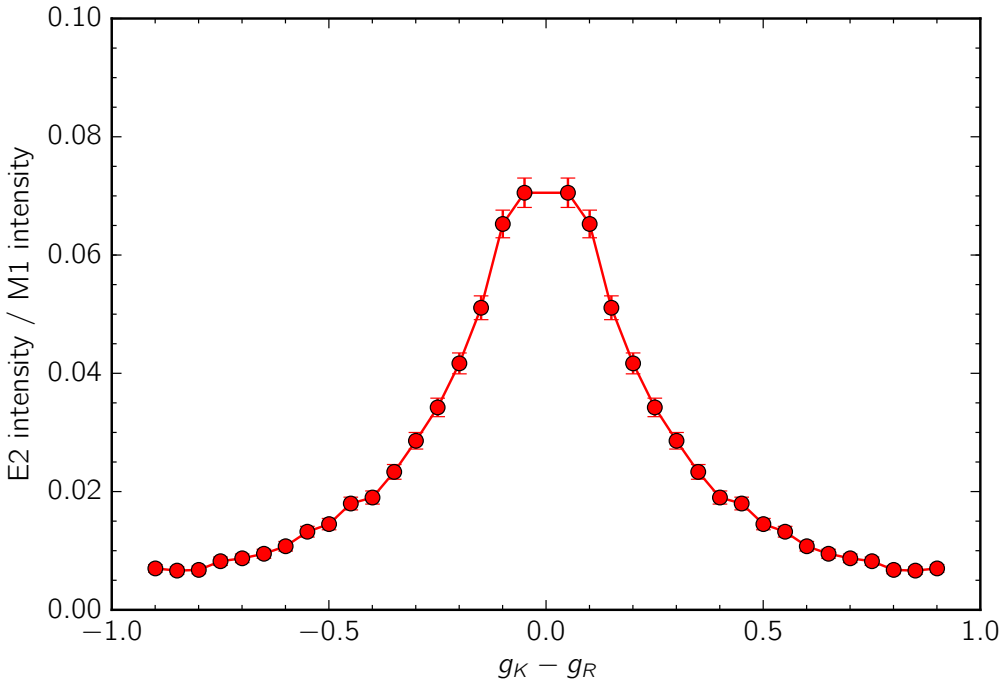

Figure 7.11: Ratio, R, of E2 and M1 electron intensities from `Geant4` simulations. The curve is symmetric because R depends only on the modulus of $g_K - g_R$.

between the barrier voltages in proportion to the number of experimental isomer-tagged events at each voltage. After applying corrections to the raw `Geant4` output for detector efficiency and resolution (section 6.4) the ratio R of the number of counts in the E2 and M1 electron regions is found. This is plotted against $g_K - g_R$ in figure 7.11.

The value of R from an experimental spectrum can be drawn as a horizontal line on figure 7.11 and from the points at which it crosses the simulated curve two possible values of $g_K - g_R$ will be found.

7.6 Summary

In this chapter a method has been developed to investigate the single-particle structure of an isomeric state by determining a value for $g_K - g_R$ from the conversion electron spectrum of the band built on the isomer. The electron spectrum is split

into separate regions of electrons from M1 and E2 transitions. The edges of each of these regions have been justified and it has also been shown that the deduced $g_K - g_R$ should not be sensitive to small changes in the location of these edges. The function used to model the background in the experimental spectrum has also been discussed.

Chapter 8

Ground-state band

Both γ rays and conversion electrons from the ground-state band of ^{254}No have been observed separately in previous experiments, but using SAGE is the first time that they have been measured at the same time. This allows coincidences between them to be seen and by measuring the intensities of γ rays and conversion electrons from the same transitions experimental values for the conversion coefficients can be calculated.

8.1 Conversion coefficients

Figure 8.1 shows recoil-tagged γ-ray and electron singles spectra. The electron spectrum has had background subtracted using the method described in section 6.2. Where possible the peaks have been fitted to find their energies and intensities and table 8.1 gives details of these.

For the transitions where it is possible for the peak areas to be measured in both the γ-ray and conversion-electron spectra the conversion coefficients can be calculated using equation 3.19 and these are also listed in table 8.2b. The L- and M-shell components of the conversion coefficients are plotted separately in figure 8.2a with theoretical conversion coefficients for E1, M1, E2 and M2 multipolarity transitions, calculated using `BrIcc`, also shown for comparison.

For some transitions the energy resolution of SAGE is good enough to resolve the L-shell peak into two components: one from the L_I and L_{II} sub-shells, and one from

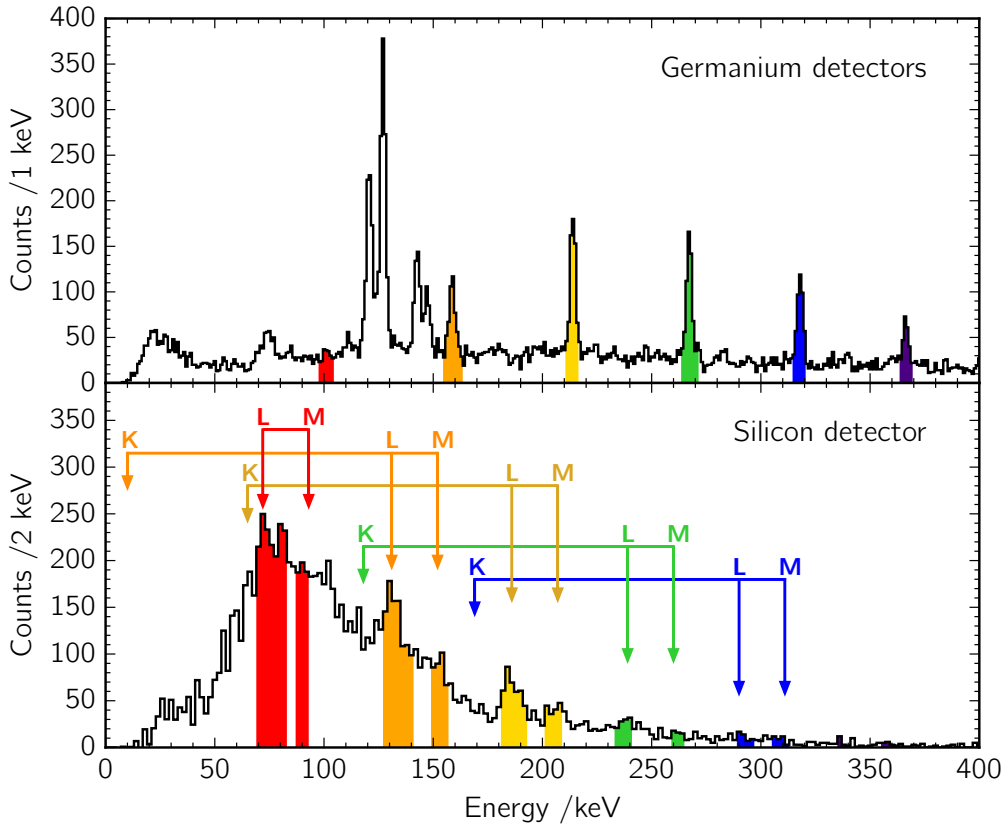

Figure 8.1: Spectra from the SAGE silicon and germanium detectors for recoil-tagged data. γ-ray and conversion-electron peaks from the same transitions in the ground-state band are shaded in the same colour and electron shells are labelled on the silicon detector spectrum.

the L_{III} sub-shell. The ratios of the conversion coefficients for these sub-shells,

$$\frac{\alpha_{L_I} + \alpha_{L_{II}}}{\alpha_{L_{III}}} \tag{8.1}$$

are plotted in figure 8.2b, with theoretical values from `BrIcc` also shown.

8.2 Coincidences

Coincidences between γ rays and conversion electrons from different transitions show that they are both part of the same cascade in a nuclear decay and helps to

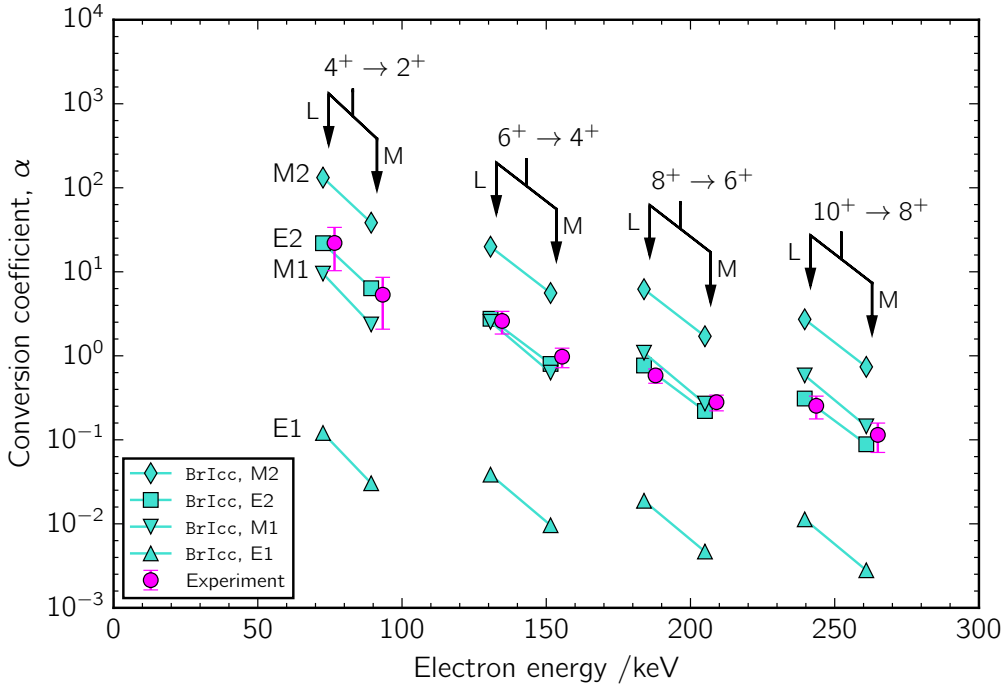

(a) L- and M-shell conversion coefficients.

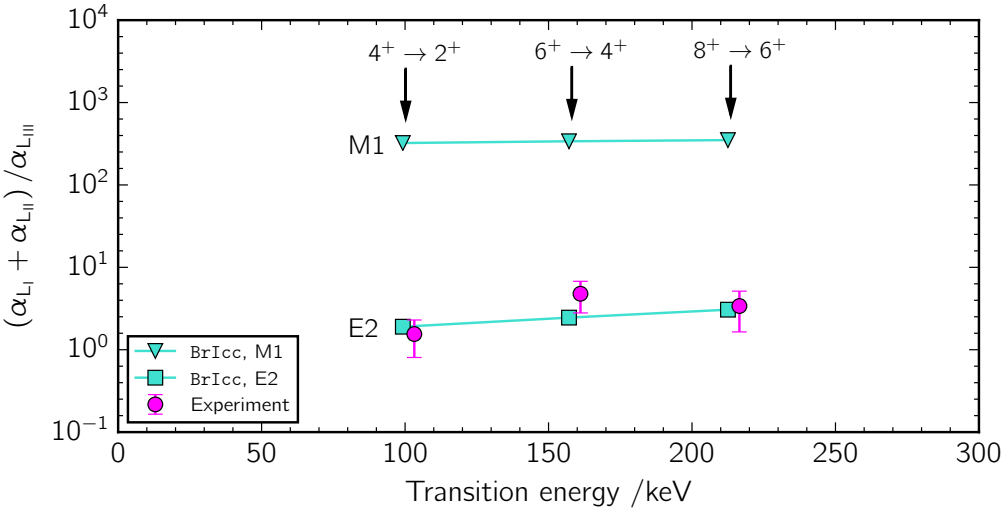

(b) Ratio of conversion coefficients for L electron sub-shells.

Figure 8.2: Conversion coefficients for ground-state band transitions. A log scale is used to compare conversion coefficients for different transition multipolarities over a wide range of energies. Theoretical values from `BrIcc` for different transition multipolarities are plotted for comparison with experimental data. The energies of experimental and theoretical data points are offset slightly so both can be seen.

Table 8.1: Ground-state band transition energies, E, and intensities, I, measured with SAGE. Subscripts refer to γ rays, L-shell electrons and M-shell electrons.

(a) Measured energies for γ rays and L- and M-shell conversion electrons.

Transition	E_γ /keV	E_L /keV	E_M /keV
$4^+ \rightarrow 2^+$	101.2(6)	75(1)	91(2)
$6^+ \rightarrow 4^+$	159.1(2)	133(1)	154(3)
$8^+ \rightarrow 6^+$	214.5(2)	186(2)	207(3)
$10^+ \rightarrow 8^+$	267.8(1)	242(3)	263(5)

(b) Measured intensities, corrected for detector efficiency, for γ rays and L- and M-shell conversion electrons. Total conversion coefficients, α, from the experimental peak areas and from `BrIcc` are also listed.

Transition	I_γ	I_L	I_M	α_{exp}	α_{BrIcc}
$4^+ \rightarrow 2^+$	5.6(27)	120(30)	30(11)	27(14)	30(1)
$6^+ \rightarrow 4^+$	31(4)	82(23)	31(7)	3.6(9)	3.99(6)
$8^+ \rightarrow 6^+$	60(5)	35(6)	17(3)	0.9(1)	1.20(2)
$10^+ \rightarrow 8^+$	54(5)	14(4)	6(2)	0.37(9)	0.532(8)

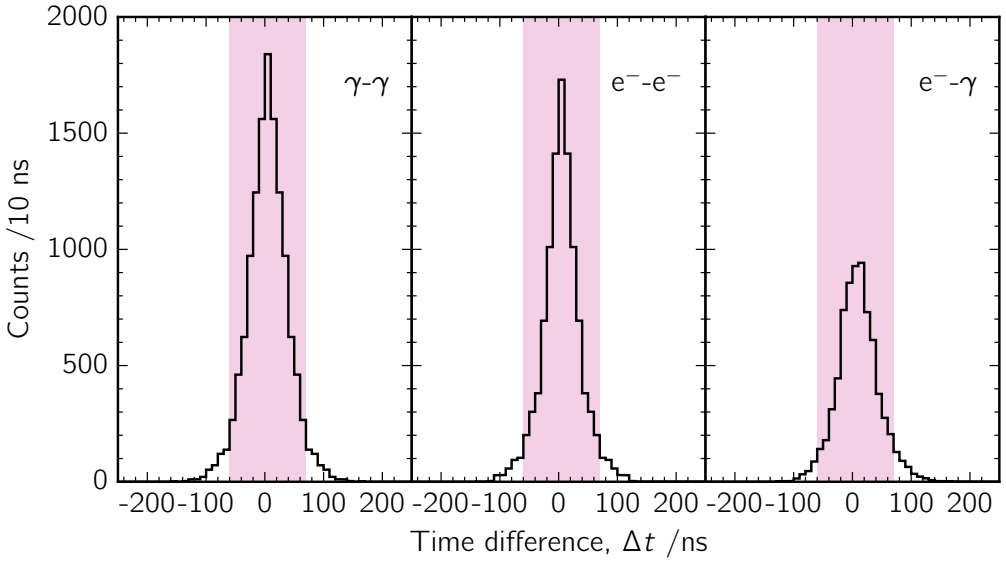

Figure 8.3: Time differences between hits in the SAGE silicon and germanium detectors with shaded areas showing the gates used to select coincidences.

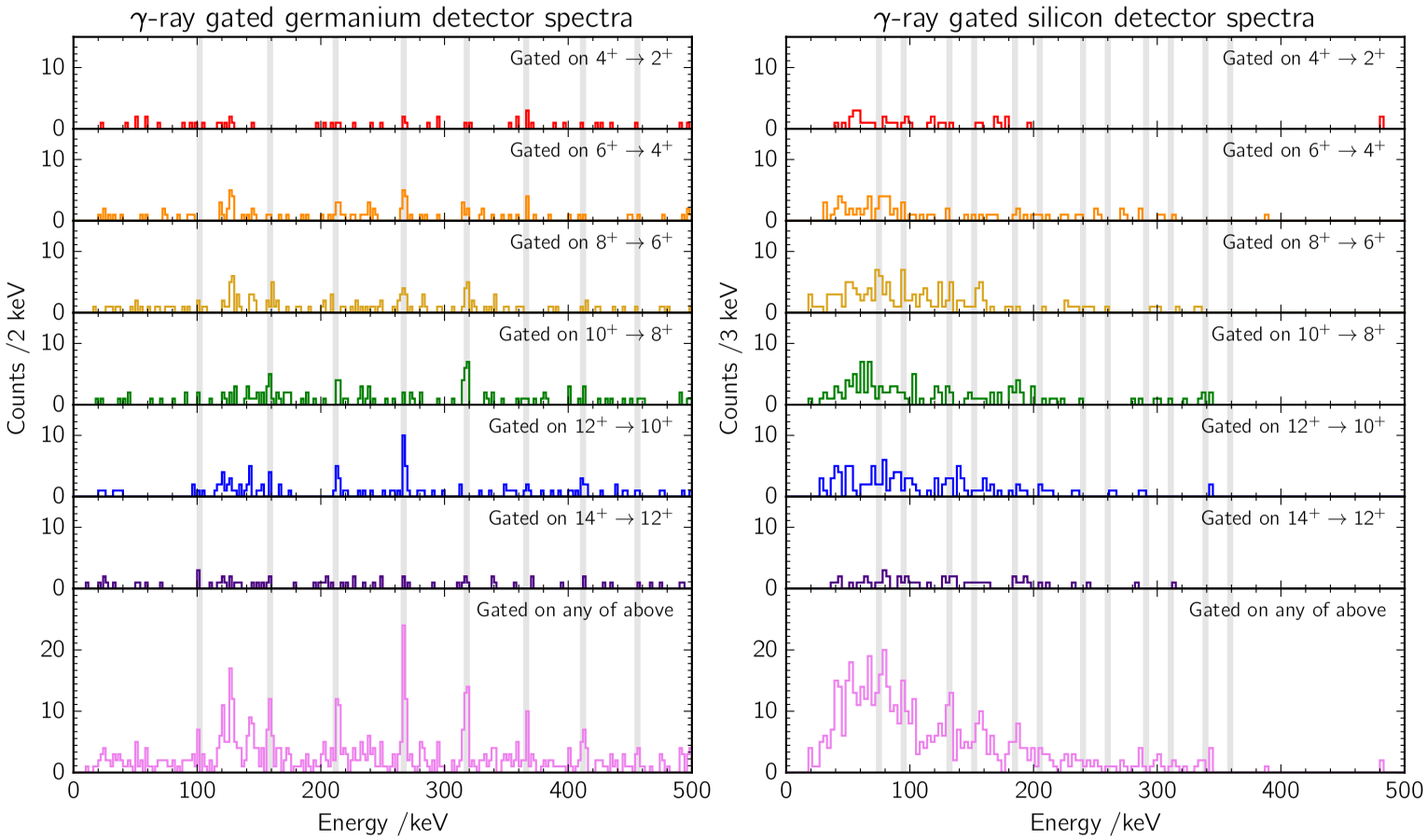

Figure 8.4: Recoil-tagged SAGE spectra gated on coincidences with γ rays from ground-state band transitions. Energies of γ rays, or L- and M-shell conversion electrons from transitions in the ground-state band are marked.

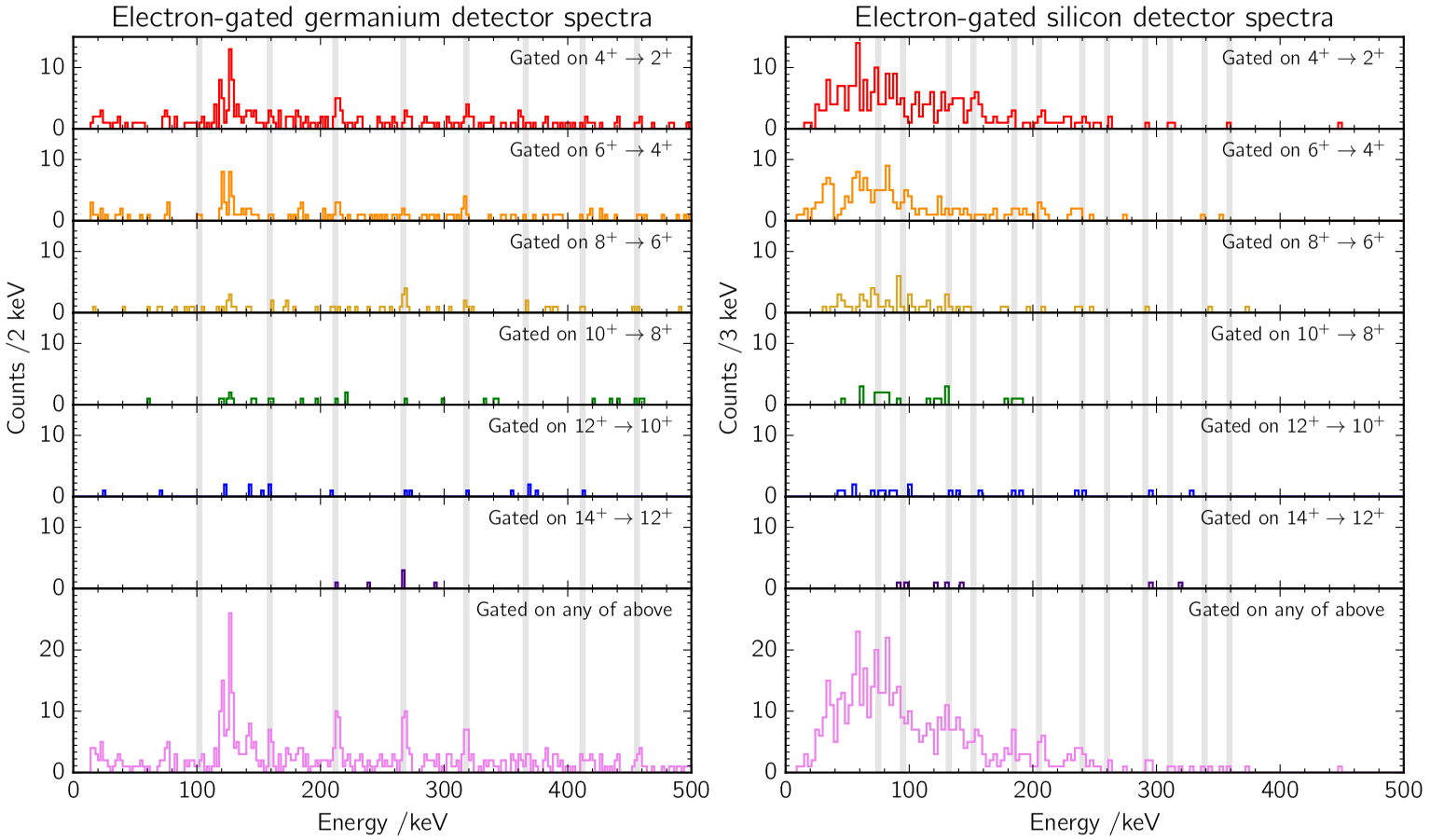

Figure 8.5: Recoil-tagged SAGE spectra gated on coincidences with L-shell conversion electrons from ground-state band transitions. Energies of γ rays, or L- and M-shell conversion electrons from transitions in the ground-state band are marked.

place the transitions in a level scheme. When the data is sorted each event is 4 μs long so as well as these true coincidences there will also be random coincidences between unrelated signals in different SAGE detector elements (germanium detector crystals or silicon detector pixels). Within each event the true coincidences are identified with a much tighter gate on the time difference, Δt, between the signals,

$$-60 \text{ ns} \leq \Delta t \leq 70 \text{ ns}$$

The distribution of time differences between hits in the germanium and silicon detectors are shown in figure 8.3.

Spectra can be produced of γ rays or electrons in coincidence with any chosen transition by gating on the energy of one hit in each coincident pair. The first hit in the pair is only added to the spectrum if the second hit passes an energy gate used to identify the chosen transition. It is also possible to identify transitions in coincidence with any one of a number of chosen transitions by comparing the second hit with a set of energy gates. In this case a hit is only added to the resulting spectrum once, even if it is in multiple-coincidence with more than one other hit passing more than one of the set of energy gates [115].

Using SAGE transitions can be identified by gating on either γ rays or conversion electrons of the correct energy. Spectra in coincidence with γ rays from the ground-state band are shown in figure 8.4. The gates used to identify the ground-state band transitions have a width of 4 keV centred on the transition energy, E_γ. Figure 8.5 shows hits in coincidence with L-shell electrons from the ground-state band. The energy gates have a width of 6 keV centred on the L_I electron energy, $E_\gamma - 29$ keV. In both cases spectra are also shown of hits in coincidence with any of the gates used.

8.3 Discussion

The ground-state band has been observed previously and the SAGE data does not extend the level scheme. The singles spectra (figure 8.1) show how as the transition energy decreases and the conversion coefficient increases the electron peaks become relatively more important than the γ-ray peaks. The lowest-energy transition in the band ($E_\gamma = 44(1)$ keV, $2^+ \rightarrow 0^+$) is not seen in either spectrum. Its low energy means it has a very large conversion coefficient of $\alpha = 1550(200)$ and γ ray emission is unlikely, but L-shell electrons from it have energies of 15–22 keV and are stopped from reaching the silicon detector by the high-voltage barrier.

Conversion coefficients

Comparing the measured conversion coefficients from the ground-state band transitions with values from `BrIcc` (figure 8.2a) shows that they are not consistent with either E1 or M2 multipolarity. E2 multipolarity looks most likely, but M1 is also possible.

The relative size of the conversion coefficients for different electron shells also varies with transition multipolarity, and comparing the experimental ratios of L_I + L_{II} to L_{III} conversion coefficients to theoretical values for M1 and E2 multipolarity (figure 8.2b) rules out M1 multipolarity and leaves E2 as the only possible multipolarity of the ground-state band transitions. This is as expected for a rotational band.

Although the uncertainties on the calculated conversion coefficients are large the theoretical conversion coefficients for different multipolarity transitions vary by several orders of magnitude and the multipolarity of the transitions can be determined experimentally. For a rotational band built on the ground state of an even-even nucleus the multipolarity of all transitions could be deduced to be E2 without measuring the conversion coefficients, but the measurement shows that with enough data it is possible to use SAGE to determine transition multipolarities.

Coincidences

Coincidence spectra gated on either γ rays or electrons from the ground-state band show peaks in both the germanium and silicon detector spectra from other transitions in the band. This confirms that both the γ rays and conversion electrons are from transitions in the same band. Coincidences between electrons from more highly-converted low energy transitions and γ rays from higher energy transitions can be seen, for example the 367 keV γ rays in coincidence with the $4^+ \rightarrow 2^+$ electrons in the top-left spectrum of figure 8.5. Gating on γ rays shows the 102 keV γ-ray peak from the $4^+ \rightarrow 2^+$ transition much more clearly than in the singles spectrum but it is still not possible to identify the $2^+ \rightarrow 0^+$ transition.

The spectra in coincidence with conversion electrons show a greater number of nobelium X-rays than those in coincidence with γ rays. These are the X-rays emitted when atomic electrons re-arrange themselves after a conversion electron is emitted. The relative importance of γ rays and conversion electrons for higher- and lower-energy transitions is also seen in the spectra. As the transition energy increases fewer conversion electrons are emitted and the number of coincident hits in figure 8.5 drops quickly as the transition energy is increased. For γ rays more coincidences are seen as transition energy increases, before the number falls again due to lower detector efficiency.

There is no background subtraction performed on the coincidence spectra and for the lower-energy transitions in the silicon detector a lot of background electrons also pass the energy gate. This gives more background from random coincidences in the electron-gated spectra.

Chapter 9

Level scheme between the isomers

The two proposed level schemes above the slow isomer in ^{254}No are both based on decay spectroscopy of the fast isomer, but in this work the structure above the slow isomer can also be investigated using recoil-isomer tagged in-beam spectroscopy. Figure 9.1 shows the two suggested level schemes along with a third simpler level scheme in which the 605 keV transition directly depopulates the fast isomer

The main differences between the level schemes are the placement of the 605 keV transition. In level scheme C it depopulates the fast isomer directly and should not be seen in the prompt data. This level scheme can therefore be ruled out if any γ rays or conversion electrons from the 605 keV transition are seen in SAGE.

In level schemes A and B the 605 keV transition does not directly depopulate the fast isomer and in either case it would be expected to be seen in the prompt data, but the intensity would be different. Each excited state can be populated either by transitions into it from decay of higher-energy excited states in ^{254}No or directly from the fusion-evaporation reaction, but the state is depopulated only by decay through the transitions out of it into lower-energy states. This means the total intensity of transitions out of any state must be at least as much as the total intensity of transitions into the state. Transitions nearer the bottom of the level scheme must have higher intensities than those near the top. If level scheme A is correct then the intensity of the 605 keV transition should be higher than the transitions placed in

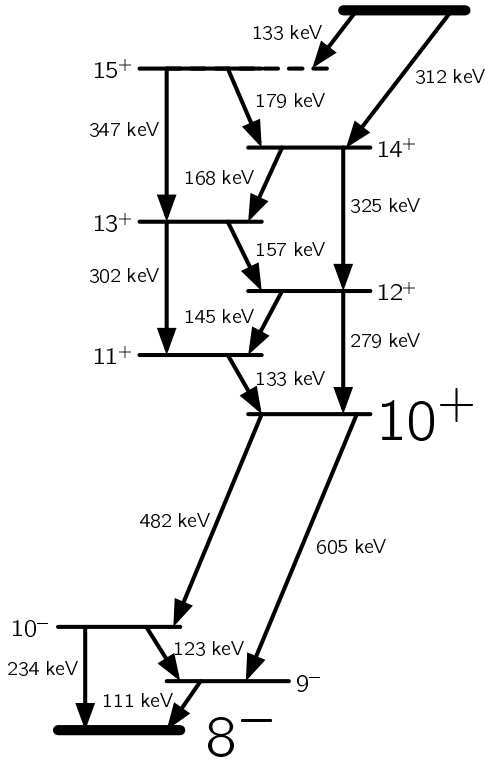

(a) Level scheme A, with an intermediate 10^+ state between the isomers, from Clarke et al. (2010) [49].

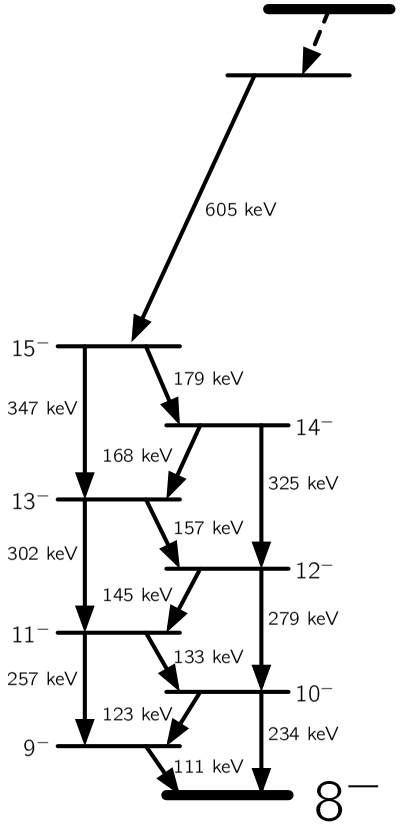

(b) Level scheme B, with an unknown intermediate structure below the fast isomer, from Heßberger et al. (2010) [50].

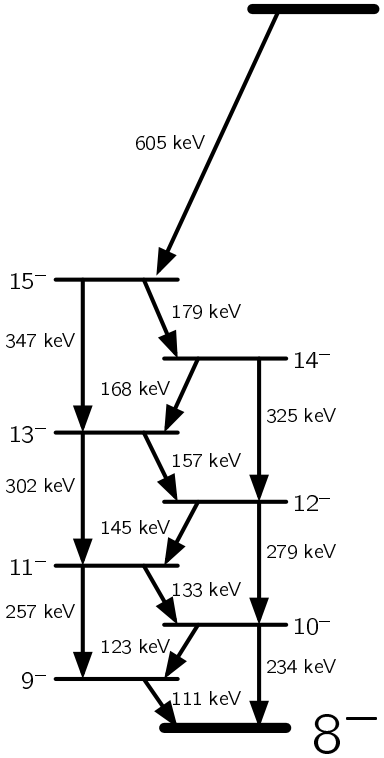

(c) Level scheme C, with a 605 keV transition directly depopulating the fast isomer and no intermediate structure.

Figure 9.1: Possible partial level schemes above the 8^- isomer. Thicker lines show levels which are isomeric.

Table 9.1: Transition intensities above the slow isomer measured in-beam with SAGE compared to previously measured values from decay spectroscopy of the fast isomer. Intensities are corrected for detector efficiency and internal conversion and normalised to the 605 keV peak.

Energy /keV	Area /counts	Intensity (in-beam)	Intensity (decay spectroscopy [49])
159.3(7)	22(10)	3.8(21)	0.99(17)
179(2)	25(12)	3.3(19)	0.90(13)
604(3)	48(15)	1.0(3)	1.00(8)

the 10^+ band above it, but if level scheme B is correct and the 605 keV transition is placed above these transitions (now in an 8^- band) then the intensity of the 605 keV transition should be lower.

The other difference between level scheme A and level scheme B is the 482 keV transition in level scheme A. This is expected to have a low intensity [49] but if it is seen in SAGE then level scheme A is the only one of these three proposals which could be correct.

In this chapter the differences between the level schemes are investigated using the recoil-isomer tagged SAGE spectra by looking for the presence and intensity of γ rays or conversion electrons from the 605 keV or 482 keV transitions. Background from a ^{74}Ge(n,n'γ) reaction is also considered when the 605 keV transition is investigated.

9.1 Intensity of 605 keV transition

The middle and lower panels of figure 9.2 show the recoil-isomer tagged spectra from SAGE. In the spectrum from the germanium detectors it is possible to fit the peaks at 159 keV, 179 keV and 605 keV. The peaks from the transitions expected in the band at 123 keV and 145 keV can't be fitted because they are too close to the peaks from nobelium K_α and K_β X-rays. Table 9.1 gives the energies and intensities of the fitted peaks, with intensity data from a previous decay spectroscopy experiment also listed for comparison. The intensity of the 605 keV peak in the in-beam data is relatively less than in the decay spectroscopy data.

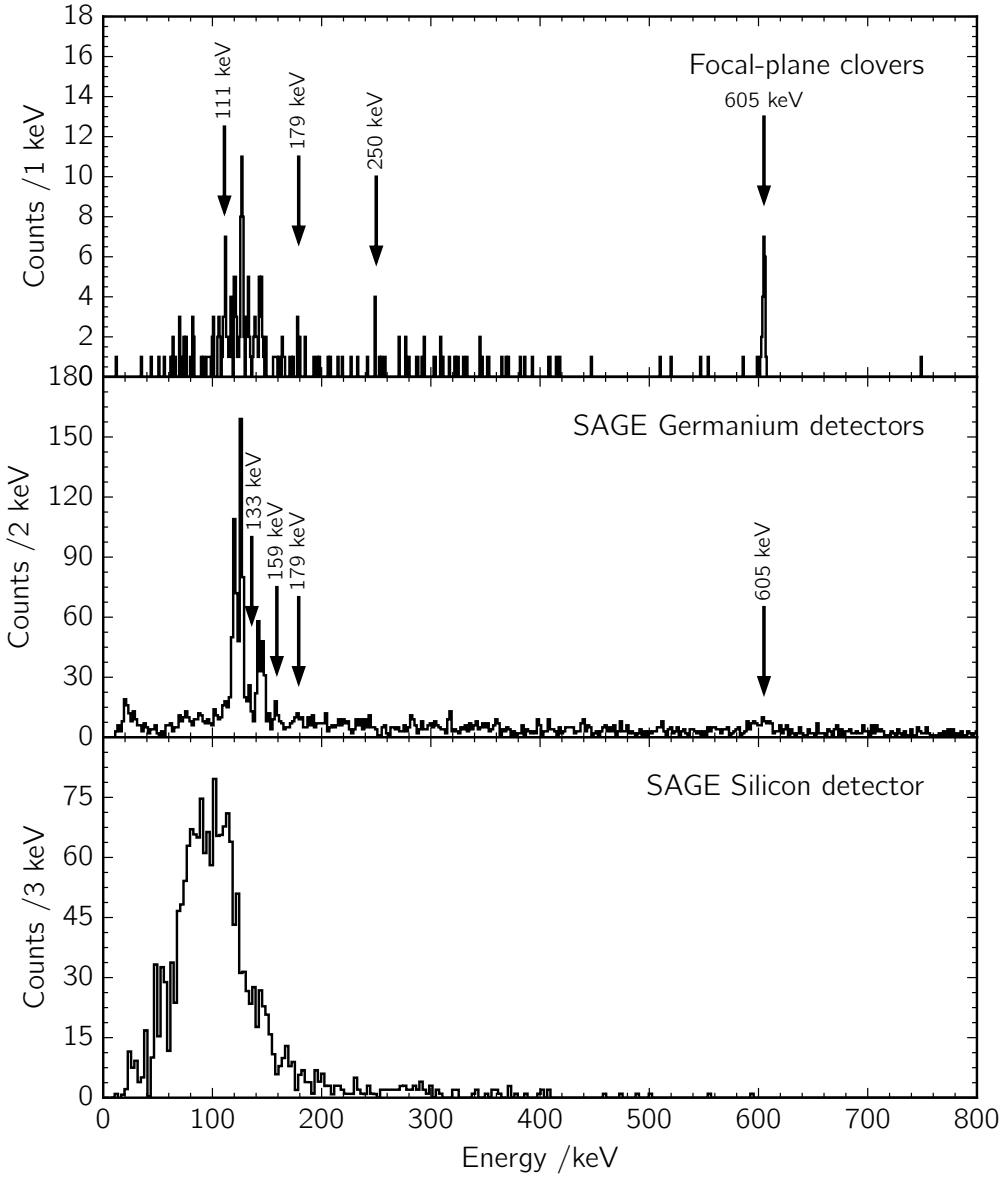

Figure 9.2: Spectra from the focal-plane clover detectors in coincidence with the decay of the fast isomer and from SAGE for prompt data from recoil-isomer tagged events. The top spectrum shows γ rays in the focal-plane clover detectors in coincidence with the decay of the fast isomer. Arrows show some of the γ-ray peaks from ^{254}No. The 250 keV peak has not been seen in any previous experiments and its origin is unknown. There is not enough data to identify any other γ rays in coincidence with it. The middle panel shows the recoil-isomer tagged SAGE germanium detector spectrum. The most prominent peaks are from nobelium X-rays and some of the γ-ray peaks from ^{254}No are labelled. The bottom panel shows the recoil-isomer tagged SAGE silicon detector spectrum after background subtraction.

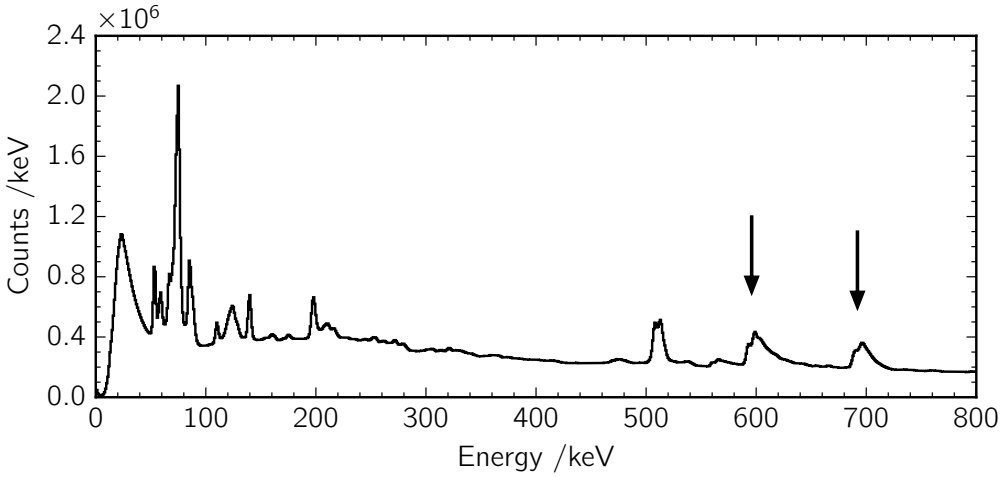

Figure 9.3: Raw spectrum (after Doppler correction) from the SAGE germanium detectors. The arrows show the biggest peaks from Ge(n,n'γ) reactions.

9.2 ^{74}Ge(n,n'γ)

The shape of the 605 keV peak in the SAGE germanium detector spectrum is broader than any of the other γ-ray peaks and the raw SAGE germanium detector spectrum (figure 9.3) has a peak in the same position from the ^{74}Ge(n,n'γ) inelastic neutron scattering reaction ($E_\gamma = 596$ keV [116]) occurring within the detectors. The broad shape of the peak in the raw spectrum, with a tail on the high-energy side, is characteristic of inelastic neutron scattering because the energy of the γ ray is summed with any kinetic energy transferred to the germanium crystal lattice from the neutron [117]. Applying the Doppler correction to the different rings of germanium detectors in SAGE also shifts the peak energies in each of them and broadens the peak in the total spectrum from all three rings.

The ^{208}Pb + ^{48}Ca fusion-evaporation reaction used to make ^{254}No also produces two neutrons. These are emitted in coincidence with ^{254}No recoils and this means any γ rays from neutron scattering can't be removed from the spectrum by the subtraction of random-time background (section 6.2) and all possible recoil-decay tagging chains which identify ^{254}No recoils will also identify γ rays from scattering of the two neutrons.

The time of flight for neutrons from the target position to the germanium detectors is longer than for γ rays but the distance is so short (250 mm [107]) that the time difference is not enough discriminate between them [118].

In this experiment there is not enough data for it to be possible to split the peak at about 605 keV into separate components from ^{254}No and from neutron scattering, but in this section evidence is shown that at least some of the intensity is from the inelastic neutron scattering reaction.

Doppler shift

The γ rays from ^{254}No are Doppler-shifted because the recoiling nuclei are moving relative to the detectors. For the (n,n'γ) reaction the γ rays are emitted from ^{74}Ge nuclei within the detector and there is no Doppler shift. If Doppler correction is not applied to the data then looking at each ring of germanium detectors in SAGE separately should show the ^{254}No γ rays at slightly different energies, E', related to the angle of the detectors, θ, by equation 5.5. Plotting E' against $\cos\theta$ should give a straight line with a positive gradient proportional to the peak energy in the frame of the recoils. The γ rays from the (n,n'γ) reaction are emitted from ^{74}Ge nuclei inside the detector so there is no Doppler shift in their energies.

Figure 9.4 shows that for ^{254}No X-rays and transitions in the ground-state band and out of the 3^+ state the uncorrected energy does increase with $\cos\theta$ but for the peak at about 605 keV there is almost no difference in energy between the different detector rings.

Efficiency of clover germanium detector rings

The position of the SAGE target wheel inside the target chamber means it absorbs γ rays emitted from the target position towards the downstream ring of clover detectors more than γ rays emitted towards the upstream ring of clover detectors. This gives a difference in efficiency between the two rings, despite the geometry of the detectors being the same. Figure 9.5 shows this for the calibration data with

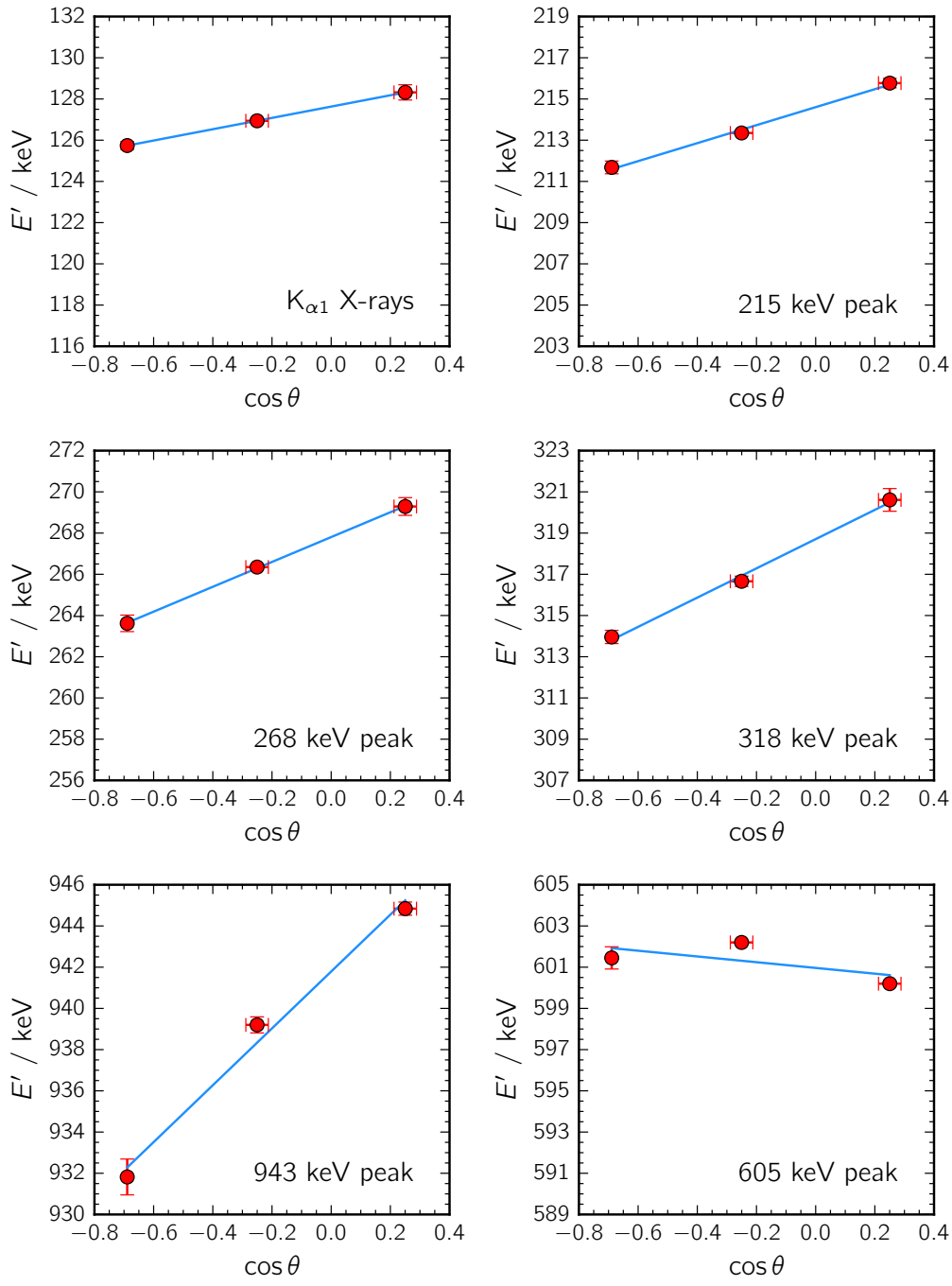

Figure 9.4: Energies of the same peaks in different SAGE germanium detector rings with no Doppler correction. Energies are shown for ^{254}No $K_{\alpha 1}$ X-rays (128 keV), ^{254}No ground-state band peaks (215, 268 and 318 keV), $3^+ \rightarrow$ ground-state band (943 keV) and the 605 keV peak.

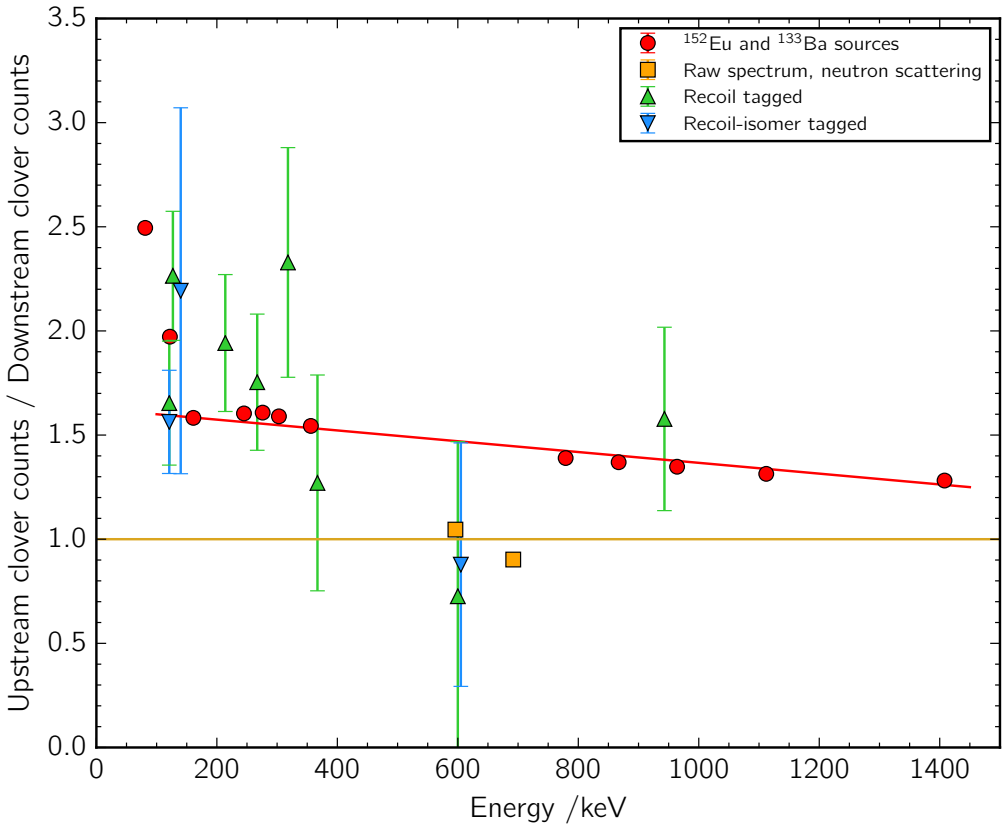

Figure 9.5: Ratio of numbers of counts in the two rings of clover germanium detectors in SAGE. The horizontal line marks where the number of counts in upstream and downstream detector rings is the same. A line has also been drawn through the data points for ^{152}Eu and ^{133}Ba sources to guide the eye. It is not a line of best fit. Error bars on the data points from the ^{152}Eu and ^{133}Ba sources and neutron scattering peaks in the raw spectrum are smaller than the symbols used to plot them.

the ^{152}Eu and ^{133}Ba sources and for γ rays from the recoil-tagged ^{254}No spectrum, where the ratio of number of counts in the two rings is roughly 1.4. For any γ rays emitted by scattering reactions within the germanium detectors there is no shadowing effect from the target wheel and the efficiency is the same in both rings of clover detectors, as shown in figure 9.5 for the neutron scattering peaks from the raw germanium detector spectrum. The ratio of numbers of counts for the 605 keV peak in figure 9.5 is much closer to the raw neutron scattering than the recoil-tagged ^{254}No. This suggests that these γ rays are not emitted at the target position.

Table 9.2: Expected number of electron counts in the SAGE silicon detector from a 605 keV transition in ^{254}No.

Multipolarity	K-shell electrons	L-shell electrons
E1	$1.7(5) \times 10^{-3}$	$0.9(3) \times 10^{-3}$
M1	$5(1) \times 10^{-2}$	$2.5(8) \times 10^{-2}$
E2	$7(2) \times 10^{-2}$	$4(1) \times 10^{-2}$
M2	0.10(3)	0.06(2)

9.3 Conversion electrons from a 605 keV transition

Observation of conversion electrons from a 605 keV transition in ^{254}No would not have the same problems with background from ^{74}Ge(n,n'γ) and could provide unambiguous evidence for the presence of the transition in the in-beam data. The number of electrons detected, N_e, is linked to the number of γ rays, N_γ, by

$$N_e = \frac{\alpha N_\gamma \epsilon_e}{\epsilon_\gamma} \tag{9.1}$$

where α is the conversion coefficient and ϵ_γ and ϵ_e are the efficiencies for detecting γ rays and electrons. The fitted area of the peak at 605 keV (assuming a Gaussian peak shape) is

$$N_\gamma = 48(15) \text{ counts}$$

Assuming that all these counts are ^{254}No γ rays the expected numbers of electrons detected can be calculated assuming different possible multipolarities for the 605 keV transition, and these are listed for the K- and L-shell peaks in table 9.2. For higher multipolarities than these the Weisskopf estimate for the half-life becomes so long that the electrons would not be seen in the prompt data. Rounding any of the numbers of electrons in table 9.2 to the nearest whole count gives zero, the same as if there was no prompt 605 keV transition. No counts are seen at the expected energies in the experimental spectrum, but this does not help to determine if the 605 keV transition is seen in the prompt data.

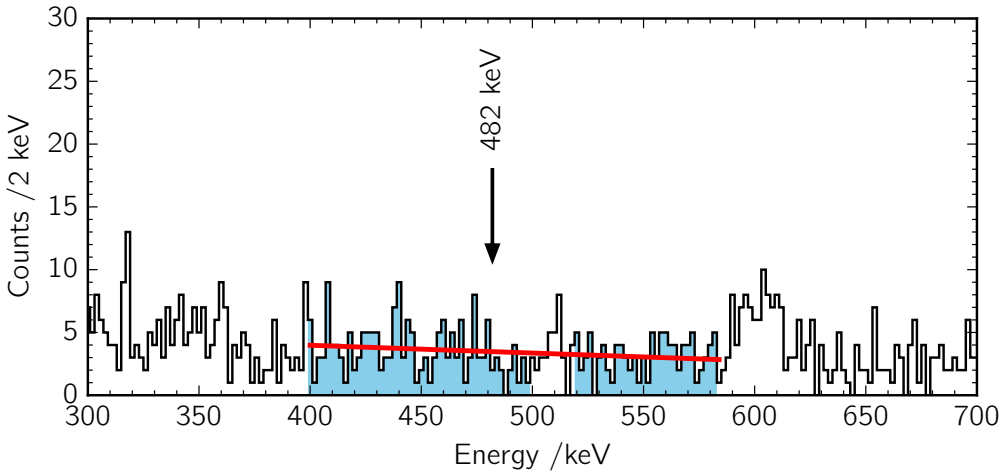

Figure 9.6: Enlarged section of recoil-isomer tagged SAGE germanium detector spectrum, showing the location of the 482 keV peak seen in decay spectroscopy [49]. The shaded area is the region used to find the background when a limit is put on the intensity of the 482 keV peak and the thicker red line is the fitted average background.

9.4 Intensity of a 482 keV transition

Observation of the 482 keV transition from level scheme A in the in-beam data could also help confirm this level scheme without any problems from (n,n'γ) background. There is no obvious peak seen above the background in the SAGE germanium detector spectrum in figure 9.6, but confidence limits can be placed on the possible number of counts from a 482 keV transition using the method described in Feldman and Cousins (1998) [119] for Poisson processes with background.

Any γ rays from this transition are assumed to be in the energy range of 480–484 keV and an average background is calculated from a linear fit to the spectrum in the energy ranges 400–500 keV and 520–584 keV. The background region is chosen to avoid the peaks at 511 keV and 605 keV. Figure 9.6 shows both the regions used to find the background and the average fitted background. At a 90 % confidence

level the limits on the number of counts from a 482 keV transition are:

$$\text{Lower limit} = 0$$

$$\text{Upper limit} = 3.25$$

These can be corrected for detector efficiency, adjusted for internal conversion (assuming E1 multipolarity [49]) and normalised to the 605 keV peak to give intensity values directly comparable with table 9.1,

$$\text{Lower limit} = 0$$

$$\text{Upper limit} = 0.61$$

With the intensity of the 605 keV transition in ^{254}No being hard to determine accurately it is more useful to compare the 482 keV intensity to a different transition. Taking the ratio of intensities of the 179 keV and 482 keV peaks in the decay spectroscopy data gives

$$\frac{I(482\text{ keV})}{I(179\text{ keV})} = 0.078(24)$$

but using SAGE the limits on the ratio are

$$0 < \frac{I(482\text{ keV})}{I(179\text{ keV})} < 0.018(9)$$

There is no evidence in the SAGE data for a 482 keV transition at the intensity expected from level scheme A.

9.5 Decay of the fast isomer

The top panel of figure 9.2 shows the GREAT clover germanium detector spectrum in coincidence with conversion electrons in DSSD-X from the decay of the fast isomer. The peak at 605 keV is much narrower than the peak in the in-beam spectrum and there should be much less neutron-scattering background at the focal plane so it is

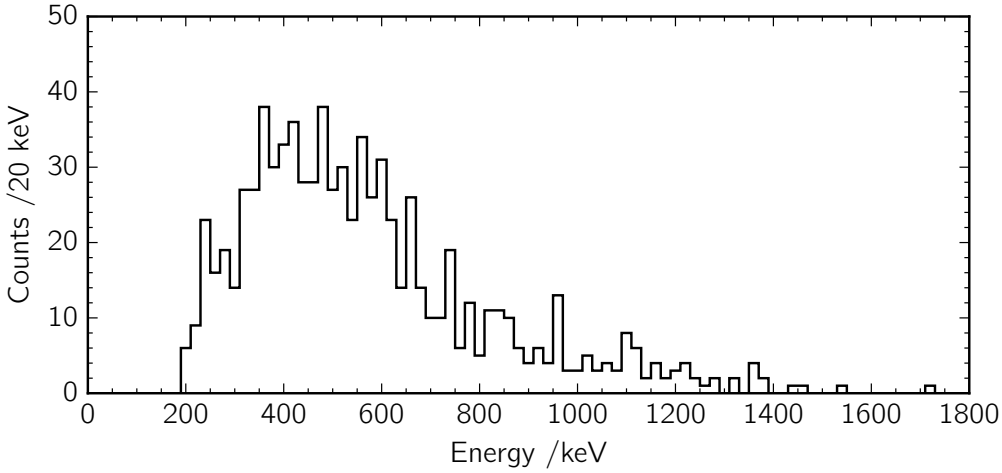

Figure 9.7: Sum of energy from all focal-plane detectors (DSSD, PIN diodes and planar and clover germanium detectors) in the decay of the fast isomer.

assumed that this peak is entirely from a 605 keV transition in ^{254}No.

Focal-plane energy sum

The sum of the energy deposited in all of the focal-plane detectors when the fast isomer decays gives a lower limit on the energy difference between the fast isomer and the slow isomer. Figure 9.7 shows that the total energy spectrum extends up to around 1500 keV. The energy difference between the isomers is greater than this for all three level schemes in figure 9.1 and it is not possible to use this spectrum to rule out any of these level schemes.

9.6 Discussion

If there is an intermediate 10^+ state between the isomers with a 605 keV transition linking it to the band built on the 8^- isomer (level scheme A in figure 9.1) then the intensity of the 605 keV transition in the in-beam data should be at least as much as the transitions placed in the 10^+ band above it. Instead, the in-beam data (table 9.1) shows that the 159 keV and 179 keV transitions have higher intensities than the 605 keV peak. Creating the nucleus directly in a fusion-evaporation reaction would

increase any side feeding of the 605 keV transition from other levels not populated by the decay of the fast isomer. This would increase the intensity of the 605 keV transition relative to those above it in the in-beam data compared to the decay spectroscopy data, which is not what is seen experimentally. The uncertainties on the intensities from SAGE are large, but the difference between the in-beam and decay spectroscopy intensities is still significant.

When the transition intensities are compared they are corrected for internal conversion with the assumption that the 605 keV transition has E1 multipolarity. Changing the multipolarity could increase the intensity of the 605 keV transition in the in-beam data, matching better with level scheme A, but it would also increase the transition's total intensity from the decay spectroscopy data. Changing the intensity of the transition by the same factor in both cases does not change the relative difference in intensity between the in-beam and decay spectroscopy data.

There is evidence from the Doppler shift and relative intensities of the two rings of clover detectors for a peak in the recoil-isomer-tagged spectrum from inelastic neutron scattering at around the same energy as the 605 keV γ rays from ^{254}No. It is not possible to split the peak in the in-beam spectrum into separate components from these two sources or to determine if the peak is entirely due to neutron scattering without any ^{254}No γ rays. If the peak is split then the intensity of the transition in ^{254}No is reduced even more and level scheme A is still inconsistent with the SAGE data.

If all the intensity of the in-beam 605 keV peak is from neutron scattering then the transition in ^{254}No can directly depopulate the fast isomer (as shown in level scheme C). If there is a contribution from a transition in ^{254}No then there must be an unknown intermediate structure between the fast isomer and the 605 keV transition (as shown in level scheme B), or there could be a 605 keV doublet in ^{254}No with one transition depopulating the fast isomer and the other somewhere else in the level scheme. Without determining unambiguously the source of the peak seen in SAGE it is not possible to rule out any of these cases. If there are two different 605 keV

transitions then they will have the same Doppler shift and be even more difficult to separate than γ rays from ^{254}No and from the (n,n'γ) reaction.

The 605 keV γ rays seen at the focal plane in coincidence with the decay of the fast isomer confirm that there is a transition with this energy in ^{254}No somewhere between the two isomers, but it does not give any more information about where in the level scheme the transition should be placed. Any of the level schemes in figure 9.1 is consistent with this observation.

Spin and parity of the fast isomer

If level scheme C is correct then the fast isomer decays by the 605 keV transition into the 15^- level in the band in the band built on the slow isomer [49, 50]. This suggests a spin of 16 for the fast isomer and coupling together two 8^- excitations can produce a 16^+ four-quasiparticle configuration. If the 605 keV transition does directly depopulate a 16^+ isomer to a 15^- level then it would have E1 multipolarity. With a half-life of 184 µs the reduced hindrance factor (section 3.3) for the decay is

$$f_\nu = 42$$

This is within the expected range for K-hindered decays [38] and level scheme C remains plausible with a 16^+ assignment for the fast isomer.

Chapter 10

Structure of the $K^{\pi} = 8^{-}$ isomer

If all the transitions observed above the 8^{-} isomer are placed in a single rotational band (as in level schemes B or C from figure 9.1) then the method described in chapter 7 can be used to find the value of g_K for the bandhead. This can then be compared to calculated values of g_K for different possible single-particle states with the right spin and parity to determine which of these is most likely to be the single-particle structure of the isomer.

10.1 Finding g_K for the slow isomer

The M1 and E2 electron regions are shown again in figure 10.1 and their limits are:

$$\text{M1 region} = 40\text{–}180 \text{ keV}$$

$$\text{E2 region} = 200\text{–}370 \text{ keV}$$

The background curve (equation 7.3) with the parameters $a = 240$, $b = 36$ and $c = -0.02$ is also shown in figure 10.1. The electric quadrupole moment of ^{254}No used to calculate $B(\text{E2})$ for the simulations is $Q_0 = 13.3$ eb [56].

The E2/M1 electron intensity ratio is shown for experimental and simulated spectra in figure 10.2. The crossing of the experimental value and the line connecting the

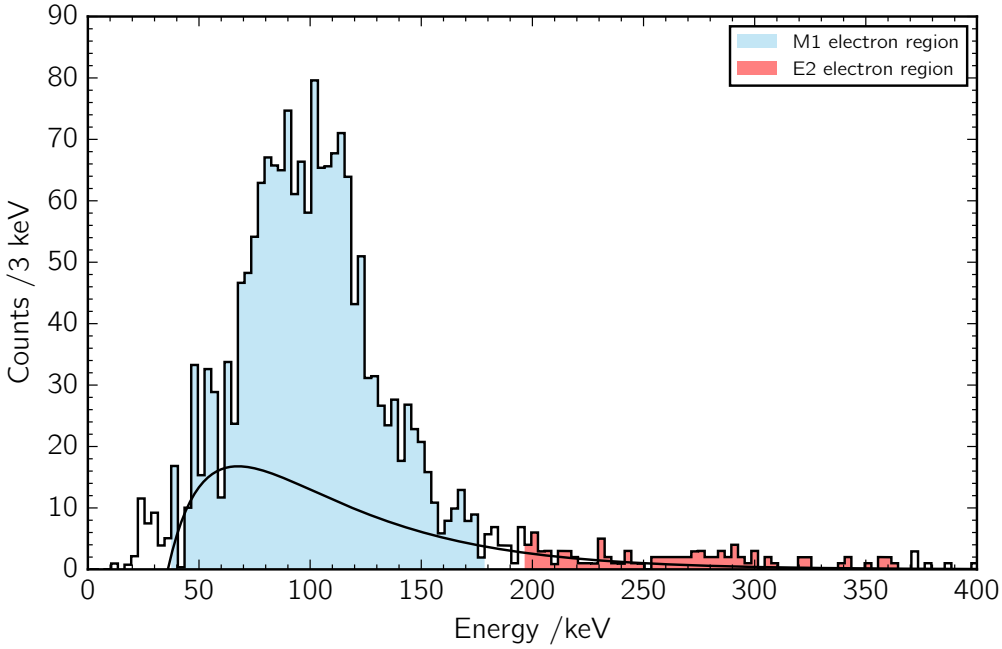

Figure 10.1: Experimental recoil-isomer tagged SAGE silicon detector spectrum. The shaded areas show the E2 and M1 electron regions and the smooth black line is the modelled background which is subtracted from the area of each region.

simulated points gives a pair of possible $g_K - g_R$ values for the band,

$$g_K - g_R = -0.16^{+0.05}_{-0.09}$$
$$g_K - g_R = +0.16^{+0.09}_{-0.05}$$

The nominal value of $g_K - g_R$ is taken from the average experimental ratio (the solid green line in figure 10.2) and the uncertainties include the range of values within the uncertainties both with and without subtraction of modelled background from the spectrum (everything within the two shaded green regions in figure 10.2).

10.2 Discussion

There are three possible 8^- two-quasiparticle configurations in ^{254}No which are predicted to be at about the right energy for the slow isomer [121–123]. Table 10.1

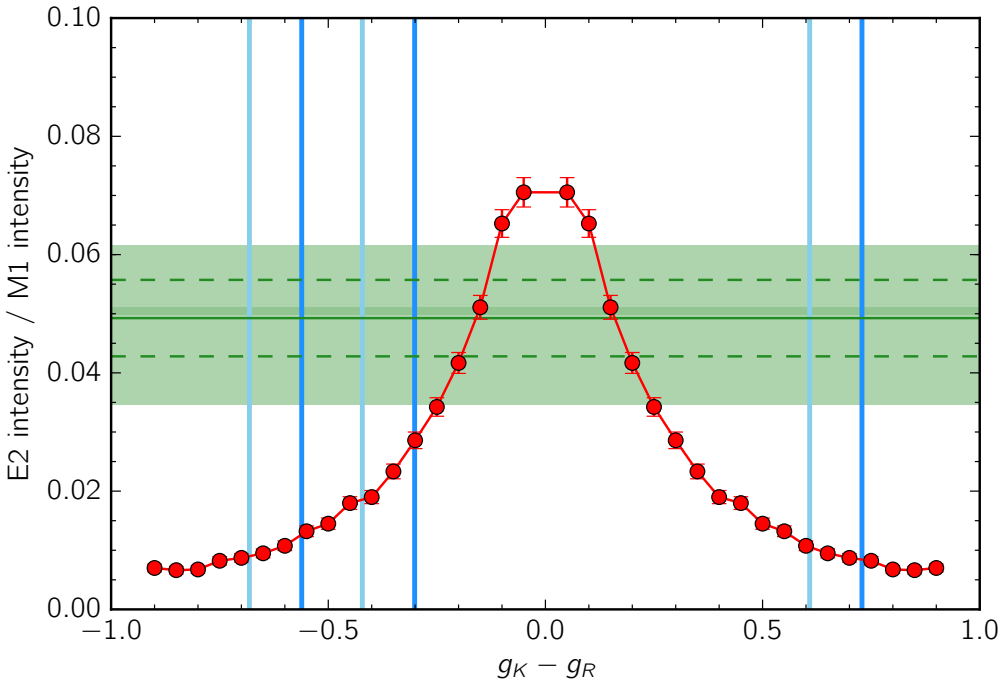

Figure 10.2: E2/M1 electron intensity ratio from experimental and simulated SAGE spectra. The dashed green horizontal lines show the experimental ratios with (lower line) and without (upper line) subtracting the modelled background, with lighter green bands either side showing the uncertainty on each. The solid green line is the average of these two values. The red lines shows the ratio from `Geant4` simulations. The vertical lines mark the values of $g_K - g_R$ for three calculated 8^- states, with unquenched g_R in light blue and quenched g_R in dark blue.

Table 10.1: Possible quasiparticle configurations for the 8^- isomer, with calculated g_K values (from the `swbeta` code [120]) and $g_K - g_R$ for unquenched and quenched rotational g factors. The spin g factors, g_s, for the protons and neutrons are reduced from the values for free nucleons by a factor of 0.7.

Configuration	g_K	$g_K - g_R$ (unquenched)	$g_K - g_R$ (quenched)
$\frac{7}{2}^+[613]_\nu \otimes \frac{9}{2}^-[734]_\nu$	-0.28	-0.68	-0.56
$\frac{7}{2}^+[624]_\nu \otimes \frac{9}{2}^-[734]_\nu$	-0.02	-0.42	-0.30
$\frac{7}{2}^-[514]_\pi \otimes \frac{9}{2}^+[624]_\pi$	+1.01	+0.61	+0.73

lists them with their calculated g_K values and $g_K - g_R$ for each configuration with unquenched ($g_R = Z/A = 0.402$) and quenched ($g_R = 0.7 \times Z/A = 0.281$) rotational g factors. Comparing the $g_K - g_R$ values for each configuration with the values found from figure 10.2 shows that none of them are within the uncertainty for either experimental value, but the

$$\left\{ \tfrac{7}{2}^{+}\,[624]_{\nu} \otimes \tfrac{9}{2}^{-}\,[734]_{\nu} \right\}^{8^{-}}$$

two quasi-neutron structure with a quenched g_R is closest.

Previous experiments [56] have given the structure of the isomer as the two-proton state, based on γ-rays seen in coincidence with the decay of the fast isomer. The value of $g_K - g_R$ was calculated from the E2/M1 γ-ray branching ratio out of levels in the band built on the isomer. A separate value was found using the transitions depopulating each level. The values found were

$$g_K - g_R = -0.60(8)$$
$$g_K - g_R = +0.60(8)$$

There were only three levels where the intensity of both the transitions were big enough to be measured, so this result is based only on those. The method used to find the values of $g_K - g_R$ in the current work should be sensitive to conversion electrons from transitions depopulating all levels in the band.

The two-neutron assignment suggested here for the isomer is the same as for the 8^{-} isomers in the $N = 150$ isotones, including ^{252}No, but a proposed $N = 152$ deformed shell gap would be expected to increase the excitation energy of two-neutron states in $N = 152$ nuclei above the two-proton state [122]. Not all calculations predict a deformed shell gap at $N = 152$. There are also HFB calculations using the Skyrme SLy4 interaction for ^{250}Fm which prefer a gap at $N = 150$ [124] and projected shell model calculations which predict $\frac{7}{2}^{+}\,[624]_{\nu} \otimes \frac{9}{2}^{-}\,[734]_{\nu}$ to be the

lowest-lying 8^- state in ^{254}No [62].

Comparison with hafnium isotopes

In the rare-earth region where K isomerism is also common both ^{176}Hf and ^{178}Hf have two 8^- states (one two-proton $\frac{7}{2}^+[404]_\pi \otimes \frac{9}{2}^-[514]_\pi$ and one two-neutron $\frac{7}{2}^-[514]_\nu \otimes \frac{9}{2}^+[624]_\nu$). Only the lower-lying of the two states is isomeric but γ rays from rotational bands built on both configurations have been seen experimentally in both nuclei [76, 125]. Figure 10.3 shows partial level schemes for both isotopes. Similarly to this, it is likely that in ^{254}No all three possible 8^- configurations exist, even if they have not yet all been identified.

The method used to determine g_K assumes on all electrons are from the same band or are part of a modelled background based on the recoil-tagged data. This is likely to be true if the transitions within the 8^-_1 isomeric band are more intense than those in any other band. Without being able to measure and compare the intensity of γ rays from more than one 8^- band this can't be checked experimentally, but in both the hafnium isotopes the intensity of transitions within the 8^-_2 bands are less than within the 8^-_1 band. Assuming that ^{254}No is similar the other 8^- states should not affect the determination of g_K for the slow isomer.

Conversion electrons from transitions between the 8^- bands could also be a problem. The transitions between the bands link levels with $\Delta I = 0$ or $\Delta I = 1$ and have M1 multipolarity. These could give extra electrons in the M1 region of the silicon detector spectrum. The spacing of levels within the 8^- bands are similar (because the moments of inertia are similar) and these transitions can be grouped into two sets ($\Delta I = 0$ or $\Delta I = 1$) with similar energies within each set. The actual energies of the transitions depend on the energy difference between the bandheads. If the transitions have similar energies then any electrons from them will also have similar energies and would be likely to form a broad peak in the electron spectrum, instead of being spread evenly through it. This wouldn't be possible to remove with the current modelled background shape, but if there were a significant number

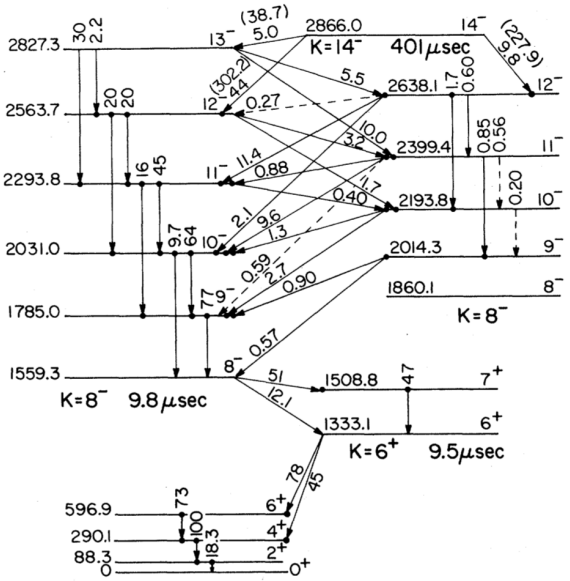

(a) Partial level scheme for ^{176}Hf. The transitions are labelled with their γ-ray intensities measured in the decay of the 14^{-} isomer. Based on figure 1 from Khoo et al. (1975) [76].

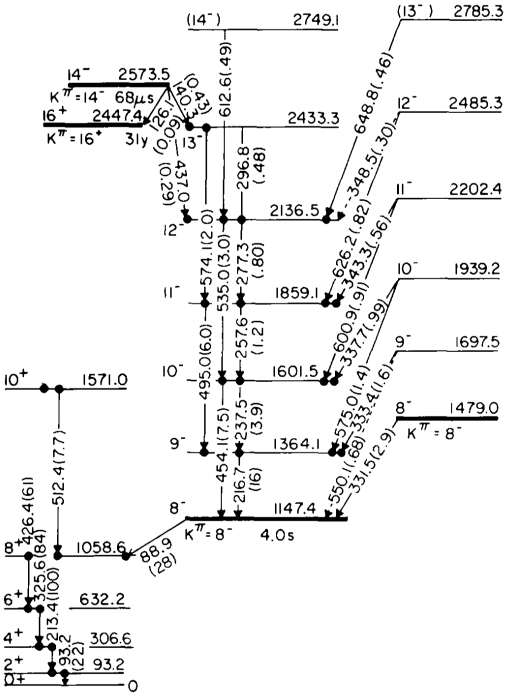

(b) Partial level scheme for ^{178}Hf. The transitions are labelled with their energies and (in brackets) their γ-ray intensities measured in the ^{176}Yb(α,2n)^{178}Hf reaction. Based on figure 1 from Khoo et al. (1977) [125].

Figure 10.3: Partial level schemes for 8^{-} isomers in hafnium isotopes.

of electrons from this source they would be more obvious in the spectrum if they were all grouped together and nothing like this is seen experimentally. Depending on the energy difference between the 8^- states these transitions could have higher energies than the M1 transitions within the 8^-_1 band giving them smaller conversion coefficients and reducing their contribution to the electron spectrum.

Mixing between two-proton and two-neutron states with the same K^π is also seen in the hafnium isotopes [125, 126], but in ^{254}No this has not been considered.

Chapter 11

Conclusions

11.1 Structure of *K* isomers in ^{254}No

The aims of this experiment were to determine which, if either, of the two most recently proposed level schemes above the 8^- isomer in ^{254}No was correct and to determine the single-particle structure of the isomeric states. It has been shown that one of the level schemes is not consistent with the in-beam data from SAGE and that it is likely that all observed transitions lie in a single rotational band. It is also possible that the fast isomer is depopulated directly by a 605 keV transition, with no intermediate structure, but the limited amount of data makes it impossible to completely separate any transition at this energy in ^{254}No from the background ^{74}Ge(n,n'γ) peak at around the same energy.

The separation of peaks from ^{254}No and from neutron scattering by their different Doppler shifts would be greater with detectors closer to 0° or 90° to the beam direction, instead of the two rings of clover detectors at closer to 90° in SAGE, which might make resolving them easier. This is difficult because detectors at small angles in the downstream direction are hard to fit around a recoil separator and in the upstream direction the SAGE silicon detector couldn't be used. Using scintillator detectors for γ rays instead of germanium would remove the background peak, but the worse energy resolution would make identifying peaks from γ rays in the rotational band built on the 8^- isomer even harder.

Even if all transitions seen above the 8^- isomer are in the same rotational band

this is not enough to determine the single-particle structure of the isomeric state. This work has developed a method to investigate the structure of the isomer using the prompt conversion-electron spectrum without having to be able to fit individual peaks in the γ-ray spectrum. This method has also been tested to check that it is not strongly sensitive to any of the choice of parameters used when it is applied. Advances in instrumentation (combining both γ-ray and conversion electron spectroscopy with SAGE) and data acquisition (switching from analogue to digital electronics) have lowered the limit of feasible cross sections for in-beam studies of transfermium nuclei and development of analysis methods for use with limited amounts of data should also help this.

The conversion-electron spectrum suggests a two-neutron $\frac{7}{2}^{+}[624]_{\nu} \otimes \frac{9}{2}^{-}[734]_{\nu}$ configuration for the 8^{-} isomer, unlike previous assignments from γ-ray spectroscopy of a two-proton state [56]. The two-neutron assignment is the same as all the assigned 8^{-} isomers in the $N = 150$ isotones but for the $N = 152$ isotones there are no other isomers with structural assignments. More data for these nuclei would be useful to provide an overview in any systematic trends in isomeric configurations in the transfermium region. ^{252}Fm would be a particularly interesting case to compare with ^{250}Fm, ^{252}No and ^{254}No to see the effects of changing either the proton number or the neutron number, but unlike these three it can't be produced by a cold-fusion reaction of a ^{48}Ca beam on a stable target. An ^{18}O beam on a ^{238}U target could be used but the recoils would have very low energy. The long half-life (25.39(4) hours [127]) would also make recoil-decay tagging very hard, but as long as the reaction channel is clean tagging on the decay of isomers with shorter half-lives would be easier.

Extending the data to heavier nuclei is difficult because of the decreasing production cross sections, but more data on isomeric states in some of the curium and californium isotopes could also be helpful. Beam intensities for in-beam spectroscopy are limited by background rates in the detectors at the target position and decay spectroscopy can't be used to investigate the levels above isomeric states unless they are fed by

decay of another isomer. Detailed studies of isomers in nuclei with much smaller production cross sections will require either longer experiments or further advances in instrumentation.

11.2 Measuring conversion coefficients with SAGE

Although this work has not extended the level scheme for the ground-state band the simultaneous detection of γ rays and conversion electrons has allowed conversion coefficients to be measured for some transitions. For a rotational band built on a $K^\pi = 0^+$ bandhead it is known that all transitions must have E2 multipolarity, but the measurement shows that, if there is enough data to be able to fit peaks in both the γ-ray and electron spectra, SAGE can directly determine transition multipolarity. There are other cases in which this could be used to assign spins and parities of the states linked by a transition. The uncertainties on the conversion coefficients from SAGE are large, but there are several orders of magnitude difference between calculated conversion coefficients for different multipolarities, and when comparing measured values with those from `BrIcc` the transition multipolarity can be easily determined.

The conversion coefficient for a transition decreases rapidly with energy, making conversion coefficients harder to measure at higher energies because it is much less likely that a statistically significant electron peak is seen in SAGE. The efficiency of SAGE for detecting either γ rays or electrons also decreases with increasing energy but the effect of this is smaller. Unfortunately many of the transitions in ^{254}No for which measuring the conversion coefficient would be most useful are the higher-energy transitions linking different bands. The lower-energy transitions within rotational bands are of less interest as their multipolarity can already be deduced from their placement in the level scheme.

References

[1] D.C. Hoffman, A. Ghiorso and G.T. Seaborg, *The Transuranium People: The Inside Story*, World Scientific Publishing (2000) [see p. 1]

[2] S. Hofmann, *On Beyond Uranium: Journey to the end of the Periodic Table*, Taylor & Francis (2002) [see p. 1]

[3] Yu.Ts. Oganessian, V.K. Utyonkov, Yu.V. Lobanov et al., *Phys. Rev. C* **74** (2006) 044602 [see p. 1]

[4] D. Rudolph, U. Forsberg, P. Golubev et al., *Phys. Rev. Lett.* **111** (2013) 112502 [see p. 1]

[5] R.-D. Herzberg and P.T. Greenlees, *Prog. Part. Nucl. Phys.* **61** (2008) 674–720 [see p. 2]

[6] R.-D. Herzberg, *Nuclear Structure of Superheavy Elements* in M. Schädel and D. Shaughnessy, *The Chemistry of Superheavy Elements*, Springer (2013) [see p. 4]

[7] C.F.v. Weizsäcker, *Z. Phys.* **96** (1935) 431–458 [see p. 3]

[8] R.F. Casten, *Nuclear Structure from a Simple Perspective, Second edition*, Oxford University Press (2000) [see pp. 4 and 17]

[9] M. Goeppert-Mayer, *Phys. Rev.* **74** (1948) 235–239 [see p. 5]

[10] O. Haxel, J.H.D. Jensen and H.E. Suess, *Naturwissenschaften* **35** (1948) 376 [see p. 6]

[11] M. Goeppert-Mayer, *Phys. Rev.* **75** (1949) 1969–1970 [see p. 6]

[12] R.D. Woods and D.S. Saxon, *Phys. Rev.* **95** (1954) 577–578 [see p. 7]

[13] R.B. Firestone, *Table of Isotopes, Eighth edition*, John Wiley & Sons (1996) [see pp. 9, 10, and 28]

[14] S.G. Nilsson, *K. Dan. Vidensk. Selsk. Mat. Fys. Medd.* **29** (1955) 1–69 [see p. 8]

[15] A. Bohr and B.R. Mottelson, *Nuclear Structure (Volume II)*, W. A. Benjamin (1975) [see pp. 13, 14, 15, and 32]

[16] L. Grodzins, *Annu. Rev. Nucl. Sci.* **18** (1968) 291–342 [see p. 15]

[17] K.S. Krane, *Introductory Nuclear Physics*, John Wiley & Sons, Inc (1988) [see pp. 16 and 29]

[18] V.M. Strutinsky, *Nucl. Phys. A* **95** (1967) 420–422 [see p. 18]

[19] V.M. Strutinsky, *Nucl. Phys. A* **122** (1968) 1–33 [see p. 18]

[20] A. Parkhomenko and A. Sobiczewski, *Acta Phys. Pol. B* **35** (2004) 2447–2471 [see p. 20]

[21] A. Parkhomenko and A. Sobiczewski, *Acta Phys. Pol. B* **36** (2005) 3115–3137 [see p. 20]

[22] M. Bender, W. Nazarewicz and P.-G. Reinhard, *Phys. Lett. B* **515** (2001) 42–48 [see pp. 21 and 22]

[23] D.R. Hartree, *Math. Proc. Cambridge Philos. Soc.* **24** (1928) 111-132 [see p. 20]

[24] M. Bender, P.-H. Heenen and P.-G. Reinhard, *Rev. Mod. Phys.* **75** (2003) 121–180 [see p. 20]

[25] T.H.R. Skyrme, *Nucl. Phys.* **9** (1958) 615–634 [see p. 20]

[26] P. Ring and P. Schuck, *The Nuclear Many-Body Problem*, Springer (2004) [see p. 22]

[27] M. Bender, K. Rutz, P.-G. Reinhard, J.A. Maruhn and W. Greiner, *Phys. Rev. C* **60** (1999) 034304 [see p. 22]

[28] S.E. Agbemava, A.V. Afanasjev, T. Nakatsukasa and P. Ring, *Phys. Rev. C* **92** (2015) 054310 [see p. 22]

[29] S. Ćwiok, J. Dobaczewski, P.-H. Heenen, P. Magierski and W. Nazarewicz, *Nucl. Phys. A* **611** (1996) 211–246 [see p. 22]

[30] P.M. Whelan and M.J. Hodgson, *Essential Pre-University Physics*, John Murray (1971) [see p. 23]

[31] H. Geiger and J.M. Nuttall, *Philos. Mag. (series 6)* **22** (1911) 613–621 [see p. 24]

[32] O. Hahn and L. Meitner, *Z. Phys.* **26** (1924) 161–168 [see p. 27]

[33] T. Kibédi, T.W. Burrows, M.B. Trzhaskovskaya, P.M. Davidson and C.W. Nestor Jr., *Nucl. Instrum. Meth. A* **589** (2008) 202–229 [see p. 30]

[34] V.F. Weisskopf, *Phys. Rev.* **83** (1951) 1073 [see p. 30]

[35] P. Walker and G. Dracoulis, *Nature* **399** (1999) 35–40 [see pp. 32, 33, and 34]

[36] B. Kourchatow, I. Kourchatow, L. Kourchatow, L. Myssowsky and L. Roussinow, *C. R. Acad. Sci.* **200** (1935) 1201–1203 [see p. 32]

[37] G.D. Dracoulis, P.M. Walker and F.G. Kondev, *Rep. Prog. Phys.* **79** (2016) 076301 [see p. 32]

[38] F.G. Kondev, G.D. Dracoulis and T. Kibédi, *Atom. Data Nucl. Data* **103–104** (2015) 50–105 [see pp. 33 and 108]

[39] R.-D. Herzberg and D.M. Cox, *Radiochim. Acta* **99** (2011) 441–457 [see p. 33]

[40] L.I. Rusinov, *Sov. Phys. Usp.* **282** (1961) 282–290 [see p. 34]

[41] P.M. Walker, G.D. Dracoulis, A.P. Byrne, T. Kibédi and A.E. Stuchbery, *Phys. Rev. C* **49** (1994) 1718–1721 [see p. 34]

[42] K.E.G. Löbner, *Phys. Lett. B* **26** (1968) 369–370 [see p. 34]

[43] P.R. Fields, A.M. Friedman, J. Milsted et al., *Phys. Rev.* **107** (1957) 1460–1462 [see p. 35]

[44] A. Ghiorso, T. Sikkeland, J.R. Walton and G.T. Seaborg, *Phys. Rev. Lett.* **1** (1958) 18–21 [see p. 35]

[45] G. Münzenberg, *Nucl. Phys. A* **693** (2001) 207–218 [see p. 35]

[46] Yu.Ts. Oganessian, *J. Phys. G* **34** (2007) R165–R242 [see p. 35]

[47] H.W. Gäggeler, D.T. Jost, A. Türler et al., *Nucl. Phys. A* **502** (1989) 561c–569c [see pp. 36 and 42]

[48] A.V. Belozerov, M.L. Chelnokov, V.I. Chepigin et al., *Eur. Phys. J. A* **16** (2003) 447–456 [see pp. 36 and 42]

[49] R.M. Clark, K.E. Gregorich, J.S. Berryman et al., *Phys. Lett. B* **690** (2010) 19–24 [see pp. 37, 39, 96, 97, 104, 105, and 108]

[50] F.P. Heßberger, S. Antalic, B. Sulignano et al., *Eur. Phys. J. A* **43** (2010) 55–66 [see pp. 37, 39, 96, and 108]

[51] A. Bhagwat, N.J. Thompson and J.K. Tuli, *Nucl. Data Sheets* **105** (2005) 959–986 [see p. 36]

[52] G. Audi, F.G. Kondev, M. Wang et al., *Chin. Phys. C* **36** (2012) 1157–1286 [see p. 36]

[53] P. Reiter, T.L. Khoo, C.J. Lister et al., *Phys. Rev. Lett.* **82** (1999) 509–512 [see p. 36]

[54] M. Leino, H. Kankaanpää, R.-D. Herzberg et al., *Eur. Phys. J. A* **6** (1999) 63–69 [see p. 36]

[55] S. Eeckhaudt, *Spectroscopy in the transfermium region: probing rotational, non-yrast and isomeric structures in* ^{253,254}*No*, PhD thesis, University of Jyväskylä (2006) [see pp. 36 and 38]

[56] C. Gray-Jones, *Isomer spectroscopy of* ^{254}*No*, PhD thesis, University of Liverpool (2008) [see pp. 36, 39, 109, 112, and 117]

[57] S.M. Harris, *Phys. Rev.* **138** (1965) B509–B513 [see p. 36]

[58] P.A. Butler, R.D. Humphreys, P.T. Greenlees et al., *Phys. Rev. Lett.* **89** (2002) 202501 [see pp. 36 and 65]

[59] R.D. Humphreys, *In-beam electron spectroscopy of* ^{254}*No and* ^{226}*U in conjunction with a gas-filled recoil separator*, PhD thesis, University of Liverpool (2003) [see pp. 36 and 81]

[60] S. Eeckhaudt, P.T. Greenlees, N. Amzal et al., *Eur. Phys. J. A* **26** (2005) 227–232 [see p. 38]

[61] A. Ghiorso, K. Eskola, P. Eskola and M. Nurmia, *Phys. Rev. C* **7** (1973) 2032–2036 [see p. 38]

[62] R.-D. Herzberg, P.T. Greenlees, P.A. Butler et al., *Nature* **442** (2006) 896–899 [see pp. 38, 39, and 113]

[63] S.K. Tandel, T.L. Khoo, D. Seweryniak et al., *Phys. Rev. Lett.* **97** (2006) 082502 [see pp. 38 and 39]

[64] P.G. Hansen, K. Wilsky, C.V.K. Baba and S.E. Vandenbosch, *Nucl. Phys.* **45** (1963) 410–416 [see p. 40]

[65] R.W. Hoff, T. von Egidy, R.W. Lougheed et al., *Phys. Rev. C* **29** (1984) 618–622 [see p. 40]

[66] S. Ketelhut, *Rotational structures and high-K isomerism in* ^{248,250}*Fm*, PhD thesis, University of Jyväskylä (2010) [see p. 40]

[67] D. Peterson, B.B. Back, R.V.F. Janssens et al., *Phys. Rev. C* **74** (2006) 014316 [see p. 40]

[68] A.P. Robinson, T.L. Khoo, I. Ahmad et al., *Phys. Rev. C* **78** (2008) 034308 [see p. 40]

[69] K. Katori, I. Ahmad and A.M. Friedman, *Phys. Rev. C* **78** (2008) 014301 [see p. 40]

[70] D.C. Rostron, *Spectroscopy of ^{250}Fm using tagging techniques*, PhD thesis, University of Liverpool (2009) [see p. 40]

[71] E. Parr, *Spectroscopy of excited states in ^{252}No*, PhD thesis, University of Liverpool (2011) [see p. 40]

[72] H.M. David, J. Chen, D. Seweryniak et al., *Phys. Rev. Lett.* **115** (2015) 132502 [see pp. 40 and 41]

[73] U. Shirwadkar, *Spectroscopy of heavy elements: K-isomers in ^{246,248}Cm*, PhD thesis, University of Massachusetts Lowell (2009) [see p. 40]

[74] H.B. Jeppesen, I. Dragojević, R.M. Clark et al., *Phys. Rev. C* **79** (2009) 031303(R) [see p. 40]

[75] A.P. Robinson, T.L. Khoo, D. Seweryniak et al., *Phys. Rev. C* **83** (2011) 064311 [see pp. 40 and 41]

[76] T.L. Khoo, F.M. Bernthal, R.A. Warner, G.F. Bertsch and G. Hamilton, *Phys. Rev. Lett.* **35** (1975) 1256–1259 [see pp. 41, 113, and 114]

[77] M.B. Smith, P.M. Walker, G.C. Ball et al., *Phys. Rev. C* **68** (2003) 031302(R) [see p. 41]

[78] E. Liukkonen, in *Cyclotrons and their Applications: Proceedings of the 13th International Conference, Vancouver 1992*, World Scientific, Singapore (1993) 22–27 [see p. 42]

[79] P. Papadakis, *Combining in-beam γ-ray and conversion electron spectroscopy: The SAGE spectrometer*, PhD thesis, University of Liverpool (2010) [see pp. 44, 47, and 48]

[80] J. Pakarinen, P. Papadakis, J. Sorri et al., *Eur. Phys. J. A* **50** (2014) 53 [see pp. 44 and 48]

[81] G. Duchêne, F.A. Beck, P.J. Twin et al., *Nucl. Instrum. Meth. A* **432** (1999) 90–110 [see p. 46]

[82] C.W. Beausang, S.A. Forbes, P. Fallon et al., *Nucl. Instrum. Meth. A* **313** (1992) 37–49 [see p. 46]

[83] T.K. Alexander, C. Broude, O. Häusser and J.F. Sharpey-Schafer, *Nucl. Instrum. Meth.* **65** (1968) 169–172 [see p. 46]

[84] J.F. Sharpey-Schafer and J. Simpson, *Prog. Part. Nucl. Phys.* **21** (1988) 293–400 [see p. 46]

[85] J. Sorri, *Electron spectroscopy with the SAGE spectrometer*, PhD thesis, University of Jyväskylä (2016) [see p. 48]

[86] M. Leino, J. Äystö, T. Enqvist et al., *Nucl. Instrum. Meth. B* **99** (1995) 653–656 [see p. 50]

[87] J. Sarén, J. Uusitalo, M. Leino and J. Sorri, *Nucl. Instrum. Meth. A* **654** (2011) 508–521 [see pp. 50 and 54]

[88] W.E. Lamb, *Phys. Rev.* **58** (1940) 696–702 [see p. 51]

[89] J. Sarén, *The ion-optical design of the MARA recoil separator and absolute transmission measurements of the RITU gas-filled recoil separator*, PhD thesis, University of Jyväskylä (2011) [see p. 51]

[90] R.D. Page, A.N. Andreyev, D.E. Appelbe et al., *Nucl. Instrum. Meth. B* **204** (2003) 634–637 [see pp. 52 and 53]

[91] A.N. Andreyev, P.A. Butler, R.D. Page et al., *Nucl. Instrum. Meth. A* **533** (2004) 422–434 [see pp. 53 and 58]

[92] A. Georgiev and W. Gast, *IEEE Trans. Nucl. Sci.* **40** (1993) 770–779 [see p. 55]

[93] I.H. Lazarus, D.E. Appelbe, P.A. Butler et al., *IEEE Trans. Nucl. Sci.* **48** (2001) 567–569 [see p. 55]

[94] P. Rahkila, *Nucl. Instrum. Meth. A* **595** (2008) 637–642 [see p. 55]

[95] A.N. Andreyev, D. Ackermann, F.P. Heßberger et al., *Nucl. Instrum. Meth. A* **533** (2004) 409–421 [see p. 56]

[96] W.H. Trzaska, *Nucl. Instrum. Meth. A* **297** (1990) 223–229 [see p. 56]

[97] D.C. Radford, *Nucl. Instrum. Meth. A* **361** (1995) 297–305 [see p. 58]

[98] L.P. Gaffney, *Octupole collectivity in ^{220}Rn and ^{224}Ra*, PhD thesis, University of Liverpool (2012) [see p. 58]

[99] H. Kankaanpää, *In-beam spectroscopy of very heavy elements*, PhD thesis, University of Jyväskylä (2001) [see p. 60]

[100] K.-H. Schmidt, R.S. Simon, J.-G. Keller et al., *Phys. Lett. B* **168** (1986) 39–42 [see p. 61]

[101] R.S. Simon, K.-H. Schmidt, F.P. Heßberger et al., *Z. Phys. A* **325** (1986) 197–202 [see p. 61]

[102] E.S. Paul, P.J. Woods, T. Davinson et al., *Phys. Rev. C* **51** (1995) 78–87 [see p. 61]

[103] G.D. Jones, *Nucl. Instrum. Meth. A* **488** (2002) 471–472 [see p. 64]

[104] K.-H. Schmidt, C.-C. Sahm, K. Pielenz and H.-G. Clerc, *Z. Phys. A* **316** (1984) 19–26 [see p. 64]

[105] J. Theuerkauf, S. Esser, S. Krink et al., *Program Tv*, Institut für Kernphysik, Universität zu Köln [see p. 65]

[106] A. Fitzler, *Tv Benutzer-Handbuch*, Institut für Kernphysik, Universität zu Köln (2007) [see p. 65]

[107] D.M. Cox, J. Konki, P.T. Greenlees et al., *Eur. Phys. J. A* **51** (2015) 64 [see pp. 67 and 100]

[108] D.M. Cox, *A Geant4 simulation of the SAGE spectrometer and its first application to ^{255}Lr*, PhD thesis, University of Liverpool (2014) [see p. 67]

[109] S. Agostinelli, J. Allison, K. Amako et al., *Nucl. Instrum. Meth. A* **506** (2003) 250–303 [see p. 67]

[110] E. Parr, R.-D. Herzberg, S. Antalic et al., *Eur. Phys. J. A* **48** (2012) 134 [see p. 73]

[111] P.A. Butler, P.M. Jones, K.J. Cann et al., *Nucl. Instrum. Meth. A* **381** (1996) 433–442 [see p. 81]

[112] P. Reiter, T.L. Khoo, T. Lauritsen et al., *Phys. Rev. Lett.* **84** (2000) 3542–3545 [see p. 82]

[113] G. Henning, *Stability of transfermium elements at high spin: measuring the fission barrier of ^{254}No*, PhD thesis, Université Paris-Sud (2012) [see p. 82]

[114] G. Henning, T.L. Khoo, A. Lopez-Martens et al., *Phys. Rev. Lett.* **113** (2014) 262505 [see pp. 82 and 83]

[115] C.W. Beausang, D. Prevost, M.H. Bergstrom et al., *Nucl. Instrum. Meth. A* **364** (1995) 560–566 [see p. 92]

[116] B. Singh and A.R. Farhan, *Nucl. Data Sheets* **107** (2006) 1923–2102 [see p. 99]

[117] E. Gete, D.F. Measday, B.A. Moftah, M.A. Saliba and T.J. Stocki, *Nucl. Instrum. Meth. A* **388** (1997) 212–219 [see p. 99]

[118] R. Holzmann, I. Ahmad, R.V.F. Janssens et al., *Nucl. Instrum. Meth. A* **260** (1987) 153–156 [see p. 100]

[119] G.J. Feldman and R.D. Cousins, *Phys. Rev. D* **57** (1998) 3873–3889 [see p. 104]

[120] S. Cwiok, J. Dudek, W. Nazarewicz, J. Skalski and T. Werner, *Comput. Phys. Commun.* **46** (1987) 379–399 [see p. 111]

[121] Yu.A. Lazarev, Yu.V. Lobanov, R.N. Sagaidak et al., *Phys. Scr.* **39** (1989) 422–435 [see p. 110]

[122] F.R. Xu, E.G. Zhao, R. Wyss and P.M. Walker, *Phys. Rev. Lett.* **92** (2004) 252501 [see pp. 110 and 112]

[123] F.G. Kondev, G.D. Dracoulis, T.L. Khoo et al., in *Proceedings of the International Conference on Nuclear Data for Science and Technology, Nice 2007*, EDP Sciences (2008) 61–64 [see p. 110]

[124] A. Chatillon, Ch. Theisen, P.T. Greenlees et al., *Eur. Phys. J. A* **30** (2006) 397–411 [see p. 112]

[125] T.L. Khoo and G. Løvhøiden, *Phys. Lett. B* **67** (1977) 271–274 [see pp. 113, 114, and 115]

[126] T.L. Khoo, J.C. Waddington, R.A. O'Neil, Z. Preibisz, D.G. Burke and M.W. Johns, *Phys. Rev. Lett.* **28** (1972) 1717–1720 [see p. 115]

[127] N. Nica, *Nucl. Data Sheets* **106** (2005) 813–834 [see p. 117]